Resonating Fluidic Circuits: A Novel Technology to Create a Portable Blood Viscoelasticity Measuring Device

Colin Eckhoff

A thesis submitted in partial fulfillment of the
requirements for the degree of

Master of Science in Bioengineering

University of Washington
2020

Committee:
Barry Lutz
Paul Yager
Robert Darling
Nathan White

Program Authorized to Offer Degree:
Bioengineering

University of Washington

ABSTRACT

Resonating Fluidic Circuits: A Novel Technology to Create a Portable Blood Viscoelasticity Measuring Device

Colin Eckhoff

Chair of Supervisory Committee:
Barry Lutz
Department of Bioengineering

The prehospital detection of coagulopathy has been identified as an important goal for the future of emergency medicine and trauma care. However, no clinically accepted devices that can diagnose coagulopathy by measuring blood clot viscoelasticity are portable, meaning that coagulopathy can only be diagnosed inside a well-resourced hospital. Resonating fluidic circuits are a promising technology to address this clinical need. In addition to being small enough to fit into a pocket, they are inexpensive to produce, and it has been suggested that they can be used to measure viscoelasticity. Previous research undertakings on fluidic circuits have not fully explored the potential of the technology to be applied to this clinical need. In this work, the scientific understanding of fluidic circuits is expanded, a fluidic circuit design is created for optimal viscoelastic measurement of blood clots, a portable, inexpensive, and efficient method of electrically instrumenting fluidic circuits is developed, and finally, the system is evaluated for its ability to specifically measure clot viscoelasticity relative to an existing device.

Table of Contents

List of Figures

List of Tables

Chapter 1: Clinical Background

1.1 Epidemiology of Physical Trauma

Physical trauma, defined as injury to living tissue caused by an extrinsic agent, is currently one of the greatest challenges in medicine. Every year, approximately 5.8 million people die globally due to trauma- a 32% higher death count than malaria, TB, and HIV/AIDS combined [1]. This comprises about 10% of the world's deaths, although these millions of deaths represent only a small fraction of the total incidence of trauma. Accurate figures for global trauma epidemiology are difficult to produce, but it is estimated that tens of millions of people worldwide suffer injuries that lead to hospitalizations, emergency room visits, or primary care facility visits. There are also many trauma cases that do not receive treatment through formal medical care. Of the trauma patients who do not suffer mortality, many will experience post-trauma morbidities, such as postoperative pulmonary compromise and thromboembolic events (such as blood clots that obstruct flow to lower legs, lungs, or brain), each of which being severely debilitating, and often lethal [2].

With the staggering amount of deaths that are occurring, the impact of trauma on human health is escalating. The incidence of trauma is expected to increase over the next 10 years at a faster rate than most other leading medical conditions [1]. This has already been observed in many developed countries. For instance, from 2000 to 2010, the population of the United States increased by 9.7%, but the absolute number of trauma deaths increased by 22.8% [3]. Although trauma may be perceived as a medical issue that primarily impacts developing countries, its intra-societal impact is actually greater in developed countries. As deaths due to infectious disease, maternal conditions, and malnutrition decrease while motorized transportation and population age increase, trauma has now become a leading cause of death in developed countries [4]. Using the United States as an example again, trauma is the leading cause of death for people under the age of 46, and is the 3rd leading cause of death overall, behind heart disease and cancer [5].

In response to the dire problem of trauma, this work will primarily focus on trauma as it affects the United States of America. In the US, a staggering 27.6 million people were treated in an emergency department for injuries in 2015, of which 2.8 million were hospitalized, with 214,00 total fatalities [6]. Falls, motor vehicle collisions, and gunshot wounds comprise the majority of trauma cases [5]. Trauma occurs throughout all age groups, making it the leading cause of years of life lost for individuals under 75 year old [3,5]. Despite being one of the most costly medical problems in the United States, trauma receives one of the lowest amounts of research funding of any medical condition relative to its impact on society. Injury accounts for 10% of the total disability-adjusted life years in the US per year, yet only 1% of the annual NIH budget is allocated for injury research [7].

1.2 The Trauma Triad of Death, and Current EMS Management

Hemorrhage, or profuse bleeding, is the leading cause of death among trauma patients, accounting for 40% of deaths [8]. However, deaths due to hemorrhage are generally considered preventable if more timely and appropriate medical care had been given [9]. Since patient conditions usually worsen over time following injury, it is paramount that the care be administered as fast and effectively as possible after they are received by EMS and trauma centers [10]. Although the historical temptation of trauma surgeons has been to immediately perform definitive anatomical corrections (like repairing visceral injuries), such corrections are often not well-tolerated by the poor physiological reserve of major trauma patients [11]. For instance, the surgical treatment of liver trauma is often time consuming, so trauma surgeons need to ensure that patients are of sufficient physiological status to withstand the length of the operation [12]. This has lead to the development of modernized resuscitation and surgical techniques in trauma medicine. These techniques, such as Damage Control Resuscitation (DCR) and Damage Control Surgery (DCS), focus on correcting homeostasis first, rather than anatomical issues [11, 13]. This allows doctors to mitigate an important medical phenomenon known as the ‘trauma triad of death’.

The trauma triad of death (also referred to as the 'triad') describes the combination of acidosis, hypothermia, and coagulopathy that commonly occurs in trauma patients with severe hemorrhage [14]. This fateful triad occurs in approximately 25% of all major trauma patients, but increases the risk of mortality by 4-5 times [15, 16]. At first, hemorrhage reduces the oxygen transport performance of the circulatory system, resulting in high levels of anaerobic respiration, lowering the pH of blood and leading to lactic acidosis [14]. This reduces myocardial performance and leads to a reduction in thermal circulation in the body, or hypothermia. Finally, hypothermia impairs the temperature- and pH-sensitive enzymes in the coagulation cascade, inducing coagulopathy. This exacerbates hemorrhage, and the cycle repeats as each factor compounds the others. As the cycle repeats, the positive feedback becomes so strong that hemorrhage can become uncontrollable, leading to patient death.

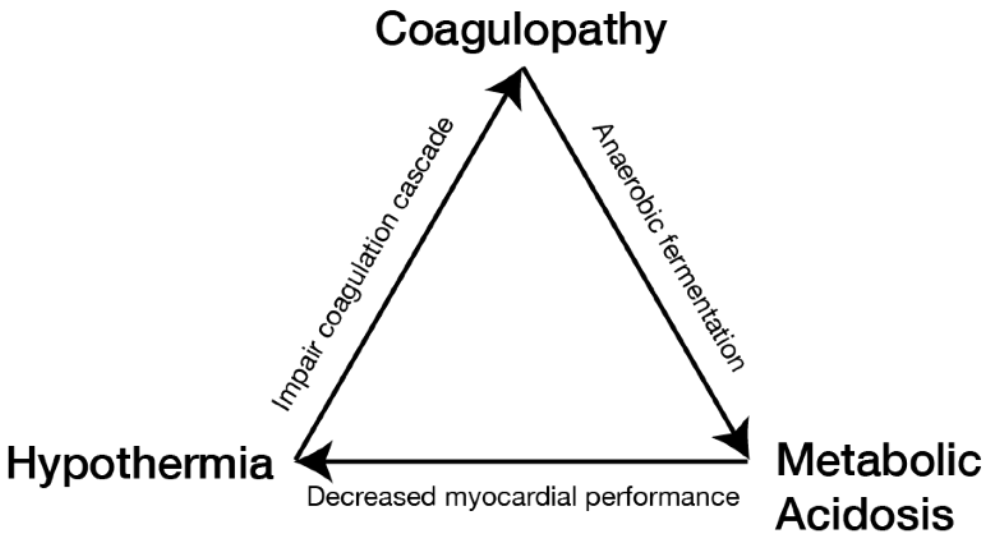

Figure 1.1. The cycle of the trauma triad of death. Adapted from [17].

Although the existence and progression of the triad is highly predictable in trauma patients, it is nonetheless extremely deadly, even with the most modern care practices. Each arm of the triad of death can be managed through present diagnostic methods, technologies, and resources that lead to subsequent mitigation therapies. However, resuscitation strategies for each arm of the triad are generally executed differently in different medical environments (ambulances, airlifts, ICUs,

operating theaters, etc.) based on that environment's available resources [18]. For instance, while paramedics can readily measure body temperature using a portable thermometer, or blood sugar using a portable glucometer, they cannot readily perform invasive surgical procedures or run laboratory-based diagnostic tests. This general problem manifests throughout nearly all segments of EMS care as a division between prehospital and in-hospital care quality.

Naturally, this division is present in trauma care. The first arm of the triad of death, hypothermia, is relatively straightforward to prevent, diagnose, and treat in the prehospital and in-hospital environment using simple thermometers and temperature control of the patient's ambient environment and injected fluids. The next arm, acidosis, is more complicated. While prehospital EMS cannot generally know the exact degree of patient acidosis, they can effectively work to prevent acidosis by limiting crystalloid transfusions (aqueous solutions of mineral salts and other water-soluble compounds, such as dextrose, with no blood products) to prevent blood dilution. In fact, the limiting of crystalloid transfusions is a tenet of the modern trauma techniques, such as Damage Control Resuscitation, that were designed to address the triad of death. Furthermore, in-hospital EMS care at emergency departments and trauma centers use advanced resources to specifically mitigate patient acidosis, safely complementing the conservative approach of prehospital EMS to acidosis.

The final component of the triad, coagulopathy, is only fought in situated hospital environments, while prehospital EMS care protocols largely neglect it. This disparity exists due to technological limitation: coagulopathy can only be diagnosed in a medically useful manner by laboratory devices. Without a means of diagnosis, coagulopathy mitigation therapy in prehospital EMS environments is not feasible [18]. Most hospitals and trauma centers, on the other hand, have access to coagulation testing devices. Testing results are analyzed by hemostasis experts to guide resuscitation using reserves of blood products and pharmacological compounds. Mitigation strategies are tailored toward individual patients and their coagulation status. Prehospital EMS care is relegated to relying on good medical practice for the other two arms of the triad (hypothermia and acidosis) to avoid perpetuating any preexisting coagulopathy.

1.3 The Coagulopathy Problem

The trauma triad of death describes major threats to homeostasis during traumatic injury and hemorrhage, so it is critical that all such threats be addressed in the medical care of EMS. It is clear that EMS has taken important steps in implementing protocols that benefit from the theory of the triad. However, when evaluating how EMS currently handles the three arms of the triad, there are obvious shortcomings related to one arm of the triad: coagulopathy. Upon injury, inflammatory and metabolic changes usually initiate coagulopathic tendencies, which are then significantly exacerbated by hypothermia and acidosis (the other arms of the triad of death) into more deadly coagulopathies. Misguided resuscitative decisions made during this time can also exacerbate coagulopathy through hemodilution, commonly referred to as dilutional coagulopathy. However, the diagnosis and treatment of coagulopathy requires sophisticated medical instruments and resources that are generally inaccessible to prehospital EMS. This has resulted in coagulopathy becoming one of the most problematic challenges of trauma medicine. Therefore, the remainder of the clinical background of this work will focus on coagulopathy, derived from the triad of death, as the major medical challenge of major trauma.

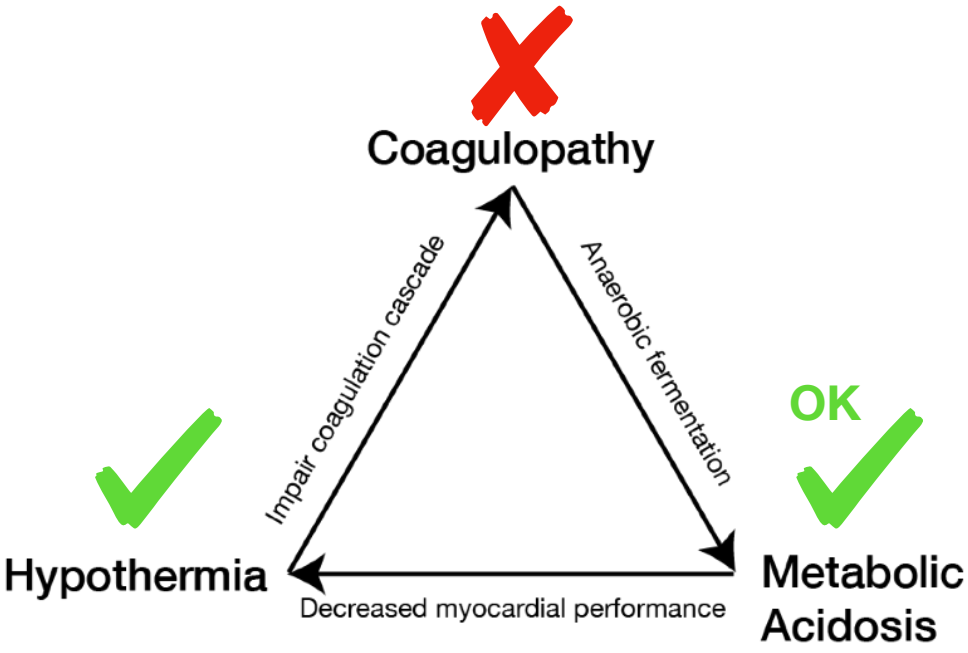

Figure 1.2. The triad of death annotated with EMS mitigation capabilities.

Coagulopathy is both common and deadly, as it occurs in approximately 25% to 30% of all major trauma patients, but increases the risk of mortality by 4-5 times [15, 16]. In fact, it is specifically implicated as the primary cause of death in almost half of hemorrhage deaths in trauma patients. Consequently, coagulopathy alone is one of the single most accurate predictors of mortality and prognosis. Although coagulopathy may be mistakenly generalized as a baseline disorder appearing only in select patients due to preexisting conditions such as Hemophilia or blood thinner therapy, it can actually be induced by trauma into patients of any prior health status, including, and especially, younger trauma patients.

It is vital for trauma patients that EMS use rapid and aggressive techniques to identify and control coagulopathy. Identification of coagulopathy allows for perturbations in patient homeostasis to be quelled before the situation becomes irreversible, and enables more effective blood bank utilization and triaging. Several methods already exist to perform coagulopathy identification. The most low-tech methods are observational indexes that rely on the assessment of physicians or paramedics to identify patients at an increased risk of coagulopathy. These indexes usually account for the circumstances and severity of an injury, the presence of shock, and patterns in vital signs. Unfortunately, these indexes generally cannot accurately identify or stratify patients in a manner that is specific enough to combat coagulopathy [18]. The diagnosis of coagulopathy can only be clinically made using coagulation testing devices. Coagulation testing devices exist in many forms, and many have been used for decades now in trauma centers, ICUs, and operating rooms.

1.4 Limitations of Existing Coagulation Testers

The first challenge in coagulopathy treatment is detection. A wide variety of devices that analyze blood coagulation currently exist to perform these diagnostics, and they vary considerably in their function and form [19]. To simplify the broad market of these devices, two general categories will be introduced: conventional coagulation tests (CCTs), and whole blood viscoelastic (VE) tests. While it is important to acknowledge that there are novel testing technologies that do not necessarily fit either the CCT or VE test description, they are omitted

from our market representation, as they consist primarily of platelet diagnostic sensors that are still exploring their potential clinical applications. An example of such a new device would be Stasys.

Five classic CCTs are International Normalized Ratio (INR), Prothrombin Time (PT), activated Partial Thromboplastin Time (aPTT), platelet count, and fibrinogen level. These CCTs have long histories of use in hematology, including trauma medicine applications [6]. However, CCTs are limited by their slow results, limited functional representation of the coagulation cascade, and poor demonstrated association with better clinical outcomes [7]. Alternatively, coagulation analysis can be done using VE tests, with brands like thromboelastography (TEG), ROTEM, and Sonoclot being major players. VE testing, in contrast to CCTs, provides a more specific and comprehensive description of patient clotting activity [20]. To this end, it has been found that r-TEG, a rapid, chemically-activated version of TEG, provides clinically superior information than CCTs for directing hemostasis and anticoagulation therapy in trauma cases [19]. Traditional VE tests take up to thirty minutes to complete, with the most clinically useful data being available within ten-to-fifteen minutes, but accelerated versions of VE tests typically take a third of that time to produce analogous data. Some documented benefits of VE-guided resuscitation include reduced blood product usage, more appropriate triaging, and improved post-operation outcomes.

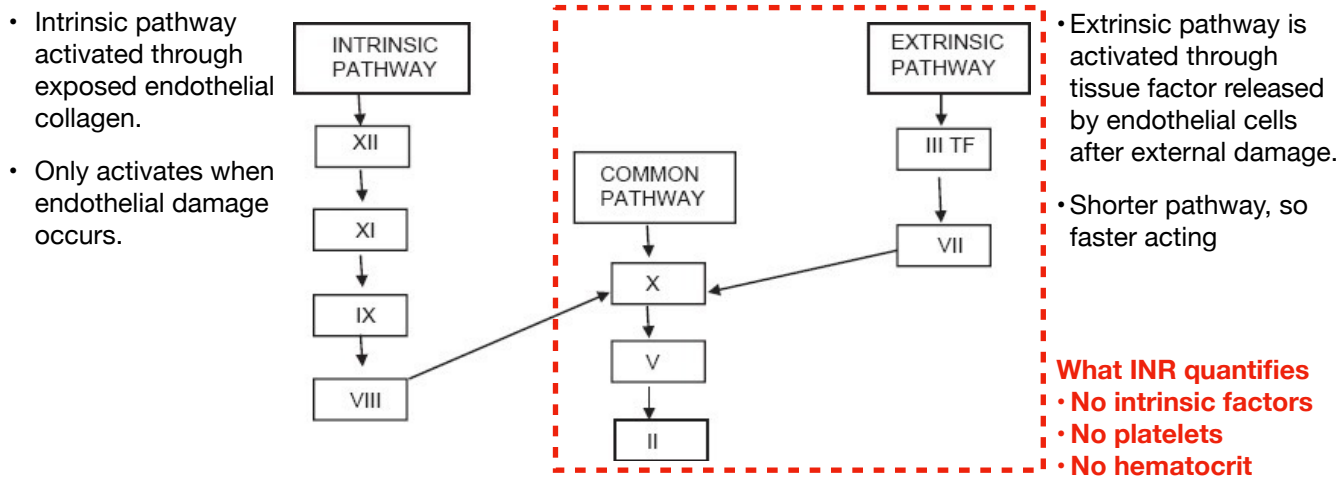

Figure 1.3. Coagulation cascade with INR measurement outlined. Taken from [21].

For the sake of more technical coverage, below are more descriptive details for the two tests:

CCTs

- PT/INR most popular; measures the time it takes for plasma to clot after adding thromboplastin.
- Only quantifies the function of the extrinsic and common blood coagulation pathway.
- Some can be implemented as a point-of-care device.
- Home INR monitoring is common for monitoring the effectiveness of anticoagulation therapy, such as warfarin.
- It does not evaluate the functional clotting performance of whole blood.

Viscoelastic Testing

- Measures the mechanical impedance of a clotting whole blood sample over time.
- Whole blood assays have been found useful and cost-effective in perioperative settings.
- Large device size and weight limits use to laboratory settings.
- Relatively large blood sample volumes.
- Device costs $40,000

A qualitative comparison between CCTs and VE testers reveals a trade-off between portability and diagnostic power in current blood coagulation analyzers. While the use of VE testers in trauma settings to detect coagulopathy and guide resuscitation is well established [9], all current implementations of whole blood coagulation analyzers are unfortunately nonportable devices. New devices, such as the TEG 6s, may be marketed as point-of-care medical devices, but their large sizes, weights, and costs limit their feasibility in prehospital settings [7]. On the other hand, popular CCT devices have made significant progress in becoming more portable, increasing testing accessibility at the point-of-care. However, they are not frequently used in major trauma medicine due to the limited clinically actionable information obtained from such devices, resulting in the portability-power divide between CCTs and VE testers.

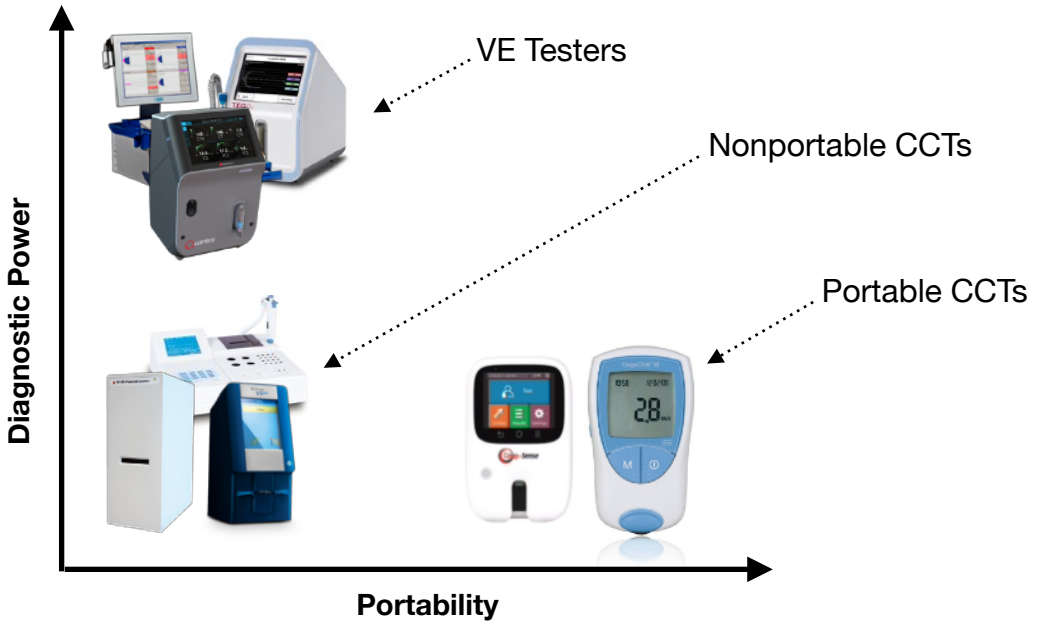

Figure 1.4. Market landscape of blood coagulation analyzers.

The division among coagulation analyzer devices is problematic for addressing the serious challenges that coagulopathy creates in trauma medicine, as will be examined in the next, and final, section of this chapter.

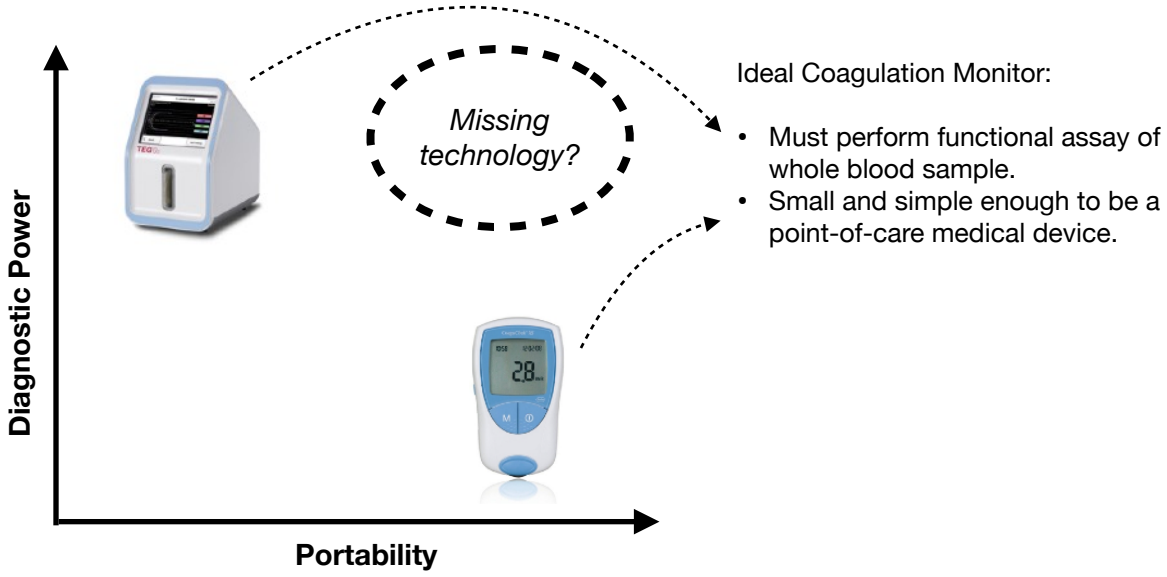

Figure 1.5. Generalization of blood coagulation analyzers, illustrating unfortunate trade-off between portability and diagnostic power.

1.5 The Need for a Portable Whole Blood Viscoelasticity Tester

Although coagulopathy testing has found prominence within the 21st century for its effectiveness in guiding trauma resuscitation, there is still significant room for improvement in reducing preventable trauma deaths. Preventable trauma deaths are defined as casualties that could have been avoided by more timely or appropriate medical care [22]. Given by this definition, care timeliness and effectiveness, particularly for coagulopathy, are of unparalleled importance in saving more lives in trauma. Yet, while the modernization of medicine has improved the clinical management of coagulopathy, the vast majority of that innovation has been bounded to hospitalized patients. Prehospital EMS coagulopathic intervention is nearly impossible because the technological resources required to monitor coagulopathy, namely testing devices, are expensive and inaccessible. Since prehospital EMS is still unequipped to manage coagulopathy, there is little that first-responders, paramedics, and other prehospital EMS personnel can do for affected patients. Therefore, if a trauma patient has coagulopathy, they are at a significantly increased risk of death due to hemorrhage (4-5 times mortality risk, as shown in section 1.2) [15, 16]. This is why the clinical outcomes of current trauma patients are highly contingent upon whether they can survive until hospitalization, where coagulopathy diagnostics and targeted therapies can finally occur.

However, as discussed, many coagulopathic changes occur early after trauma, so by the time damage control measures are undertaken in hospitals, the coagulation abilities of the severely injured patient can already be compromised enough to guarantee mortality [9]. The primary barrier that prevents earlier, more frequent, and more useful coagulopathy testing from occurring is technological in nature, as there is a lack of an adequate coagulation monitor that can be both portable and diagnostically powerful [18].

Therefore, there is a significant need for a portable, point-of-care VE testing device. A device of this type could allow paramedics, emergency medical technicians (EMTs), and other EMS personnel to test for patient coagulopathy as soon as possible. This information could assist critical triaging decisions. It could be communicated to specialists at hospitals. It could allow

doctors to anticipate certain resuscitation strategies, and recruit the appropriate resources and personnel ahead of patient arrival. Since trauma care timeliness is paramount for patient survivability, expedited coagulopathy diagnostics can help trauma patients to receive the coagulopathy therapy they need as soon as possible after hospital admission, increasing survival rates.

A portable VE testing device could also allow paramedics, EMTs, and other emergency medicine personnel to diagnose patient coagulopathy as soon as possible to administer early pharmacological interventions that are currently only administered in the hospital, such as individualized Blood Component Therapy, procoagulant hemostatic agents, fibrinogen concentrate, and tranexamic acid. Ambulances across the country are currently trending to carrying more blood products, so the logistics of patient-centered prehospital coagulation therapy using blood and pharmacological products are not new to EMS personnel. In addition, early coagulopathy diagnostics can reduce scarce blood product usage, improve triaging, prevent over and under resuscitating of patients, and enhance key communications with hospitals during patient transport. All of these benefits have been observed from the use of in-hospital coagulopathy diagnostics, and are needed in the prehospital point-of-care in order to help buy trauma patients enough time to make it to a hospital or trauma center and increase survival rates [19].

As the remainder of this work will demonstrate, the Lutz laboratory of UW Bioengineering has developed a novel technology that could allow such a device to be practically realized. This technology, referred to as “AC fluidics”, can be used to perform mechanical impedance measurements of viscoelastic materials, with blood VE testing being an obvious candidate for a clinical application. The next section will introduce more specific design requirements for a new, portable VE tester for use by EMS, and the science and engineering process behind AC fluidic technology will be detailed in further sections.

Chapter 2: Design Requirements

2.1 The Use Cases of Point-of-Care Coagulopathy Diagnostics

With the pressing clinical need for a portable VE tester having been established, we will now devise specific, quantitative device requirements to be implemented by the engineering process. A portable blood viscoelasticity tester has multiple value propositions that each correspond to a certain hypothetical clinical use case, as each use case requires slightly different design priorities. The three use cases are: total prehospital reform, partial prehospital reform, and telemedicine.

The first use case of a portable VE blood tester entails comprehensive hemostatic resuscitation in the prehospital environment. In this case, emergency medical transportation would be outfitted with all the resources and equipment necessary to perform VE-guided resuscitation outside of a hospital setting, transforming the vehicle or field station to resemble a hemostasis ICU. This is described by Spinella [22]. Coagulopathy information obtained from the VE data would be utilized by trained personnel to specifically guide hemostatic resuscitation. Meanwhile, receiving hospitals would rely on resuscitation having already begun. Therefore, they need only continue the resuscitative process until definitive anatomical corrections can be performed. It is easiest to imagine this scenario occurring on an airlift or remote medical station, where space, equipment, and personnel training are more available than on a typical ambulance.

The second use case entails a reduced set of protocol changes for EMS, where the device is used as an assistive measure for administrative EMS decisions. Instead of attempting to bring the complete assortment of hemostasis resources, equipment, and personnel forward in time to prehospital EMS care, this use case recognizes the potential for a limited, but effective set of practical changes that can still improve trauma patient outcomes. For instance, rather than guiding advanced resuscitation to specifically mitigate trauma-induced coagulopathy, the testing information could warn EMS personnel and first responders regarding the overall severity of the patient's hemostatic condition, which is then used to improve triaging and transfusion decisions.

For instance, coagulopathy testing is known to be a good predictor of internal or prior hemorrhage that may otherwise be undiscovered. Such protocols would be based on the best practices that can be done with a summary of the patient's hemostatic state, limited by what is actionable by EMS personnel. Hospitals would still be the only facilities with access to comprehensive resources for hemostatic resuscitation, and thereby will provide complementary patient care using more advanced techniques. This use case is feasible in a faster paced, highly protocolized setting, such as an ambulance, where the time and focus of accompanying paramedics and EMTs must be respected.

The final use case of this device concept entails usage solely for telemedicine. In the event that prehospital VE testing cannot render significant changes to EMS resuscitation protocols due logistical, environmental, or tactical barriers, then the VE testing results could still be communicated to hospitals and trauma centers before patient admission. Such expedited testing results would allow in-hospital personnel to anticipate care procedures, and recruit the necessary resources and personnel before patient arrival. This would improve the quality and timeliness of hemostatic resuscitation that the admitted trauma patient receives. After the execution of the initial resuscitative intervention, continued hemostasis support can be guided using any VE testing device. This use case allows for the above benefits to be realized while transit time is still prioritized and the workflow of paramedics is not impeded, even if prehospital hemostatic resuscitation is currently unfeasible for EMS.

2.2 Use Case Priorities Translated to Engineering Requirements

Each of the use cases for a portable VE tester represents a different approach to EMS and trauma medicine, based primarily on pragmatic considerations. Therefore, the design requirements for each case will vary to reflect those things. For the first use case, comprehensive hemostatic resuscitation, imagined for an airlift or field station environment, the data veracity of the entire VE curve must be high, and the testing cost must be low, because precise medical interventions will be based on the quantitative values of the VE data, and testing is expected to be repeated in order to track the progression of patient hemostasis. For the assistive measure case, imagined on

an ambulance, the speed of the test should be quick and the size of the device should be small, because critical EMS decisions need to be made expediently, and the device must be able to fit into a paramedic kit. For the final telemedicine case, communications must be available, the sample size must be small, and the device itself should be very easy to use, because the reduction in blood needed and the convenience of use help to avoid distracting EMS personnel. None of the above requirements are mutually exclusive to their respective use cases, and the sorting is only a reflection of the greatest priorities of each case.

Certain product requirements can be globally applied across all use cases. The first of these requirements is vibration resistance. In any prehospital environment, device motion should be expected during testing due the often hectic nature of EMS work and transportation. Preexisting VE testing devices can have known vulnerabilities to motion interference, so resistance to such interference in necessary for a portable VE tester. Furthermore, any conceivable use of this device will require the production of VE data to be displayed or transmitted, so it is necessary to include an output stream of VE data that can be handled and/or processed by subsequent display, communication, or development systems.

Finally, the use case design priorities must be converted into engineering product and system requirements. All of the above priorities may be assigned to one or more of three engineering fields related to the system: fluidic circuit design, VE testing effectiveness, and electrical design. The fluidic circuit design must be small in size, accept a small sample size, easy to load a sample, and be inexpensive and consistent to fabricate. The clot measuring principles should be accurate, and quick. The electrical systems on the device should support data communication, vibration resistance, and a simple user interface.

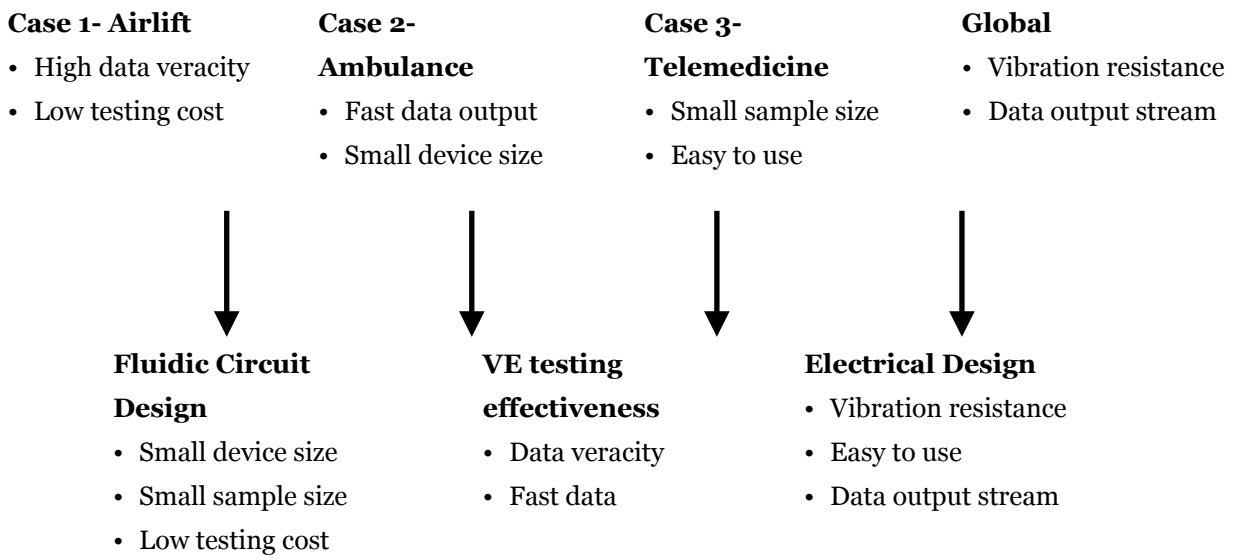

Figure 2.1. Use cases translated into high-level product requirements.

2.3 Properties of Clots and VE Testing

Blood clots, and other viscoelastic materials, exhibit both viscous and elastic behavior. This is often represented as a shear storage modulus (G') and a shear loss modulus (G''), respectively representing elasticity and viscosity. For complete characterization of a viscoelastic material, the two can be combined into a complex number called the shear dynamic modulus (G^*), from which the overall mechanical impedance magnitude and stress-strain phase lag can be obtained. The G' and G'' parameters can also be construed as other common mechanical parameters, such as Young's modulus.

$$G^* = G' + iG'' \tag{2.1}$$

However, VE testing devices do not measure absolute physical properties of blood, such as shear modulus, Young's modulus, and viscosity [23]. The data units of VE testing devices are typically based on arbitrary, preset scales from algorithms that specify normal ranges and intervention thresholds based on clinical trial results. The precise mechanical properties uncovered by VE testing are disputed. Some believe that the elastic modulus is measured, while others believe the

shear modulus is measured, or even a combination of the elastic amplitude and viscous behavior [24]. According to these arguments, the relative contributions of elasticity and viscosity to VE tester output amplitude cannot be determined, and thus, it is not strictly possible to use VE testers to measure elasticity. Therefore, VE testers are able to measure an approximation of the magnitude of G^*, but unable to collect phase information available to help discern G' or G''. Thus, there are no theoretical mathematical models defining the exact relationship between the G' and/or G'' physical properties and VE tester data, but there is consensus that VE outputs are functionally related to the viscoelasticity of a blood sample [23]. Therefore, the diagnostic power of VE testing has largely been based on intuition, heuristics, and shape recognition. For instance, the heuristic equation for ROTEM to convert output amplitude into shear modulus is:

$$G = \frac{100 \times A}{100 - A} \tag{2.2}$$

Evidently, there is not much analytical or physical reasoning to gather from this expression. Since VE testers themselves do not define a precise mathematical relationship between the output amplitude and the viscous and elastic components of the blood sample, we are not necessarily compelled to do so either. It is important to not confuse the following two goals:

1. To make a point-of-care VE tester.
2. To make a new type of VE tester that can distinguish between viscosity and elasticity.

The goal to make a point-of-care VE tester is the driving force behind this work. If we were trying to create a VE tester with viscosity and elasticity discrimination, the clinical background, markets targeted, and requirements for this project would look quite different. For instance, such a new type of VE tester would likely be unconcerned at this stage with point-of-care availability, as the research and development ought to focus on the special handling of viscoelastic materials in this hypothetical new instrument. The inability of current VE testers to distinguish between viscosity and elasticity has been accepted for decades, yet they are still used every day in the

clinic. There is, of course, room for this technical improvement, but we must also not sidetrack ourselves with problems that are out of the scope of the clinical background with which he have interested ourselves: that there is a need for a portable VE tester.

What ultimately matters is that our system shows a consistent, specific response to blood clotting over time, allowing inductive reasoning to support a causal relationship between the physical properties of a blood sample and the system output amplitude. However, even if this is all that is necessary to demonstrate a working system, we still ought to design this system to measure the known elasticity range of blood samples, lest it fail during experimentation without our understanding. The TEG product line is advertised as measuring the shear modulus of a blood clot as an indicator for overall mechanical impedance. The elastic modulus can also be utilized as a similar indicator, as the shear and elastic moduli of a material are related, given a constant poisson ratio or bulk modulus (see chapter 4 for more information on the design of this system to measure elasticity). The range of elastic moduli the system must be able to measure should ideally be from 100 Pa to 100 kPa, covering the range of typical clotting activity [25].

2.4 Product Requirements

To imagine towards a point-of-care VE analyzer, the requirements of an ideal product are produced. A portable VE analyzer can enable paramedics to significantly improve trauma patient survivability by providing EMS the option of doing such testing in order to enable targeted hemostasis therapy, improve triaging, and allow medical centers to anticipate care challenges before patient arrival. As a coagulation testing tool, the device ought too be used with a drop of patient whole blood, which will be sampled with a disposable cartridge that electronically measures the clot properties. There should be no additional tools necessary, including collection tubes or needles. The first available information from the device should be available within a 5-15 minute window, allowing first responders time to address immediate trauma care during the testing period of the blood sample. Additionally, there should be a wireless communication feature that can connect hospital personnel to the coagulation information of the patient in real time.

Ideally, the device would accompany EMS personnel on routine calls regardless of the intent of treating trauma. This would allow flexibility in response while minimizing required weight restrictions arise in certain settings. These settings include airlifts, ambulances, and field setups, such as military or rescue zones. They are often austere, with temperature, motion, and other environmental and transportation-related stresses being significant considerations. The battery operation must be capable of supplying weeks of standby and multiple days of continuous testing. The product should comprise a handheld electronic device that accepts passive disposable cartridges. The handheld reader will feature a display, battery, and electronics that transmit and receive signals from the disposable cartridges. The product must 1) cause no harm to patients 2) provide meaningful data to allow responders to act 3) be easy-to-use and 4) be portable and rechargeable.

Specification	CoaguChek XS	TEG 6s	Acceptance Criteria for New Device	Justification
Device Size	5.4” x 3.1” x 1.1”	11.4” x 8.6” x 7.0”	4” x 2” x 0.5”	Portability
Sample Size	≥8 µL	300 µL	<50 µL	About one drop of whole blood
Testing Cost	$20	$60-100	$10	Cheapness
Diagnostic Power	PT/INR	Classic VE	Classic VE	Whole blood test
Vibration resistance	Perfect	Fair	Good	Utility in transportation
Ease of Use	Easy	Not easy	Easy	EMS ergonomics
Testing time	13 seconds	Real-time clotting (15 mins); Can be accelerated (5 mins)	Real-time clotting (15 mins); Can be accelerated (5 mins)	Same ballpark as TEG and RapidTEG
Comms	Local IR	Software cloud	Serial output	Flexible output
Manufacturing	Recalls issued	Expensive	Not expensive	Low test cost

Table 1. Specification comparison between classic blood coagulation analyzers and a new portable VE testing device to meet the clinical need described.

2.5 Key Innovation to Sensor Instrumentation

If a low cost, highly accessible method of conducting VE tests were already established, then it would be in use right now in portable whole blood VE testers. However, as discussed, neither an established technology, nor a portable VE tester currently exist. The Lutz laboratory of UW Bioengineering has developed and applied a novel instrumentation technology that is well-suited for this application [26, 27]. The name of this new technology has been dubbed "AC fluidics" as well as "fluidic circuits" by our laboratory. AC fluidics consists of easy-to-fabricate fluidic systems whose behavior resembles a classic, second order linear system, such as an electrical RLC circuit or mechanical spring-mass-damper system. Therefore, these systems have characteristic resonance and damping properties. By observing changes in these properties when a small, mechanical modification is made by the insertion of a clotting blood sample, the viscoelastic changes in the sample can be measured. The science of AC fluidics is explained in chapter 3, but a limited understanding of it is needed to produce system requirements for this work.

2.6 System Requirements for This Work

The goal of this work is not to create a fully commercializable device, but to lay the foundations for future work on portable VE testing technology using AC fluidics. The prototype built only needs to establish the working instrumentation principles and feasibility to the described clinical application. Environmental robustness, fully integrated systems, and complete portability are not necessary. To create reasonable scoping to this work, having covered the clinical background and derived the associated product requirements, the following list states the technical objectives of this work:

1. Document scientific principles of AC fluidics and expand upon them.
    a. Recall and organize existing scientific understanding of AC fluidics from prior work.
    b. Expand science using analytical and simulated models to aid future design work.
2. Design a fluidic circuit for measurement of clot elasticity.

    a. Produce a fluidic circuit layout which can produce electrical resonance signals.
    b. Design the remainder of the circuit to optimally measure clotting elasticity.
    c. Empirically justify responsiveness of fluidic circuits to changes in clot elasticity.
3. Design novel electrical instrumentation system for fluidic circuits.
    a. Produce system requirements for the instrumentation.
    b. Design and implement electronic instrumentation system.
4. Evaluate clot-measuring potential of designed fluidic circuit.
    a. Experimentally evaluate ability of system to measure clot elasticity preliminarily.
    b. Qualify measurement limitations of system.

The ordering of the objectives approximates the ordering of the remaining content in this document.

Chapter 3: The Science of AC Fluidic Systems

3.1 Preface

For interdisciplinary engineering projects, it can be extremely beneficial to rephrase unfamiliar problems in familiar terms, thereby allowing the limited expertise of a team to be applied more broadly and more powerfully. For instance, an understanding of electrical RLC systems can allow an electrical engineer with no pedigree in mechanical engineering to approach mechanical spring-mass-damper systems due to the analogous mathematics of the two systems. Likewise, the key to understanding AC fluidics technology is to first understand the mathematical analogies that can be drawn between the phenomenon of resonance in different physical domains. More generally, systems of this type can be described as second-order linear time-invariant (LTI) systems. With any LTI system, regardless of its physical domain, the principles and practices of system analysis in the time domain and frequency domain can be applied.

Since the majority of the technical work on this project can be best described as electrical engineering, we will use electrical RLC circuits as our method of analogy when describing AC fluidic systems. By extension, we will also use electrical terminology when analyzing the systems, such as voltage, current, resistance, step response, and frequency response. Later in the chapter (section 3.4) we will precisely document the electric-hydraulic analogy to apply our understanding and intuition of electric systems to fluidic ones.

3.2 Electrical RLC Circuits and Resonance Review

To begin, a concise review of electrical RLC circuits and their properties will be presented.

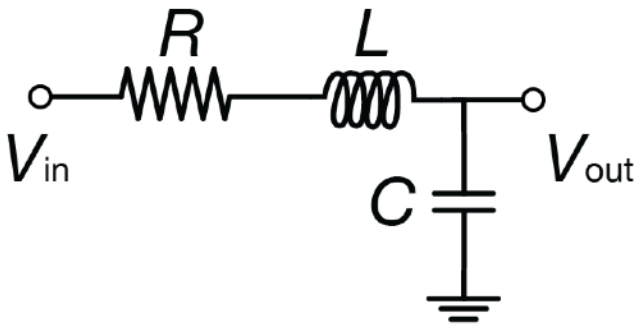

Figure 3.1. Classic low-pass RLC circuit.

Electrical RLC circuits are classic systems that have well-understand mathematical underpinnings. They are simply electrical circuits that contain three passive components: resistors, inductors, and capacitors. Resistors are components that behave as "friction" sources by nonspecifically impeding the flow of electron current, whereas capacitors and inductors impede the flow of electron current with a degree of specificity. The specificity of their impedance, called reactance, can be found through the basic property equations for these components. Using the constitutive equation for a capacitor:

$$Q = CV \tag{3.1}$$

$$\frac{qQ}{qt} = I = C\frac{dV}{dt} \tag{3.2}$$

Where Q is charge, C is capacitance, I is current, and V is voltage. Equation 3.2 proves that the current moving through a capacitor is not simply proportional to the voltage across that capacitor. Rather, the current is proportional to the *rate of change of voltag*e across it. Since impedance is equal to the voltage difference produced by a given current moving through an element ($Z = \frac{V}{I}$), we can apply a voltage signal to equation 3.2 and rearrange to determine the impedance of a capacitor. The input signal $V = Ae^{st}$ is the eigenfunction of an LTI system, where A is amplitude, $s = \sigma + j\omega$ is complex frequency, and t is time. Differentiating and applying to equation 3.2:

$$I = sAe^{st}C \tag{3.3}$$

$$Z_C = \frac{V}{I} = \frac{1}{sC} \tag{3.4}$$

Focusing on steady-state frequency only,

$$Z_C = \frac{1}{j\omega C} \tag{3.5}$$

There are two important takeaways here. First, the impedance of a capacitor is a complex number. The means that there is a magnitude and phase associated with the capacitor's impedance across different frequencies. Second, the magnitude is inversely proportional to the frequency of the input current, and there is also a -90º linear phase term, resulting in voltage that lags behind current in phase. For brevity, the impedance of an inductor will be also be given here, but can be found using similar derivations: $Z_L = j\omega L$. The magnitude response of an inductor is directly proportional to current frequency, and the +90º linear phase term results in voltage leading current in an inductor, not lagging.

With only our knowledge of the opposite natures of the respective impedances of capacitors and inductors, the behavior of resonance can be inferred. Since the angle between the two impedance phasors is supplementary (180º), they can destructively interfere. At a specific frequency where the magnitudes of the two phasors are equivalent, the phasors cancel each other out, and all reactive impedance is removed from the circuit, leaving only real, resistive terms. This frequency is found as follows:

$$|X_L| = |X_C| = \omega L = \frac{1}{\omega C} \tag{3.6}$$

$$\omega^2 = \frac{1}{LC} \tag{3.7}$$

$$\omega_0 = \sqrt{\frac{1}{LC}} \tag{3.8}$$

This frequency for which there are no imaginary impedance is known as the resonant frequency (ω_0). The affect that resonance has on an RLC circuit depends on the layout of the circuit. Some circuit designs result in maximal output magnitude for the resonant frequency, while others minimize the output magnitude at the same frequency. This can be exploited to create useful systems, such as bandpass or bandstop filters. Other times, resonance can exist within electrical systems, often from parasitic inductance and/or capacitance, that is undesired and deleterious, requiring design consideration and compensation.

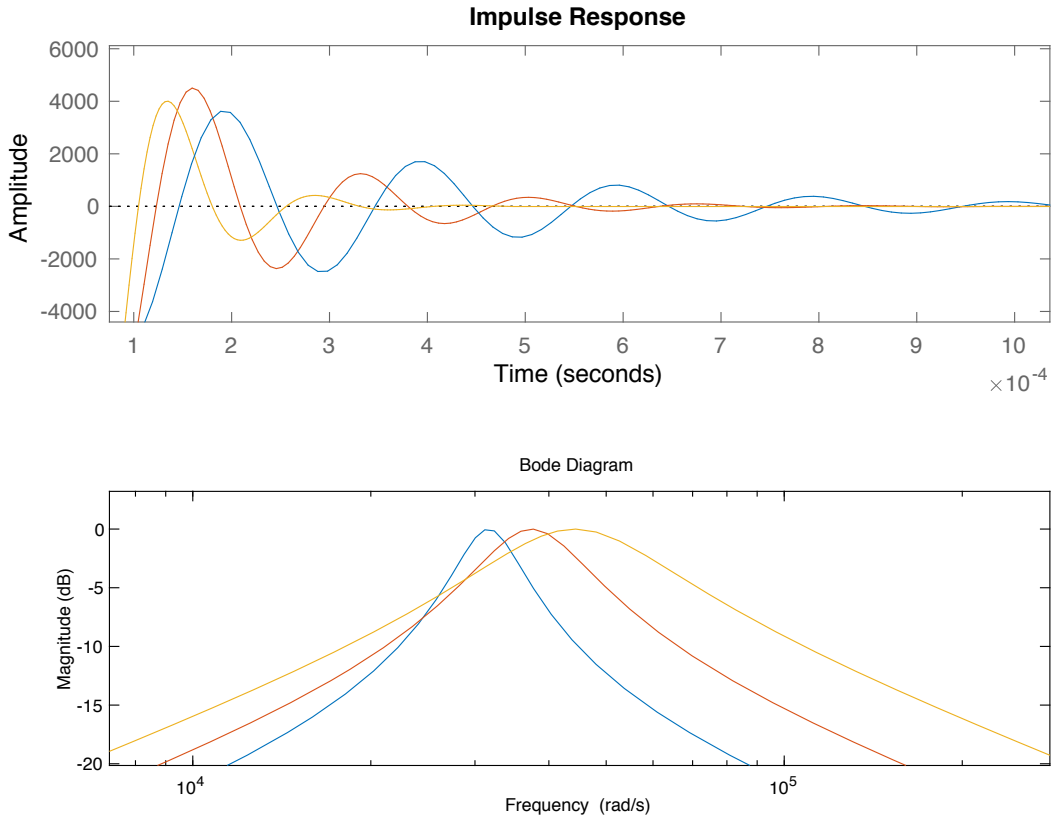

Figure 3.2. Time and frequency domain responses of various band-pass RLC circuits with different resonant frequencies and damping factors.

The resonant frequency and its extrema in the magnitude response is the most famous phenomenon of resonance, but there exists another important parameter, which is modulated by the resistive term: damping. The magnitude of the resistive term relative to the LC reactance determines how “sharp” the circuit magnitude response is, at and around the resonant frequency. Damping also determines the nature of the system response for classic inputs such as a step function: whether there are oscillations, and how prolonged those oscillations are.

3.3 Generalizing RLC Circuits to Transfer Functions for LTI Systems

As alluded to in the preface of this chapter, we will now proceed to embellish our understanding of AC fluidics using the concept of LTI systems. With our knowledge on electrical RLC circuits and resonance, as well as the electric-hydraulic analogy, we can tie everything together by mathematically describing fluidic systems using transfer functions. The theoretical nature and practical generality of transfer functions enables us to easily classify, analyze, and compare systems.

Representing any lumped-element LTI system as a topological connection of generic, unknown impedances, one can find the transfer function simply by using simple circuit rules of series and parallel impedances, as well as Kirchhoff’s circuit laws. Below are several examples of this:

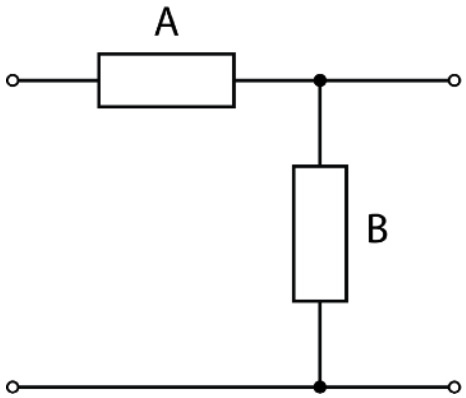

Figure 3.3. Generic divider circuit.

$$H(s) = \frac{B}{A + B} \tag{3.9}$$

Now let us do the same on circuits with known RLC impedance elements. Recalling the impedances of a resistor (R), capacitor ($\frac{1}{sC}$), and inductor (sL), we can use simply substitute the generic impedance values with the element-specific expressions. The resulting transfer function notably becomes a polynomial of the variable s.

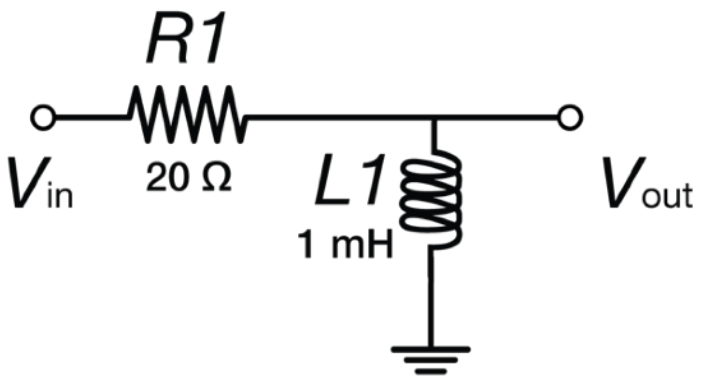

Figure 3.4. Numerically parameterized RL circuit.

$$H(s) = \frac{sL}{R + sL} = \frac{s0.001}{20 + s0.001} \tag{3.10}$$

From this transfer function, analytical expressions for time-domain and frequency-domain responses can be obtained. To be more detailed, time-domain system responses can be obtained by multiplying the transfer function by the Laplace transform of the time-domain input, and then performing the inverse Laplace transform. The steady-state frequency-response of a system can be obtained by evaluating the transfer function, which exists on the Laplacian s-plane, on the $j\omega$ axis. For a steady-state frequency response to exist, the system must be bounded-input, bounded-output stable. Another way of stating this is that the impulse response of a system must be absolutely integrable. Since any practical RLC circuit will contain resistance, either through design intentions, or unavoidable parasitic losses, damping will occur in every RLC system. Therefore, even if an RLC circuit rings like a bell upon an input transient, it will always be stable, and this always has a continuous, well-behaved frequency response.

In order to enable efficient design processes, software-based modeling tools can be used with transfer functions. Not only do these tools dramatically streamline the design process of fluidic

circuits for experimentation, but they also benefit the scalability of this technology towards commercial applications. For AC fluidic systems, arbitrary physical prototyping is not feasible on a larger scale, and higher complexity systems should be designed using software tools. The Control System Toolbox in the MATLAB software provides an excellent method of doing fluidic circuit analysis, as it allows us to input a transfer function found symbolically, plug in numerical values for the RLC parameters, determined by the dimensions of the circuit elements, and simulate the system in action.

3.4 Electric-Hydraulic Analogy for AC and DC Applications

With our understanding and intuition for RLC circuits, we can now transition from the electrical domain to the hydraulic one by using the electric-hydraulic analogy. First described by Sir Oliver Lodge in the early 20th century, this analogy enables engineers to translate the rich behavior of electrical systems into analogous fluidic systems [28]. Resistance is given by the irreversible, frictional interactions of viscosity between a fluid and the boundaries of the flow channel. Inductance is given by the inertial reluctance of a fluid's mass to change its velocity. Capacitance is given by the ability to store fluid volume through the compression of a fluid itself, or through elastic volume deformations in the flow channel. Thus, fluidic circuits can be modeled by electrical circuits by using specific flow channel sizes to represent serial resistors and inductors, and compressible regions of specific elasticities to represent capacitors. The electric-hydraulic analogy can also be applied to other fluidic systems, such as pneumatic ones. Our utilized version of the electrical-hydraulic analogy ignores the effects of Bernoulli's principle, where the pressure and flow velocity are inversely proportional to each other.

Electric	Hydraulic	Thermal	Mechanical
Voltage (V)	Pressure (Pa)	Temperature	Force
Current (q/s)	Flow Rate	Heat Flow	Velocity
Resistance (Ω)	Resistance	Resistance	Friction
Charge (q)	Volume	Heat	Displacement
Inductance (L)	Intertia	N/A	Mass

Electric	Hydraulic	Thermal	Mechanical
Capacitance	Compression	Thermal Capacitance	Compliance

Table 2. Analogies for different physical domains.

The simple analogy presented so far can already be useful for building intuition on the function of simple fluidic systems. For instance, consider the following fluidic system with an incompressible fluid:

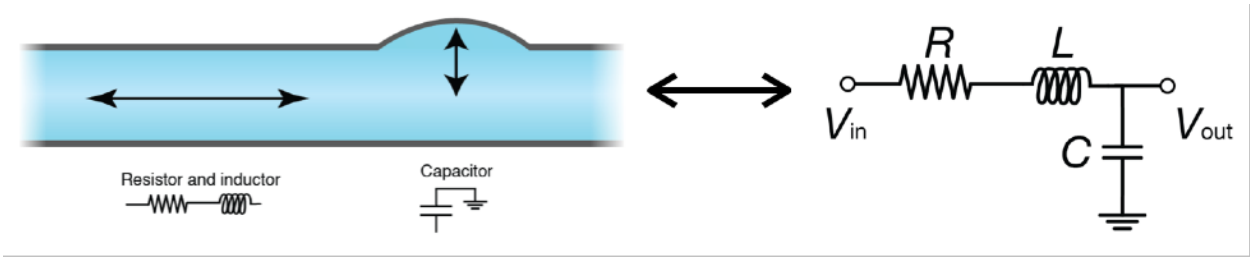

Figure 3.5. Electric-hydraulic analogy for a simple fluidic systems. Both systems behave as a second order low-pass filter.

With only our simplistic, topological perspective on this system, it is evident that it behaves like a series lowpass RLC circuit. As such, lower frequencies will be passed through the system better that higher ones, and resonance will cause a spike in the frequency response, not a dip. Therefore, we can expect the flow rate of this system to be high for lower frequencies, very high for the resonant frequency (assuming low damping), and declining for higher frequencies. This system could serve hypothetically to smooth the flow of water from an erratic, pulsatile pressure source.

Now we will graduate from qualitative analogizing to quantitative analogizing, enabling us to precisely design and characterize fluidic systems. Many models, equations, and analogies have been published in literature, with some being significantly more complex (and perhaps accurate) than others. Based on prior research by Rahil Jain, it was found that a paper from Morris and Forster from the UW Mechanical Engineering department produced accurate quantification of

fluidic resistance and inductance parameters [27]. This paper presents that exact impedance solutions for the Navier-Stokes equations for harmonic flow in a rectilinear channel over frequency [29]. The result is a complex impedance that can be decomposed into resistance and inductance. The equations for these are as follows:

$$\hat{Z}_e = \frac{\mu L \pi^2}{32 b^4} \left[\sum_{n=0}^{\infty} \frac{1}{(2n+1)^2 q_n^2} \left(\alpha - \frac{\tanh(q_n \alpha)}{q_n} \right) \right]^{-1} \tag{3.11}$$

$$q_n = \sqrt{i\eta^2 + \frac{(2n+1)^2}{4}\pi^2} \tag{3.12}$$

$$R_e = \Re[Z_e] \tag{3.13}$$

$$I_e = \Im[Z_e]/\omega \tag{3.14}$$

Where $b = \frac{d}{2}$, $\alpha = \frac{w}{d}$, and $\eta = b\sqrt{\frac{\omega}{\nu}}$, and v is the kinematic viscosity.

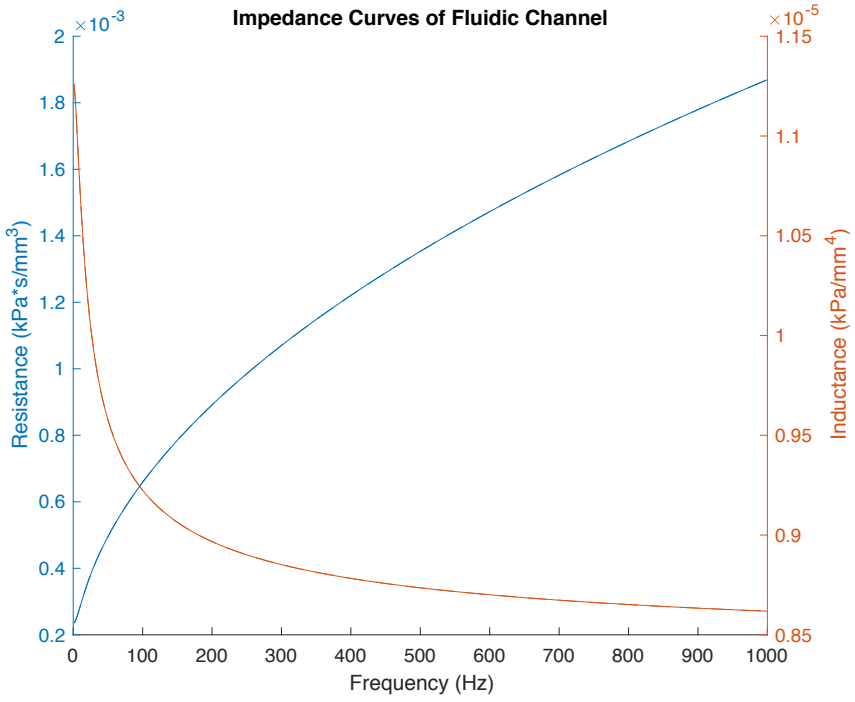

Figure 3.6. Resistive and inductive impedance values over frequency.

It is important to note the resistance and inductance values of a fluidic circuit are frequency dependent, as plotted above. This means that fluidic analogues to RLC circuits are actually nonlinear, which technically defies its classification as an LTI system, invalidating system analysis using frequency responses and transfer functions. However, approximating constant resistance and inductance values by averaging the impedance function across a 1 kHz bandwidth has proved effective at linearizing fluidic systems through experimental confirmation. As long as the frequencies in an input pressure signal lie within that averaging bandwidth of 1 kHz, the quantitative values of fluidic resistance and inductance can be accurately modeled.

Capacitance is the remaining fluidic impedance component. In the context of fluidic systems, it is usually described through distributed elasticity of a fluid channel. For instance, the Windkessel effect is a classic medical term that describes the smoothing of blood pressure that occurs due to the high elastic compliance of the aortic artery. In this case, compliance is a property inherent to the arterial walls, and is thus a distributed element. In contrast to distributed elements are lumped elements, which simplify systems into topologies consisting of discrete elements. This is usually how capacitors are expressed in electrical RLC circuits. In order to create a discrete capacitor, an isolated, deformable cavity can be produced in a fluidic system, while all other channels retain rigid walls. Other work, such as that from the groups of Landers and Begley, have proposed simple equations for capacitance of an elastic vessel or element [30]. However, prior work from Rahil Jain has found these capacitance models inaccurate [27]. The capacitance of such fluidic capacitors can be found by the pressure-deformation relationship of a circular membrane and rearranging terms to meet the desired units of volume over pressure (V and $\delta_{\max}$ expressions are from Landers [31]):

$$V = \frac{\pi a b \delta_{\max}}{3} \tag{3.15}$$

$$\delta_{\max} = \frac{3pa^4/2\bar{E}h^3}{3 + 2(a/b)^2 + 3(a/b)^3} \tag{3.16}$$

$$\bar{E} = \frac{E}{1-\nu^2} \tag{3.17}$$

For a = b,

$$\delta_{\max} = \frac{3pr^4/2\bar{E}t^3}{8} = \frac{3pr^4}{16\bar{E}t^3} \tag{3.18}$$

$$V = \frac{\pi ab3pr^4}{48\bar{E}t^3} = \frac{\pi pr^6}{16\bar{E}t^3} = \frac{\pi pr^6(1-\nu^2)}{16Et^3} \tag{3.19}$$

$$C = \frac{dV}{dP} = \frac{\pi r^6(1-\nu^2)}{16Et^3} \tag{3.20}$$

Since the above expression for fluidic capacitance is novel, testing and simulations were used to verify its veracity. Various theoretical capacitance values produced by this expression were compared with two practical capacitance values: those uncovered by prior work, and those derived from simulations. In prior work on AC fluidic technology, capacitance values for fluidic circuit components were found by fitting the parameters to observed circuit resonant frequencies against known resistances and inductances [27]. This produced a lookup table of fitted capacitances that was used in the design of fluidic circuits at the time. A simulation of a fluidic capacitor in the COMSOL software produced capacitance values that closely correspond to the fitted capacitance values. The geometry of the model comprises a disk that represents a capacitor membrane. The radius of the clot is discretely swept between 3 and 4.5 mm in increments of 0.5 mm in order to compare the simulated capacitance values to the empirical findings of prior work. The material of the membrane is PMMA. A fixed pressure of 1 kPa is applied to the bottom of the membrane in order to induce deformation, and fixed boundary conditions are applied to the sides of the membrane to simulate the mechanical fixation of the capacitor. Using 1 kPa allows the deformation to be directly converted to capacitance in the $\frac{\text{mm}^3}{\text{kPa}}$ unit which is standard in this work. The COMSOL model configuration is described in closer detail in appendix A.

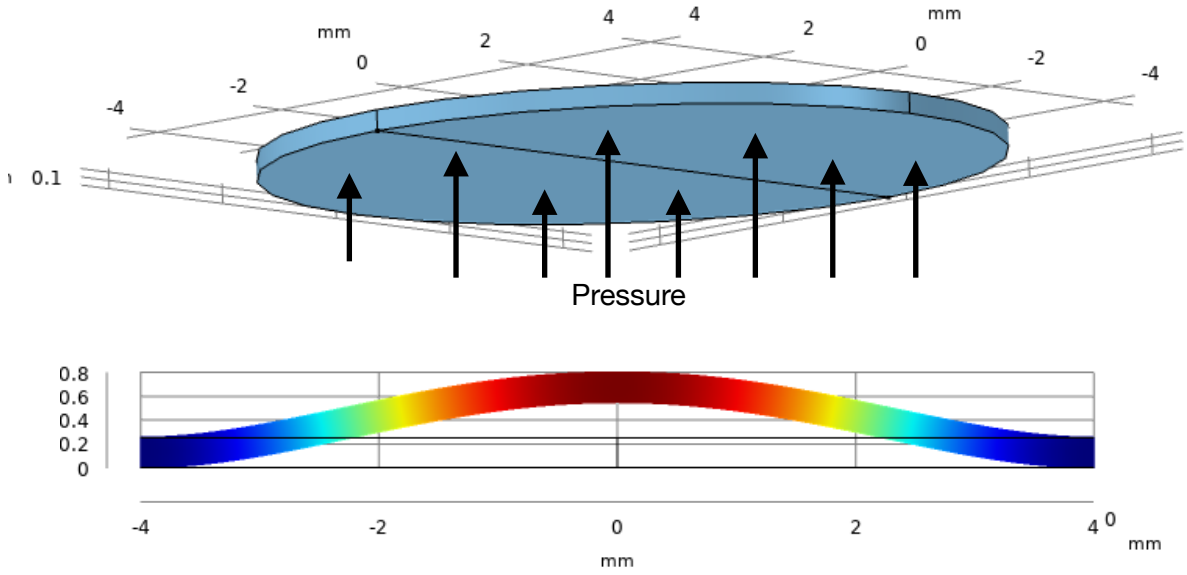

Figure 3.7. Geometry of COMSOL simulation. Top shows a three-dimensional depiction, and bottom shows a cross-section with exaggerated deformation.

Regardless of whether one lends more credibility to fitting or simulation as a method of determining capacitance, both results are similar. The theoretical values produced by the novel capacitance expression match well to both the simulated and fitted values, supporting its accuracy.

Thickness (mm)	Radius (mm)	Prior Findings [24] (mm^3/kPa)	Simulation (mm^3/kPa)	Cap Expression (mm^3/kPa)
0.254	**3**	0.0023	0.0022	0.0024
	3.5	0.0075	0.0056	0.0062
	4	0.0156	0.0125	0.0137
	4.5	0.0276	0.0256	0.0279

Table 3. Comparison of different capacitance values to support accuracy of analytical model.

The only other question at stake is whether or not fluidic capacitances behave linearly, unlike resistance and inductance, which we average across frequency for the sake of linearization.

Using a similar simulation in COMSOL, where a pressure input is varied into a capacitor, the resulting volume deformation appears to be highly linear. Furthermore, there is no suggestion from the analytic capacitance expression that fluidic capacitance is nonlinear or would change with respect to pressure amplitude, frequency, or phase. Hypothetical causes of potential nonlinearity could be mechanical inertia and resistance from the membrane forming the expandable capacitor element, or the inertia and viscous behavior of water flowing through the capacitor space. Both of these situations are considered negligible on account of the analytic and simulation evidence for fluidic capacitor linearity.

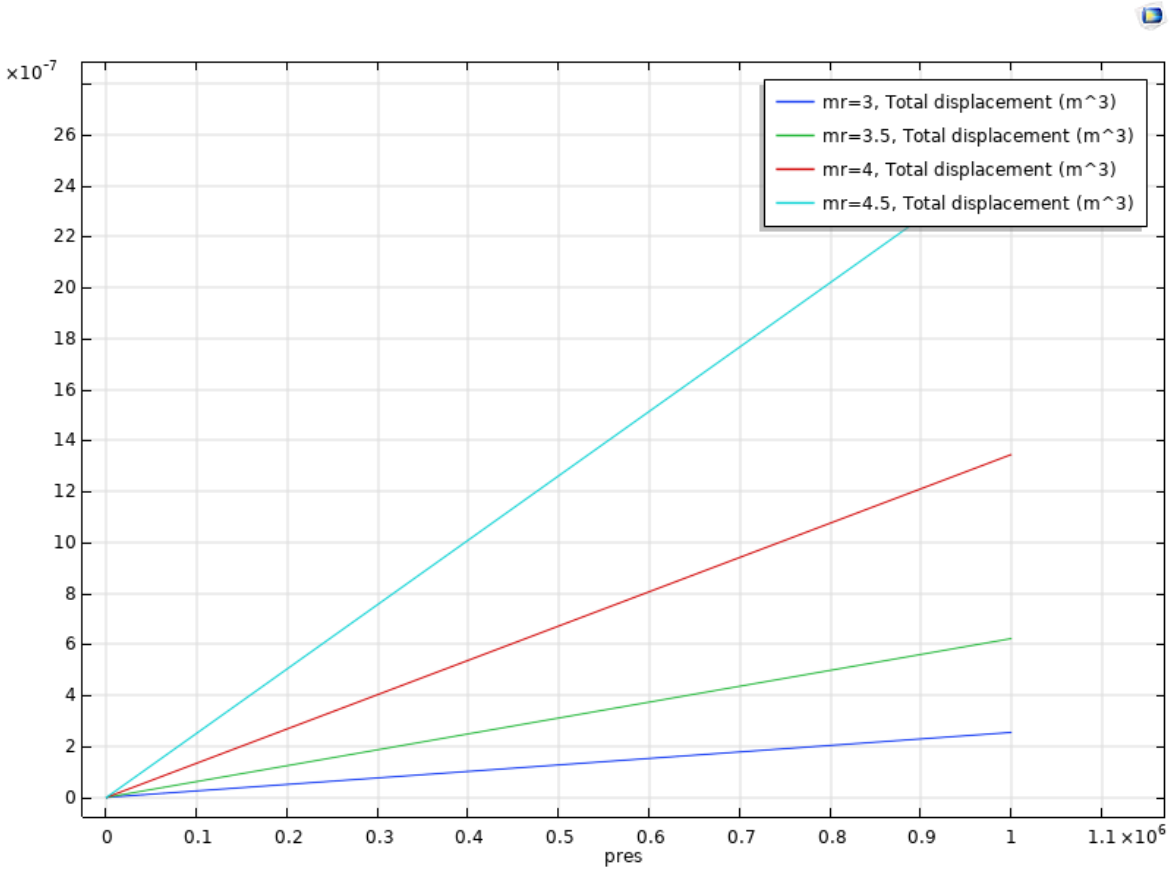

Figure 3.8. Linearity of capacitance allows membranes to be treated as capacitors.

The capacitor linearity COMSOL model was implemented using the same geometry as the prior capacitance simulation, but the input pressure to the capacitor is linearly swept from 0 to 1 kPa.

The displacement values are then sorted by the associated membrane radius and plotted, producing the lines in the figure above.

3.5 Device Fabrication

The fabrication process consists of cutting fluid channels into acrylic pieces, and stacking them on top of one another. The stacking action of the device does not let series capacitors be easily implemented without multi-layer fluidic systems, let alone capacitors with integrated piezo buzzers. The design of the fluidic systems comprises layers of different plastics stacked upon one another and bonded using adhesive. Some layers are thick are rigid, allowing structural support and carvings for channels and components, while other are thin and flexible, producing a surface on which capacitor behavior can occur. The simple AC fluidic system has the following layers:

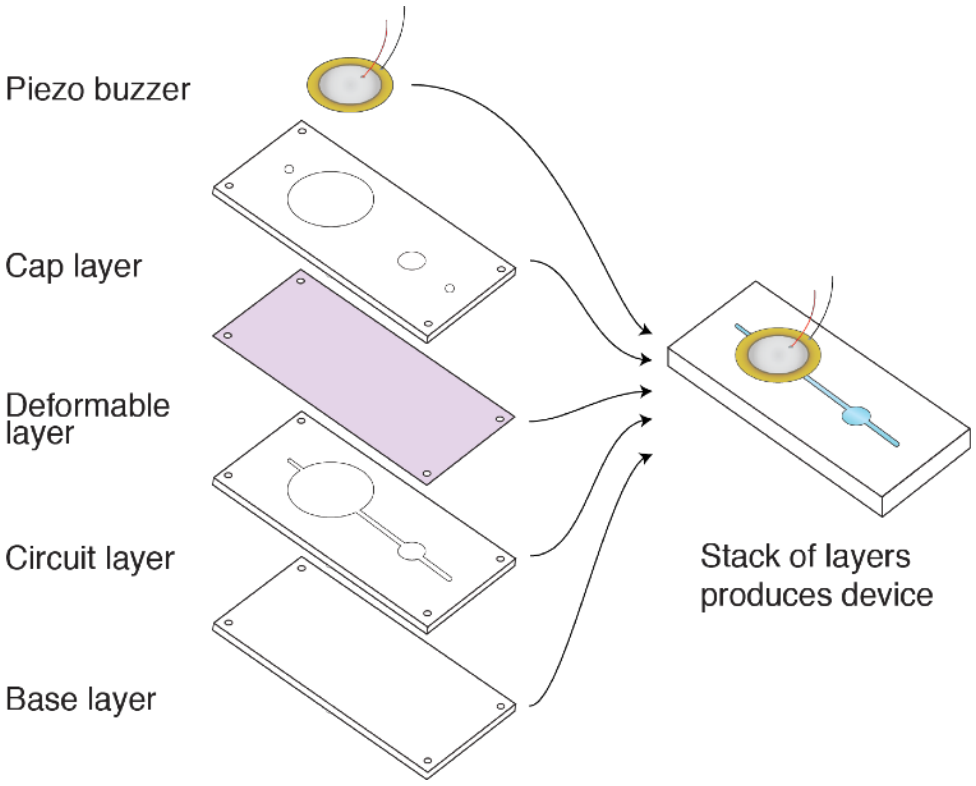

Figure 3.9. Layers stack to produce fluidic circuits.

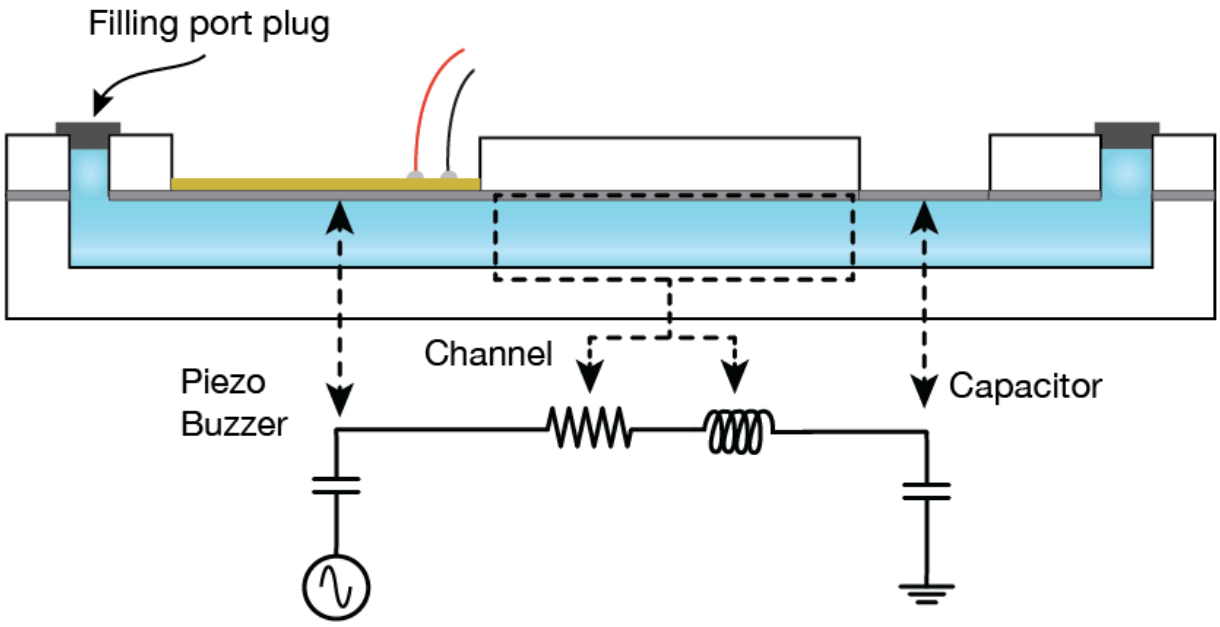

Figure 3.10. Electric-hydraulic analogy applied to this method of fluidic circuit fabrication.

The layout of each layer is specified in AutoCAD, and then a CO_2 laser is used to cut the layers. The cutting tolerances are low enough that the frequency-responsiveness of the systems are consistent. Base layers, circuit layers, and top layers are all made of acrylic (PMMA). The thickness of the top and bottom layers are not particularly important, but the thickness of the circuit layer is important, because it determines the height of the flow channels. The thickness of each acrylic layer is inherent to the sheets, and is specified in orders from our supplier (McMaster Carr). Deformable layers are made from thin material, such as Rohaglas or Mylar. The four corners of each layer feature small, circular cutouts where the layers can be aligned on a set of pins, enabling easy application of adhesives. Adhesion between layers was achieved by using PDMS tape. Layers were cleaned with isopropyl alcohol before the application of each layer of tape, and the bonding occurring under a pressure of 1500 psi for several seconds.

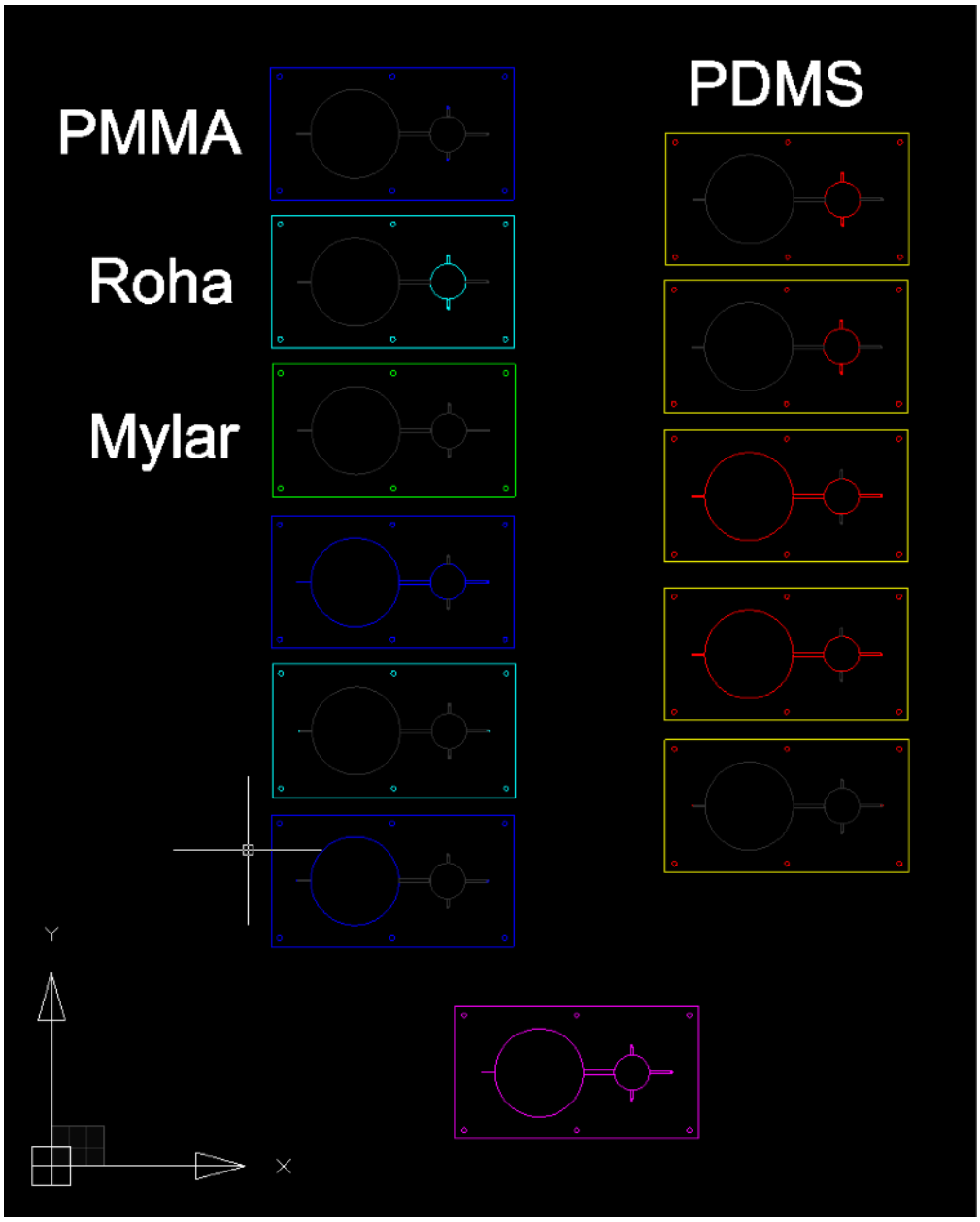

Figure 3.11. AutoCAD fluidic circuit design files. Master circuit layer is shown in magenta at the bottom, from which all other layers are derived. Different colors correspond to the different materials indicated. Gray indicates areas of no cutting.

All piezoelectric transducers (referred to as “piezo buzzers” for brevity) used in our fabrications were unimorphs with brass backing plates. The piezo buzzers used in the AC fluidic systems were applied to exposed patches of adhesive on the top layer. In order to not crack the PZT crystals within the buzzer, only gentle fingertip pressure was used during the application

procedure. This cartridge does not include vibration dampening measures, as the resonance signals observed in the cartridge are not thrown off by external vibrations.

3.6 Practical Limitations of Fluidic System Design

One important caveat to fluidic system design is the inevitable bundling of certain "RLC" components together. Electrical circuits are very convenient to design, because any R, L, or C component can be independently added to the circuit in any possible topology and permutation. However, the physical realities of fluidic circuits results in practical components that do not behave as discrete resistors, inductors, or capacitors, but rather, as series collections of multiple components. For example, if it is desired to add a resistor to a fluidic system, one may accomplish this by directing the fluid through a narrow channel. Although there is a significant resistance associated with this narrow fluidic channel, a nontrivial inductance will also be present therein. In this manner, resistors and inductors are always serially coupled in fluidic circuits, so there is no adding one without the other. Likewise, simple capacitors are always serially coupled in fluidic systems to ground potentials. It is theoretically possible to produce fluidic capacitors with fluid on both sides in order to remove the grounding effect, but this was never attempted.

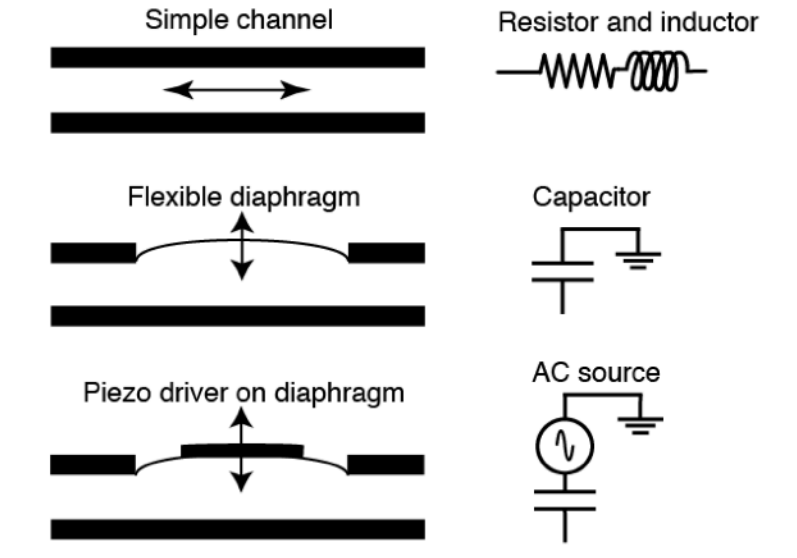

Figure 3.12. Necessary clusters of fluid circuit components due to physical and fabrication limitations.

3.7 Instrumentation for AC Fluidic Systems

If the focus of this work were solely electrical RLC circuits, then powering and instrumenting such systems would trivial. Electrical oscilloscopes, multimeters, power supplies, and function generators can be used to easily power and probe electric circuits. Unfortunately, the same luxury does not exist for AC fluidic systems. The fluidic analogies to electrical instrumentation, such as differential pressure transducers and flow meters, are generally large and cumbersome. Furthermore, these piece of equipment are generally expected to be capable of interfacing with an electrical system of some kind, typically for management or measurement of the fluidic system.

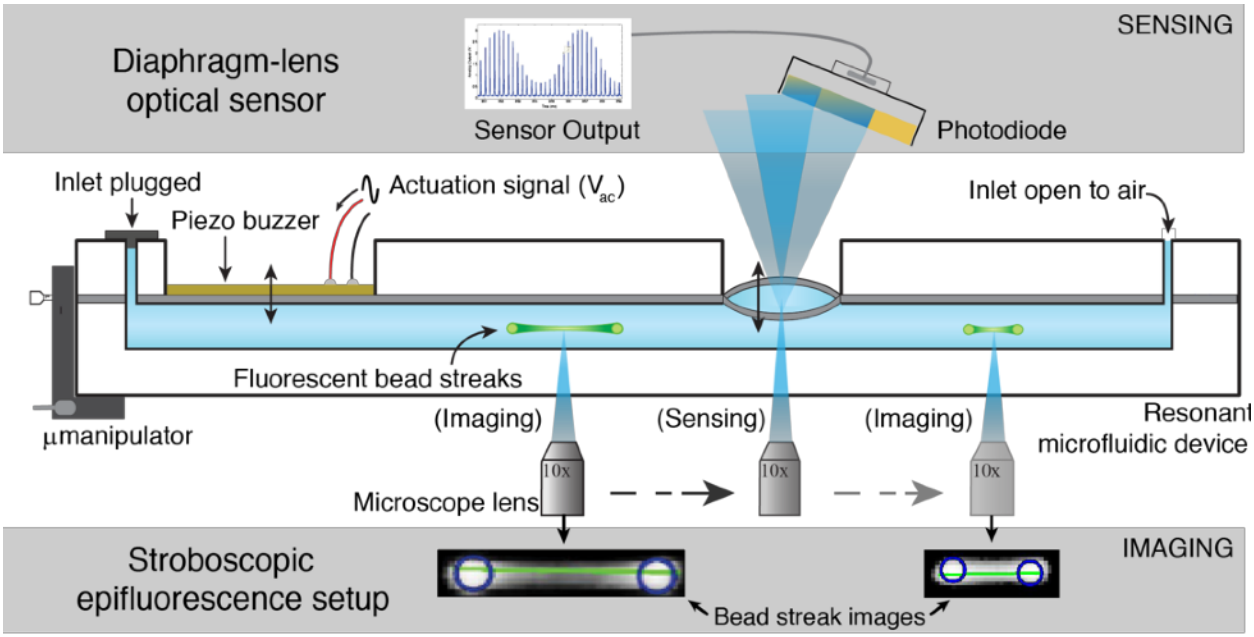

Figure 3.13. Methods of instrumentation utilized in prior work on AC fluidics.

In order to measure the pressure and flow activity within the system, optical instrumentation solutions have previously been engineered by Rahil Jain [27]. The two are epifluorescence flow tracking and capacitor-deflection measuring. Although these two methods worked for obtaining data from the fluidic systems, they are not suitable for instrumentation in a POCT medical device on account of their delicacy, complexity, and challenging signal processing. Both of these

instrumentation methods require delicate optical setups, as well as time-intensive post-processing to obtain information about frequency, magnitude, and phase. These expensive instrumentation methods significantly reduce the viability of the devices to ever become POC coagulation analyzers. In fact, these instrumentation methods result in a setup that is about on par with TEG in terms of POC versatility.

3.8 Utility of AC Fluidic Systems for Measuring Viscoelasticity

By this point in our understanding of AC Fluidics, there still remains a significant question: how does this help us measure the viscoelasticity of whole blood samples? In fact, there are very clever methods of doing this measurement. In the next chapter, we will explore the design of a fluidic system optimized for this very purpose.

Chapter 4: Fluidic Circuit Design

4.1 Contents

This chapter will cover how the fluidic circuits were designed to be instrumented, as well as how they were designed to measure blood clot elasticity. This consists of how the system was designed for use with piezoelectric transducers, as well as how the system was designed to maximize its ability to measure clot elasticity.

4.2 Piezoelectric Transduction

The theoretical basis that allows us to use piezo buzzers as both inputs and outputs to fluidic circuits is reversible transduction. Reversible transduction is the idea that many transducers used in the physical world work bilaterally. For example, antennas can be used to both broadcast and receive EM waves. Dynamic audio drivers can be used to both produce and record audio. Buoys can both be influenced by ocean waves and produce waves themselves. As long as the physical relationships that govern the behavior of the transducer are invertible in some way, a transducer is reversible.

In many applications, invertible transduction can be undesirable, because it can reduce the regulatory specificity of the transducer. For instance, if an audio speaker was also receiving acoustic feedback that interfered with the electrical amplification, that would be bad speaker design. This is why speakers and microphones, although very similar in their mechanical underpinnings, are very differently optimized. The same rules must apply to using piezoelectric buzzers as both sources and sinks for fluidic activity.

In order to understand the role of the fluidic buzzers as both sources and sinks, it would help significantly to have a model that helps us understand this transduction. Whereas prior work on AC fluidics treated piezo elements as a fitted-parameter pressure source, using piezo elements in more nuanced ways mandates more general information [26, 27]. In *Acoustics* by Leo Beranek, a

transduction model is given for electrostatic electromechanical transducers, such as piezoelectric crystals, which is relevant to our fluidic circuits.

A force applied uniformly over the face of a crystal causes an inward displacement. As a result of this displacement, a voltage appears across the electrodes of the piezoelectric crystal. For small displacements, the induced voltage is proportional to displacement. The inverse of this effect occurs when no external force acts on the crystal face but an electrical generator is connected to the terminals. If the external generator is connected, an internal force is produced which acts to expand the crystal. For small displacements (ξ), the developed force is proportional to the electric charge (q) stored in the electrodes.

$$\tilde{q} = C_E \tilde{e} - d_{31} \tilde{f} \tag{4.1}$$

$$\tilde{\xi} = d_{31} \tilde{e} - C_M \tilde{f} \tag{4.2}$$

Although this description of the electrostatic transducer model may seems simple, there are important nuances to understand. First of all, the electrical capacitance and mechanical compliance vary with displacement, but it is assumed that the displacement is very small, so these are linearized equations. Second, the above equations result in a circular problem where displacement also leads to an induced charge on the electrodes, which in turn leads to a voltage, which conversely applies an electrical voltage, leading to a mechanical force. Assuming small displacements and deflection following Hooke's law, the force ($\tilde{f}$) and electrical ($\tilde{e}$) behavior of the piezoelectric element can be stated in a z-parameter matrix form:

$$\begin{bmatrix} \tilde{e} \\ \tilde{f} \end{bmatrix} = \begin{bmatrix} \frac{1}{j\omega C_E'} & \frac{d_{31}}{j\omega C_E' C_M} \\ \frac{d_{31}}{j\omega C_E' C_M} & \frac{1}{j\omega C_M'} \end{bmatrix} \begin{bmatrix} \tilde{i} \\ -\tilde{u} \end{bmatrix} \tag{4.3}$$

Under open-circuit conditions for $\tilde{f}$ or $\tilde{e}$, the following potentials are created:

$$\tilde{f} = \frac{d_{31}}{C_M}\tilde{e} \tag{4.4}$$

$$\tilde{e} = \frac{d_{31}}{C_E}\tilde{f} \tag{4.5}$$

The takeaway is that the impedance of the piezo element must be handled correctly in driving circuitry to maintain linearity between electrical potential and the force on the piezoelectric element, because the piezo buzzer transduction model changes depending on whether the electrical side of the buzzer is short-circuited or open-circuited. In order to prevent electromechanical feedback from interfering with desired measurements, the load impedance of the piezo buzzer must be managed. The choice between the two simplified models is usually based on the desired mode of operation. When short circuited, a piezo buzzer linearly translates electrical potential to a mechanical force based on the piezoelectric coefficient and mechanical compliance of the buzzer. If the piezo buzzer is serving as a voltage source, the electrical terminals must look like an open circuit for maximally linear force signal transduction, and instead of mechanical compliance being at play, the electrical capacitance is at play. Therefore, as long as the driving circuitry can dynamically alter its impedance, a single piezoelectric element can be used as a pressure-to-voltage transducer in either direction. The design of this piezo driver is detailed in chapter 5, section 5.

This also demonstrate that the area of the piezo electric buzzer is of significance in determining its performance. Since fluid mechanics are based on pressure, but piezoelectric materials are force-based, a larger piezo buzzer area will produce a greater signal for a given fluidic pressure due to the relative increase in force.

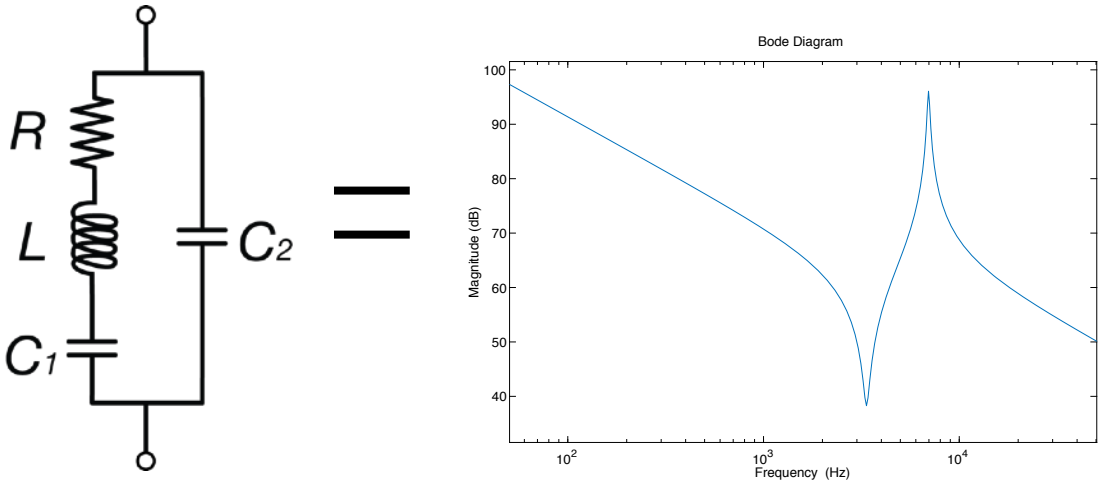

Figure 4.1. Butterworth-Van Dyke model with corresponding impedance curves.

The Butterworth-Van Dyke model of an unloaded piezoelectric buzzer shows an electrical capacitance and a mechanical resonance. The series RLC arm of the model comes from the classic spring-mass-damper type mechanical characteristics of the piezoelectric crystal. The capacitor in parallel to the RLC comes from the electrical capacitance created when two electrodes are mounted to opposing faces on a dielectric body. Due to the piezoelectric coupling of electrical and mechanical forces in the crystal, impedances from both the electrical an mechanical domain contribute to the net electrical impedance. This means that a piezo buzzer will have a series resonant frequency from the series mechanical RLC, and a parallel antiresonance from the combination of electrical capacitance and mechanical inertia (inductive). Both of these resonance behaviors are strictly undesired in fluidic circuit application, as piezo resonance could corrupt the ability of the piezo buzzer to measure fluidic circuit resonance. Piezo buzzers chosen for this system must not resonate within the 1 kHz AC fluidics bandwidth; as long as the two resonant frequencies occur above 1kHz, the frequency response of the piezo should be relatively flat.

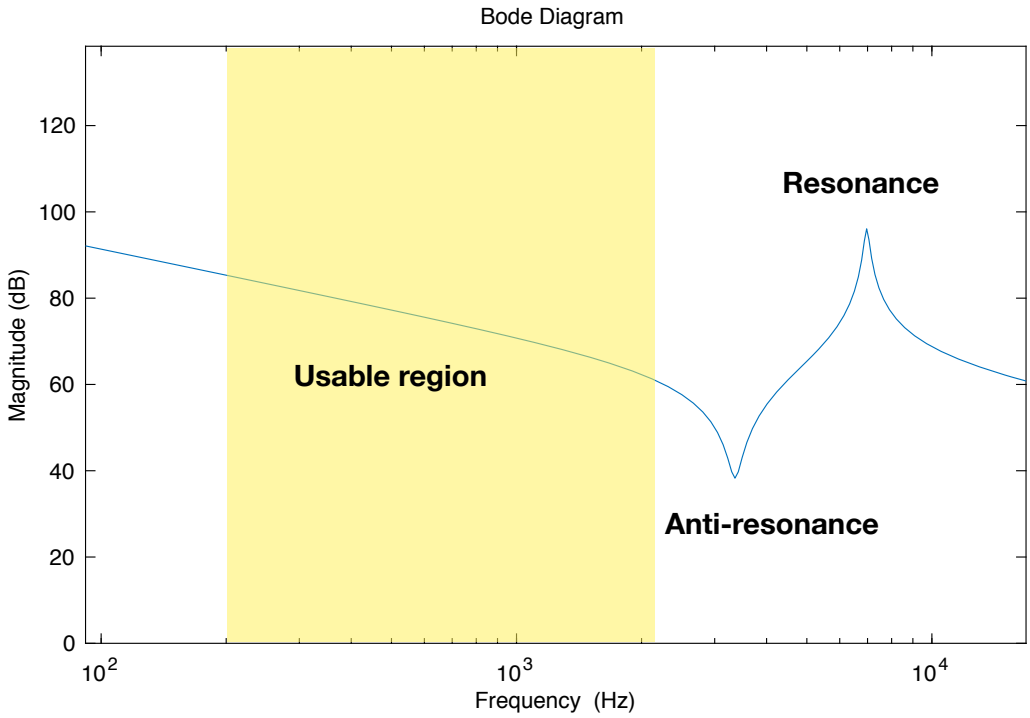

Figure 4.2. Usable region of a piezo buzzer preceding the resonant frequency.

Unfortunately, there is a conflict of goals here. We desire a large-diameter piezo buzzer in order to increase transduction sensitivity, but we also desire a high resonant frequency of the piezo buzzer. Increasing the diameter of a piezo buzzer increases its mechanical compliance and its mass, resulting in significant decreases in resonant frequency. A piezo buzzer that finds a compromise between these two goals, the Murata 7BB-20-6L0 was chosen for its large 20 mm diameter while having a 6.3 kHz resonant frequency, plenty above the 1 kHz cutoff specified. Since the series and parallel resonant frequencies of a piezo buzzer are usually close together, it is highly unlikely that the parallel resonance would be lower enough than 6.3 kHz to approach 1 kHz. The electrical capacitance of the 7BB-20-6L0 is specified at 10 nF at 1 kHz. This capacitance is rather large, but workable, as the output current of the piezo driver is high enough to fully charge it, and the input impedance of the piezo amplifier is designed to allow timely RC discharge of the piezo buzzer, as shown in chapter 5.

4.3 Incorporation of a Piezoelectric Transducer in a Fluidic Circuit

In order to utilize piezoelectric buzzers as an input and output transducers in fluidic circuits, a topological design must be made to incorporate the buzzer/s. To do this, two things must be understood about them:

1. The hydraulic circuit component analog produced by incorporation of piezoelectric buzzers in fluidic circuits.
2. The type fluidic measurements taken by piezoelectric buzzers (does it work like a pressure or flow meter?).

To the first item- since piezoelectric buzzers are attached to fluidic circuits by an adhesive layer in capacitor-esque cavities, unpowered piezoelectric buzzers generally behave like a capacitor in the fluidic circuit. This piezo-derived capacitance will exist in the fluidic circuit along with the clot-derived capacitance, which introduces the potential for one capacitance to dominate the other. If the dominating capacitance comes from the piezo buzzer, then changes in the fluidic capacitance will produce little difference on overall circuit resonance. Therefore, if the piezo and clot capacitors are to be placed in series, then the piezo capacitance should ideally be significantly (about one order of magnitude) larger than the clot capacitance. Conversely, if the two are to be placed in parallel, then the piezo capacitance should be significantly smaller than the clot capacitance. The above design considerations ensure that the clot capacitance is what characterizes the behavior of a fluidic circuit, which is necessary in order to use the system as a clot-measuring tool.

The second item, on the measurement style of piezo buzzers in fluidic circuits, is important for designing circuit topologies with regards to piezo placement. Piezoelectric buzzers behave as electro-mechanical transducers, as described in section 4.2. However, a fluidic instrumentation analogy is still needed to properly design a fluidic circuit with an output buzzer. The instrumentation analogy question is: do output piezo buzzers behave as pressure meters

(voltmeter analogy) or flow meters (ammeter analogy)? The answer will help to determine the best fluidic circuit topology to produce a strong, frequency-modulating resonance output while ensuring minimal loading effects on the remainder of the circuit from the output piezo.

In practice, the electrical output of the piezoelectric buzzer will be similar regardless of its propensity to measure pressure or flow, since the only major difference between the voltage and current responses of an RLC circuit is the presence of DC in the voltage one. Nonetheless, piezoelectric elements have deleterious internal resistances that cause a constant loss of charge, so they cannot truly be used to measure static forces. This fact, combined with the low fluidic impedance of the highly-capacitive piezo buzzer led to the hypothesis that piezoelectric buzzers are best treated as flow meters (or ammeters in the electric analogy).

With the ammeter hypothesis having been made, the only remaining fluidic circuit design question is how to produce resonance. RLC resonance manifests in different ways depending on whether the L and C components are in series or in parallel. These differences in resonance are often utilized to create maxima or minima in the frequency response of a circuit, but both types are equally valid to measure. In this application, series resonance was predicted to be more favorable, as it allows the hypothetically superior piezo ammeter to be easily implemented in series with the RLC components.

Although ammeters and series resonance were hypothesized to produce the best results, each topology combination was designed and experimentally evaluated for the sake of definitive closure on this matter. Circuit designs were made to maximize the amplitude of the step response by keeping resistances low. Time domain step response results are shown between a fluidic circuit model and reality, and frequency domain model results are shown before and after the capacitance of the circuit is decreased, emulating a clot forming. Analog data collection was done using a Tektronix DSO. Plots with white backgrounds are model simulations, and images with black backgrounds are oscilloscope screenshots. The TD plot monicker refers to time domain signals, and FD refers to frequency domain signals. At this stage in this work, the piezo

driving for each circuit was done using a bench top function generator, and the piezo reading comprised of simple, obsolete analog front-ends.

Series Resonance Voltmeter

The following is the fluidic circuit design for the best-performing fabricated series resonance voltmeter:

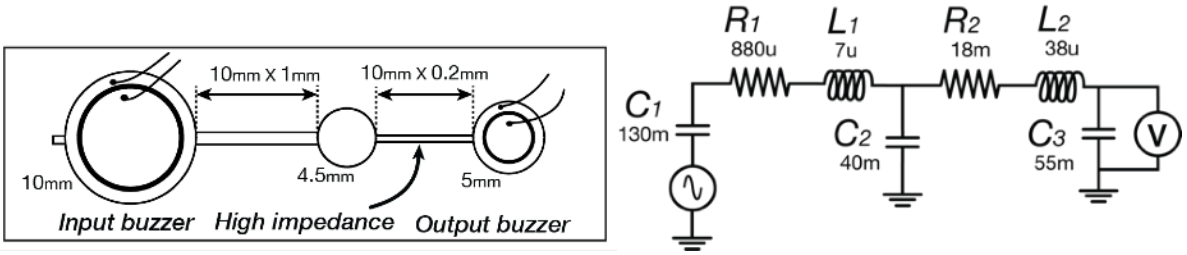

Figure 4.3. Series resonance voltmeter design. Fluidic (left) and electric (right).

In order to effectively implement this fluidic circuit design, the classic design tenants of electrical voltmeters were considered. Since voltage is a potential, as opposed to current, which is charge flow, voltage can be measured by probing a load in a circuit in parallel. The impedance of an ideal voltmeter is infinitely high, so that no current is drawn by it. If a voltmeter drew current from a circuit load after being placed in parallel to that load, the reduction in current across the circuit load would change the actual voltage drop across that element, such that the circuit no longer behaves as expected. Therefore, the implemented voltmeter output of a fluidic circuit must exist in a high impedance channel. Although the high impedance RL channel is not actually measured by the piezo voltmeter, is was found to be necessary to avoid the accidental creation of an ammeter.

Electric-hydraulic analogy modeling was used to help produce an effective fluidic voltmeter design. Of the three elementary impedances: resistance, inductance, and capacitance, resistance is the most desirable parameter to increase for a voltmeter channel, because it has no frequency dependence. This can be achieved by producing a small area channel that leads to the output piezo buzzer. However, decreasing the area of a channel also increases its inductance, which can

be large enough to produce significant, deleterious low frequency resonance when placed in series with the output buzzer capacitor. In addition, since the piezo buzzer element behaves as a capacitor, increasing the resistance value of the preceding channel by a very large amount will sacrifice the bandwidth of the output piezo buzzer.

This conflict of interest between the need for high voltmeter impedance and the resultant deleterious resonance and RC characteristics creates an optimization problem for choosing channel area. Setting the area to be too large results in a bypass of the central fluidic capacitor, significantly reducing the sensitivity of the system to changes in that capacitance, and causing high quality-factor resonant ringing that is not associated with the central capacitor. However, settings the area to be too low results in an overdamping of the system with poor RC characteristics, resulting in low sensitivity to center capacitor ringing.

Demonstrative of these issues, a circuit with the specifications in figure 4.3 was produced. The step response of this circuit was observed to contain both deleterious ringing and a small amount of desired ringing. Applying a gentle pressure to the capacitor to reduce its capacitance resulted in the disappearance of most of the visible desirable ringing, as the sharp corners of the deleterious ringing rounded off. The very small amplitude of the desired ringing at that point was practically indiscernible from the high amplitude deleterious low frequency ringing. This spells trouble for the effectiveness of this design topology.

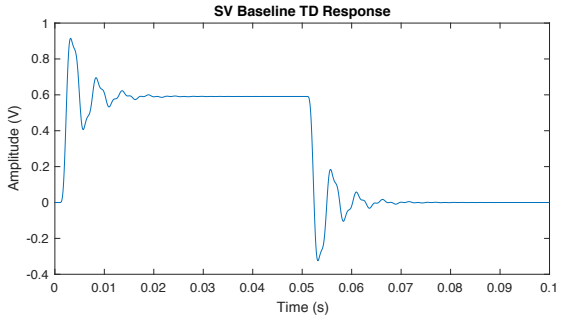

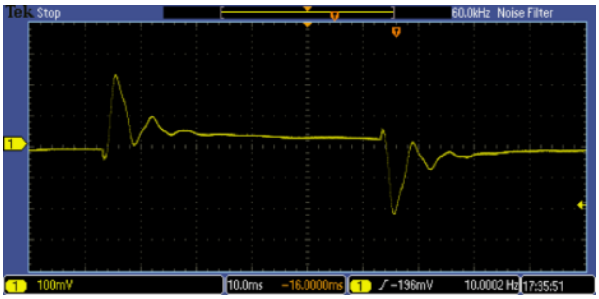

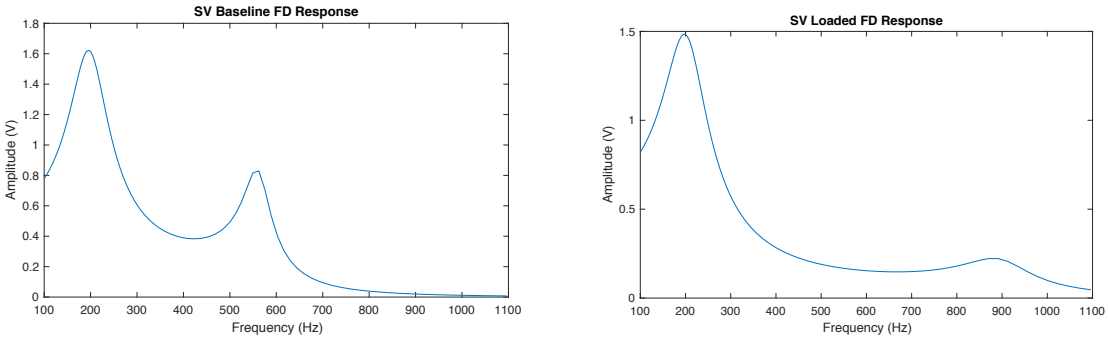

Figure 4.4. Series resonance voltmeter performance. Modeled step response (upper left); real step response (upper right); modeled step response frequency domain (lower left); modeled step response frequency domain with modulation (lower right).

Similar to how odd harmonics of a triangle wave produce sharp peaks, the 200 Hz dominant resonance and the tripled 600 Hz inferior resonance produce a rudimentary triangle wave. After capacitance reduction, the frequency changes, phase shifting, and amplitude attenuation of the inferior resonance significantly reduces the appearance of the output as a triangle wave. The domination of the system by the unchanging resonance associated with the high impedance channel results in this fluidic circuit implementation being of poor instrumentation performance.

Parallel Resonance Voltmeter

The following is the fluidic circuit design for the best-performing fabricated parallel resonance voltmeter:

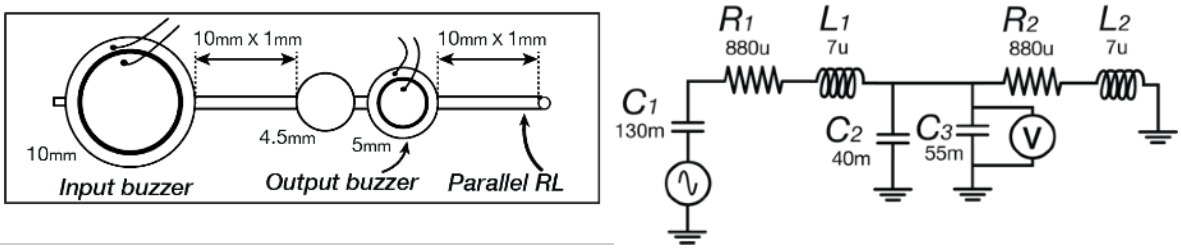

Figure 4.5. Parallel resonance voltmeter design. Fluidic (left) and electric (right).

The principle advantage of this topology is that the dominating resonance is associated directly with the sample-receiving capacitor, whereas the inferior resonance is associated with the two piezo elements. This means that the inferior resonance is low in amplitude, and low in

frequency(~100Hz). The combination of low frequency and low amplitude results in manageable low frequencies that can be addressed by high-pass filter.

However, there are two major disadvantages to this circuit:

1. The sample-receiving capacitor is in parallel with a much larger output buzzer capacitance, rendering the net capacitance of the dominant resonance rather large, as net capacitance for parallel capacitors is the sum of each one's capacitance. This results in the loading of the sample capacitor producing a rather small effect on the frequency shifting.

2. The open ground inlet is prone to leakage, producing bubble that shunt the impedance of the parallel channel. This significantly reduces the inductance component of the resonance, thereby compromising the resonance advantages of the parallel resonance topology.

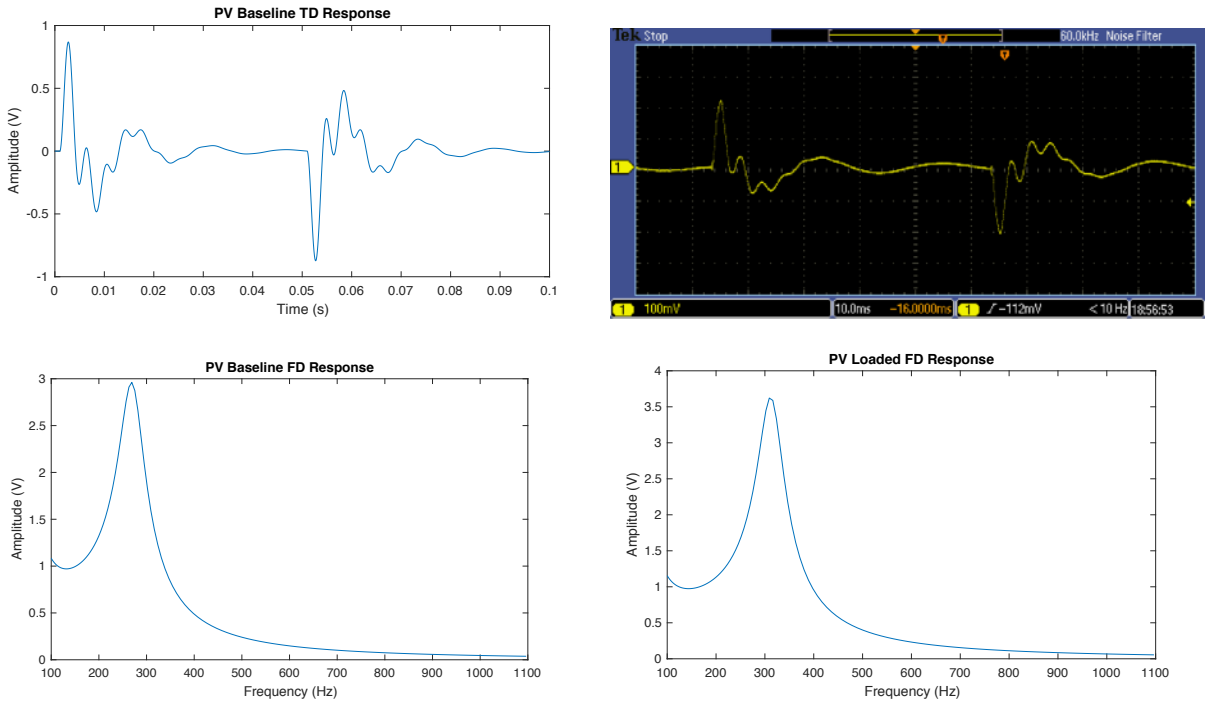

Figure 4.6. Parallel resonance voltmeter performance. Modeled step response (upper left); real step response (upper right); modeled step response frequency domain (lower left); modeled step response frequency domain with modulation (lower right).

Although there is clear ringing that is captured, the frequency modulation range is quite small. For subtle changes the material firmness of a blood sample, this fluidic circuit design would require a heavier signal processing overhead in order to have very high frequency resolution to detect such subtle changes. In addition, the open ground port significant complicates the mechanical robustness of the device. Although this is a viable design, it is far from optimal.

Parallel Resonance Ammeter

The following is the fluidic circuit design for the best-performing fabricated parallel resonance ammeter:

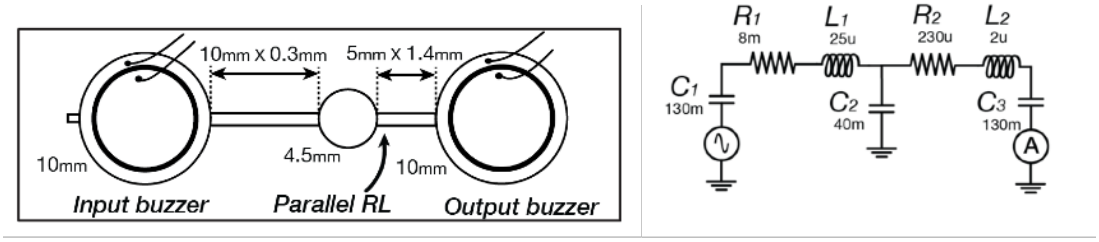

Figure 4.7. Parallel resonance ammeter design. Fluidic (left) and electric (right).

This topology is theoretically more suitable for a measurable fluidic circuit, because it increases the flow rate across the output buzzer, increasing output signal if the piezo buzzer serves as an ammeter. Ideally, the output buzzer in this circuit should behave like a conductor to ground, which is why a large, high capacitance buzzer is useful for this application. It will read any fluid flow that bypasses the capacitor.

One inevitable problem that will be encountered in parallel resonance circuits is the intrusion of low-frequency parasitic resonance to the system, as was seen in the voltmeter designs. In this design, the low frequency parasitic resonance is actually worse than in the parallel voltmeter setup, due to the covering of the ground port with a piezo buzzer. However, this parasitic resonance does not actually behave in a truly parasitic manner, as it can modulate from changes in system capacitance. This results in two resonance signals being output from this circuit, both of which modulating in response to capacitance changes.

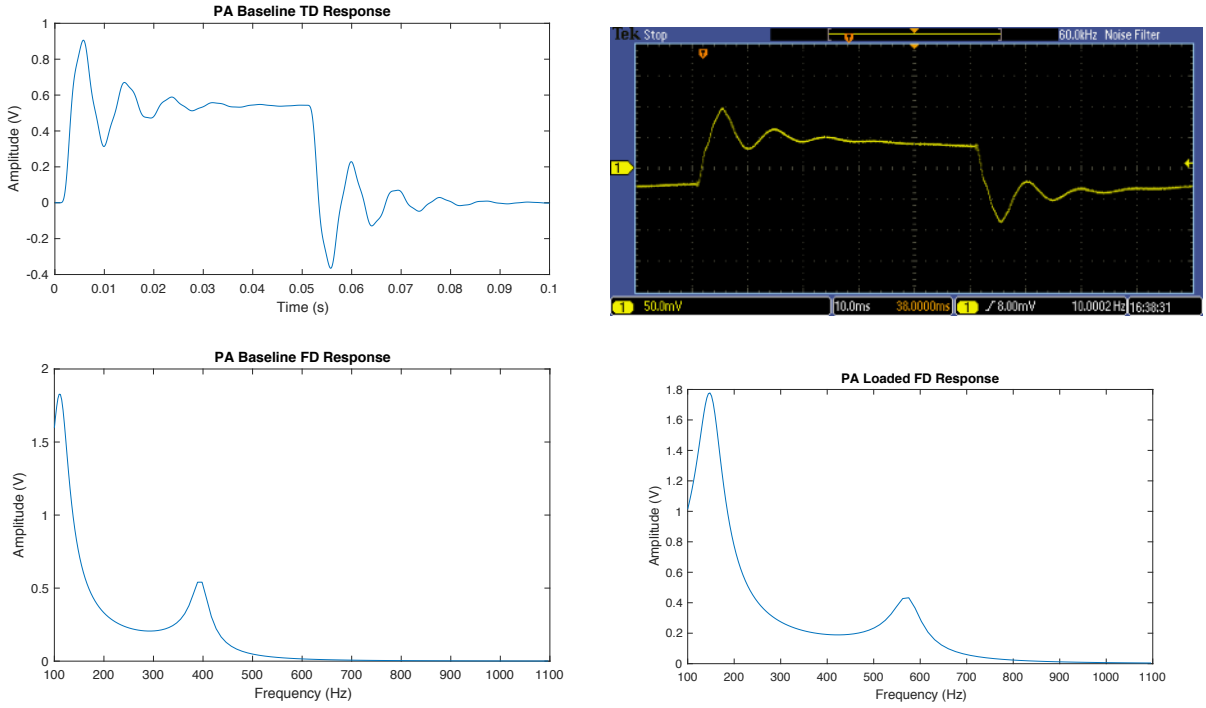

Figure 4.8. Parallel resonance ammeter performance. Modeled step response (upper left); real step response (upper right); modeled step response frequency domain (lower left); modeled step response frequency domain with modulation (lower right).

This circuit shows shifts in the lower frequency resonance that are easy to resolve without significant signal processing. Therefore, this circuit topology is both viable, and a contender for the best instrumentation topology. The largest downside to this circuit is the even poorer modulation range than the parallel voltmeter design. However, if we implement DSP solutions that are sensitive enough to capture the subtle resonance changes in this circuit, then the mechanical robustness of the circuit (no open ground ports) supports this design as a useful, output-enabled fluidic circuit. However, as shown in the next section, this topology lost out to the series ammeter design.

Series Resonance Ammeter

The following is the fluidic circuit design for the best-performing fabricated series resonance ammeter:

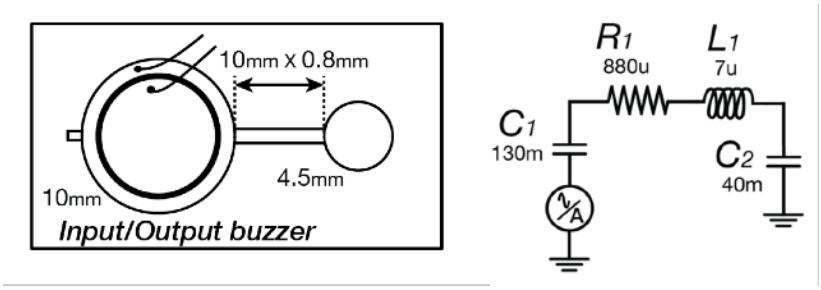

Figure 4.9. Series resonance ammeter design. Fluidic (left) and electric (right). Duplexing is used on a single piezo buzzer, hence the composite input/output.

One might notice a peculiarity about this circuit: there is no secondary piezo buzzer serving as a system output. This is the case, because there is no possible two-buzzer series ammeter fluidic circuit topology that can be made using our acrylic-cutting fabrication techniques. Therefore, the only way to use piezo buzzers as an output for this circuit is piezo duplexing. Duplexing allows the single piezo buzzer in this fluidic circuit to behave as both an input and an output. This was implemented using dynamic-impedance driving electronics that are described in chapter 5.5, which allow rapid switching between driving the piezo buzzer pressure output, and reading the electromotive output.

After implementing the duplexing electronics, the resonant frequency of the fluidic circuit can clearly be determined by electronically capturing the step response of the system. However, only one-half of the square wave period will contain ringing information, as one half of the square wave is dedicated to charging the buzzer (actuation), and the other half is dedicated to discharging the buzzer and measuring the result (measuring). This means that the refresh rate of the real-time resonant frequency tracking of the system will be half of any other topology for a given frequency of input square wave. The halving of the refresh rate is not a practical issue, because the rate of actuation can easily be increased to capture resonant frequency modulations in excess of the clotting time constants of any biosamples used with the device.

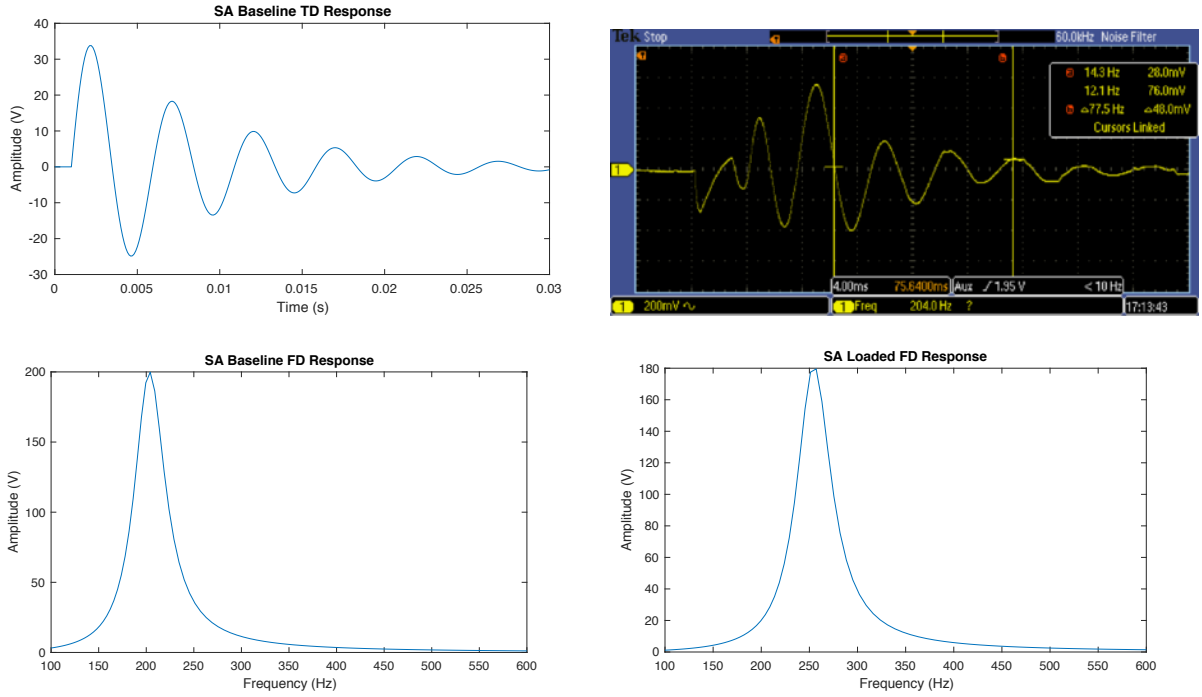

Figure 4.10. Series resonance ammeter performance. Modeled step response (upper left); real step response (upper right); modeled step response frequency domain (lower left); modeled step response frequency domain with modulation (lower right).

The pictured results above show both excellent-appearing time domain signals, as well as a single, clear frequency peak that can easily be tracked as the resonant frequency is modulated. Whereas other circuit topologies had parasitic resonances that could end up dominating the circuit response, the frequency domain of this one is pristine; it shows just one frequency peak that corresponds to the resonant frequency of the system. The time domain snapshots of the system output also appear crisp enough to demonstrate strong resonance.

There are several imperfections in the TD oscilloscope screenshots that are indicative of lower TD signal quality than the other fluidic circuit topologies. In particular, the unwanted signal components that can be seen include duplexing artifacts, mains hum, and filter-induced phase activity. This is attributable to the deprecated analog front end that was created at the time of this experiment to make these measurements as a proof-of-concept. Since then, the electrical instrumentation was remade from scratch using superior design techniques, which are

documented in the instrumentation chapters of this work. Nonetheless, the series ammeter is the clear winner of the fluidic circuit instrumentation topologies.

4.4 Step Response for a Transconductance Lowpass RLC

The transfer function of a common electric circuit is usually a ratio of two voltages, two currents, or two resistances. However, fluidic circuits transduced by a piezoelectric buzzer tend to work as voltage-in, current-out (transconductance) systems, based on the theoretical and empirical arguments in the prior section that characterize piezoelectric buzzers as force-actuating, yet flow-measuring. Therefore, the transfer function will be derived from the admittance of the circuit, equivalent to the inverse of impedance.

$$Z = R + sL + \frac{1}{sC} = \frac{1}{s}\left(s^2L + sR + \frac{1}{C}\right) \tag{4.6}$$

$$H(s) = \frac{Y}{X} = \frac{I}{V} = Z^{-1} = \frac{s}{s^2L + sR + \frac{1}{C}} = \frac{1}{L} \times \frac{s}{s^2 + \frac{R}{L}s + \frac{1}{LC}} \tag{4.7}$$

$$H(j\omega) = \frac{1}{L} \times \frac{j\omega}{-\omega^2 + \frac{R}{L}j\omega + \frac{1}{LC}} \tag{4.8}$$

$$|H(j\omega)| = \frac{1}{L} \times \frac{\omega}{\sqrt{(\frac{1}{LC} - \omega^2)^2 + (\frac{R}{L}\omega)^2}} \tag{4.9}$$

$$|H(j\omega)|_{j\omega=\frac{1}{\sqrt{LC}}} = \frac{1}{L} \times \frac{\frac{1}{\sqrt{LC}}}{\sqrt{(\frac{R}{L}\frac{1}{\sqrt{LC}})^2}} = \frac{1}{L} \times \frac{\frac{1}{\sqrt{LC}}}{\frac{R}{L}\frac{1}{\sqrt{LC}}} = \frac{1}{R} \tag{4.10}$$

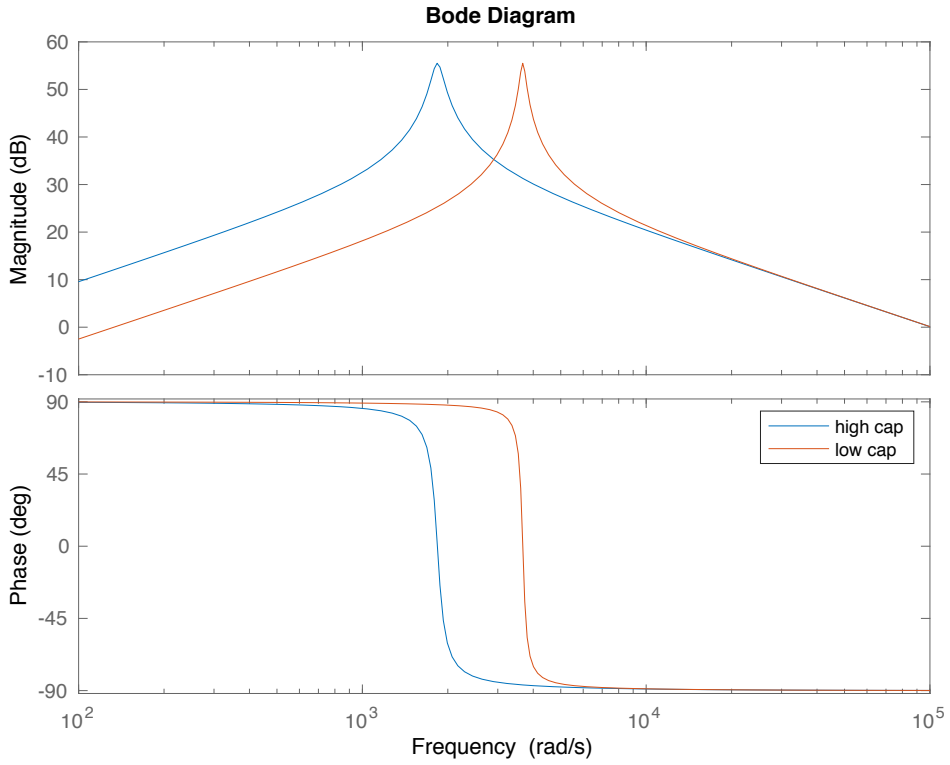

Figure 4.11. Two Bode plots of example transconductance transfer functions with different capacitances.

Despite the magnitude of the frequency response being constant for any resonant frequency, the high-frequency roll-off of the step function results in diminishing step response amplitude with resonant frequency.

$$Y(s) = H(s) \times X(s) = \frac{s}{L\left(s^2 + \frac{R}{L}s + \frac{1}{LC}\right)} \times \frac{1}{s} = \frac{1}{L\left(s^2 + \frac{R}{L}s + \frac{1}{LC}\right)} = \frac{1}{L\left(-\frac{R^2}{4L^2} + \frac{1}{LC} + \left(\frac{R}{2L} + s\right)^2\right)} \quad (4.11)$$

$$Y(s) = \frac{\sqrt{\frac{1}{LC} - \frac{R^2}{4L^2}}}{L\sqrt{\frac{1}{LC} - \frac{R^2}{4L^2}}\left(\frac{1}{LC} - \frac{R^2}{4L^2} + \left(\frac{R}{2L} + s\right)^2\right)} = \frac{\sqrt{\frac{1}{LC} - \frac{R^2}{4L^2}}}{\sqrt{\frac{L}{C} - \frac{R^2}{4}}\left(\frac{1}{LC} - \frac{R^2}{4L^2} + \left(\frac{R}{2L} + s\right)^2\right)} \quad (4.12)$$

$$y(t) = \mathscr{L}^{-1}\{Y(s)\} \frac{e^{\frac{-R}{2L}t}}{\sqrt{\frac{L}{C} - \frac{R^2}{4}}} \sin\left(\sqrt{\frac{1}{LC} - \frac{R^2}{4L^2}}t\right) = \frac{e^{\frac{-R}{2L}t}}{\sqrt{\frac{L}{C} - \frac{R^2}{4}}} \sin\left(\frac{1}{\sqrt{LC}}\left(\sqrt{1 - \frac{R^2C}{4L}}\right)t\right) \quad (4.13)$$

$$\text{Since } \omega_0 = \frac{1}{\sqrt{LC}}, \text{ and } \zeta = \frac{R}{2}\sqrt{\frac{C}{L}},$$

$$y(t) = \frac{e^{\frac{-R}{2L}t}}{\sqrt{\frac{L}{C}}\sqrt{1-\zeta^2}} \sin\left(\omega_0\sqrt{1-\zeta^2}t\right) \quad (4.14)$$

One can note that the true frequency of oscillation is not the resonant frequency, but the damped natural frequency. It is less than the undamped natural frequency by a factor of $\sqrt{1-\zeta^2}$, but the difference is practically negligible. Therefore, we can simplify the output results as the following by removing the $\sqrt{1-\zeta^2}$ factor:

$$y(t) = \sqrt{\frac{C}{L}} e^{\frac{-R}{2L}t} \sin\left(\frac{1}{\sqrt{LC}}t\right) \quad (4.15)$$

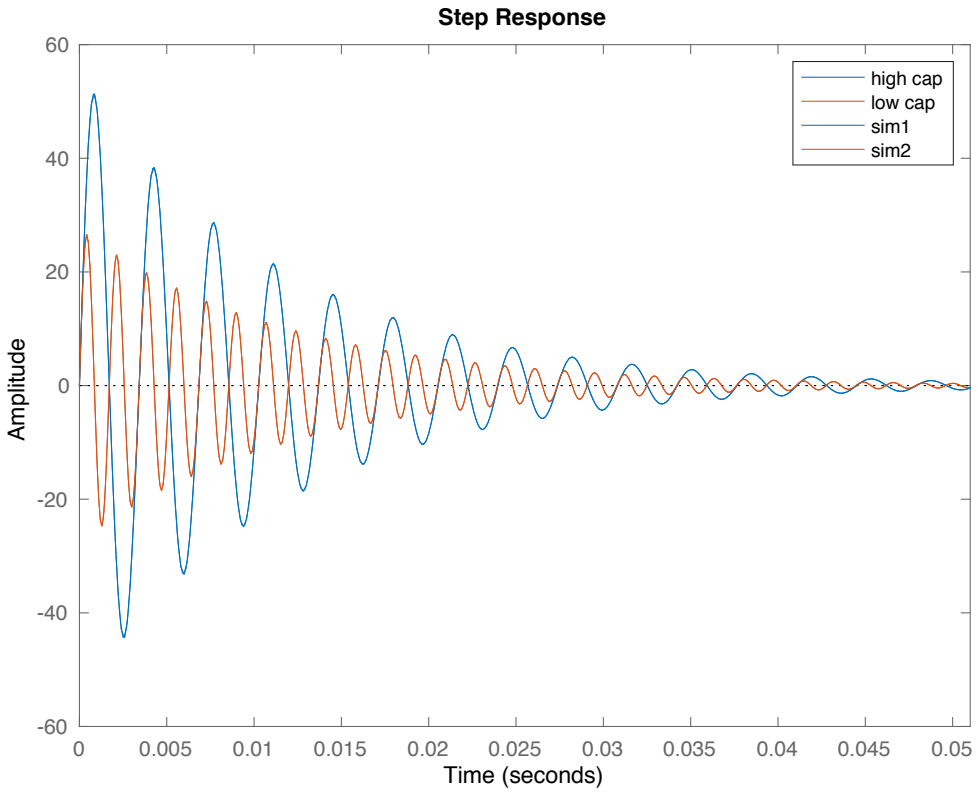

Figure 4.12. Example of reduced step response amplitude for higher resonant frequency in a transconductance system.

Changing the capacitance of the system not only affects the resonant frequency (approximating the damped natural frequency), but it also affects the amplitude of the step response.

$$\text{Poles: } s = \frac{-\frac{R}{L} \pm \sqrt{\frac{R}{L}^2 - 4\frac{1}{LC}}}{2\frac{R}{L}} \tag{4.16}$$

$$\frac{\partial s}{\partial C} = \frac{\pm 1}{C^2 R\sqrt{\frac{R^2}{L^2} - \frac{4}{LC}}} \tag{4.17}$$

It can be seen from the transfer function that as capacitance decreases, the location of the poles will change to be further from both the σ and jω axes, increasing the resonant frequency, and reducing the amplitude of the step response.

4.5 The Optimal Clot Capacitor

As discussed in chapter 2, section 3, obtaining an accurate, quantitative value for the elastic modulus of a clot sample is not necessary, nor possible, in current VE testers. The output amplitude of VE testers contain contributions from both viscous and elastic components, and the devices are unable to separate the relative contribution of the two. AC fluidics, with the goal of creating a point-of-care VE test, also does not need to perform this viscous/elastic separation, so long as the output amplitude can scale with the elastic modulus of the clot sample.

As also put in chapter 2, the viscoelasticity of a blood clot is not necessarily a simple, objective metric to measure. Existing whole blood VE testers claim most commonly that shear modulus is the measured mechanical property of their samples. However, provided there is a constant Poisson's ratio in the clot sample, the shear and elastic moduli of a material are directly related through:

$$\nu = \frac{E}{2G} - 1 \tag{4.18}$$

The assumption that the Poisson's ratio of a blood clot is constant throughout the coagulation process has been empirically justified for low strain conditions [32, 33]. Since the Poisson's ratio of a blood clot is close to that of water ($\nu = 0.5$), the elastic modulus can be linearly scaled to the Poisson's ratio by the following factor:

$$G = \frac{E}{2(\nu + 1)} \Rightarrow \frac{E}{3} \tag{4.19}$$

With this information in hand, the fluidic circuit can serve as a VE tester as long as its output amplitude (resonant frequency) is influenced by the elastic modulus of a clot sample. COMSOL simulations was used to confirm the sensitivity of a fluidic circuit capacitor to a series elastic plug emulating a clot. Aside from confirming VE sensitivity, the simulations allowed us to discover the best fluidic circuit fabrication for measuring clots. And by knowing beforehand the viscoelastic properties desired to be measured (100 Pa to 100 kPa elastic modulus range), the optimization process is specification-oriented.

Below is the generic design of a series-resonance ammeter fluidic circuit that has been modified to include a "chamber" into which clot samples may be injected. It is hypothesized that a clot in this area, or any elastic material, will behave as a series capacitance with the membrane capacitor, resulting in a guaranteed decrease in net fluidic system capacitance. The only question is: by how much does the net capacitance decrease for a given sample elasticity?

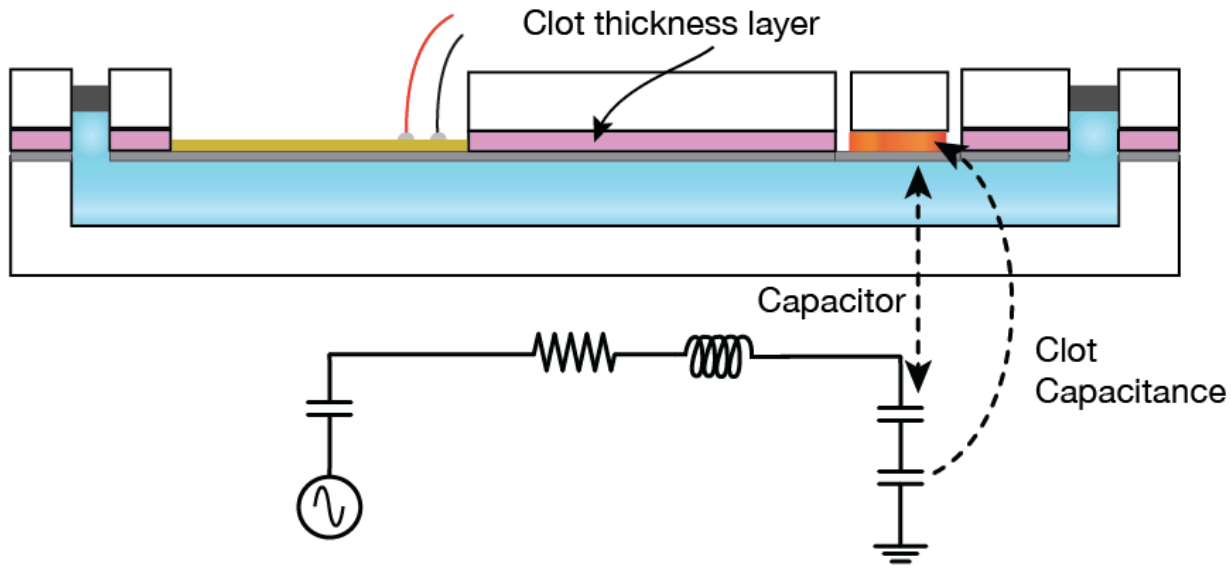

Figure 4.13. Fluidic circuit fabrication with room for clot sample to behave as an additional capacitance. There are no known biocompatibility issues expected with PPMA and Mylar for the clot capacitor chamber.

The first COMSOL simulation studied the affect of varying capacitor membrane thickness of the response of the system. The response of the system is modeled as changes in capacitor volume

for a constantly applied pressure, and independently varying elastic moduli of the clot element. Since pressure is constant, the dependent volume changes can be interpreted as capacitance changes. Therefore, the sensitivity of the capacitor to different clot elasticities should be evident.

The geometry of the model comprises a capacitor membrane, clot, and rectangular ceiling layer. The radius of the clot is kept at 4.5 mm, as is the clot. Clot thickness is kept at 0.254 mm, while membrane thickness is discretely swept in order to observe the causal variations in the elasticity response curves. The material of the ceiling layer and membrane is PMMA, and the clot material is defined as a linear elastic material with a Poisson's ratio of 0.5 and an elastic modulus that is swept during the simulation. A constant pressure of 1 kPa is applied to the bottom of the membrane in order to induce deformation, and fixed boundary conditions are applied to the sides of the membrane and the ceiling. Using 1 kPa allows the deformation to be unitarily converted to capacitance in the $\frac{mm^3}{kPa}$ unit which is standard in this work.

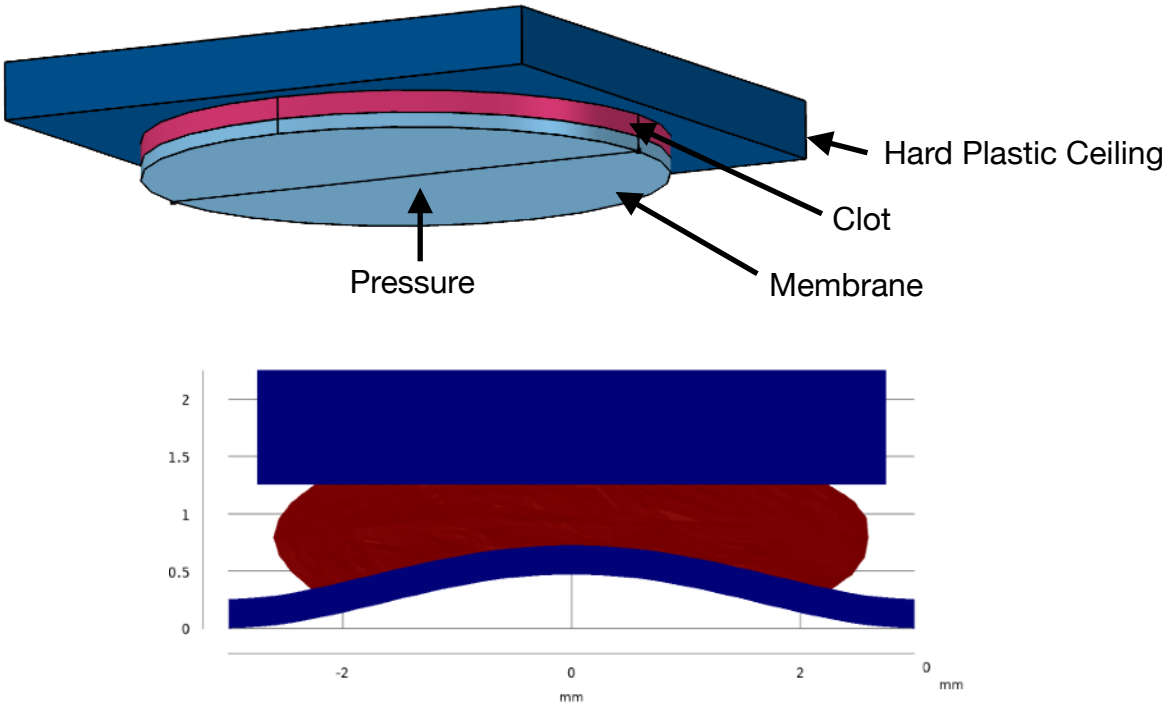

Figure 4.14. Geometry of COMSOL capacitor+clot simulation. Top shows a three-dimensional depiction, and bottom shows a cross-section with exaggerated deformation.

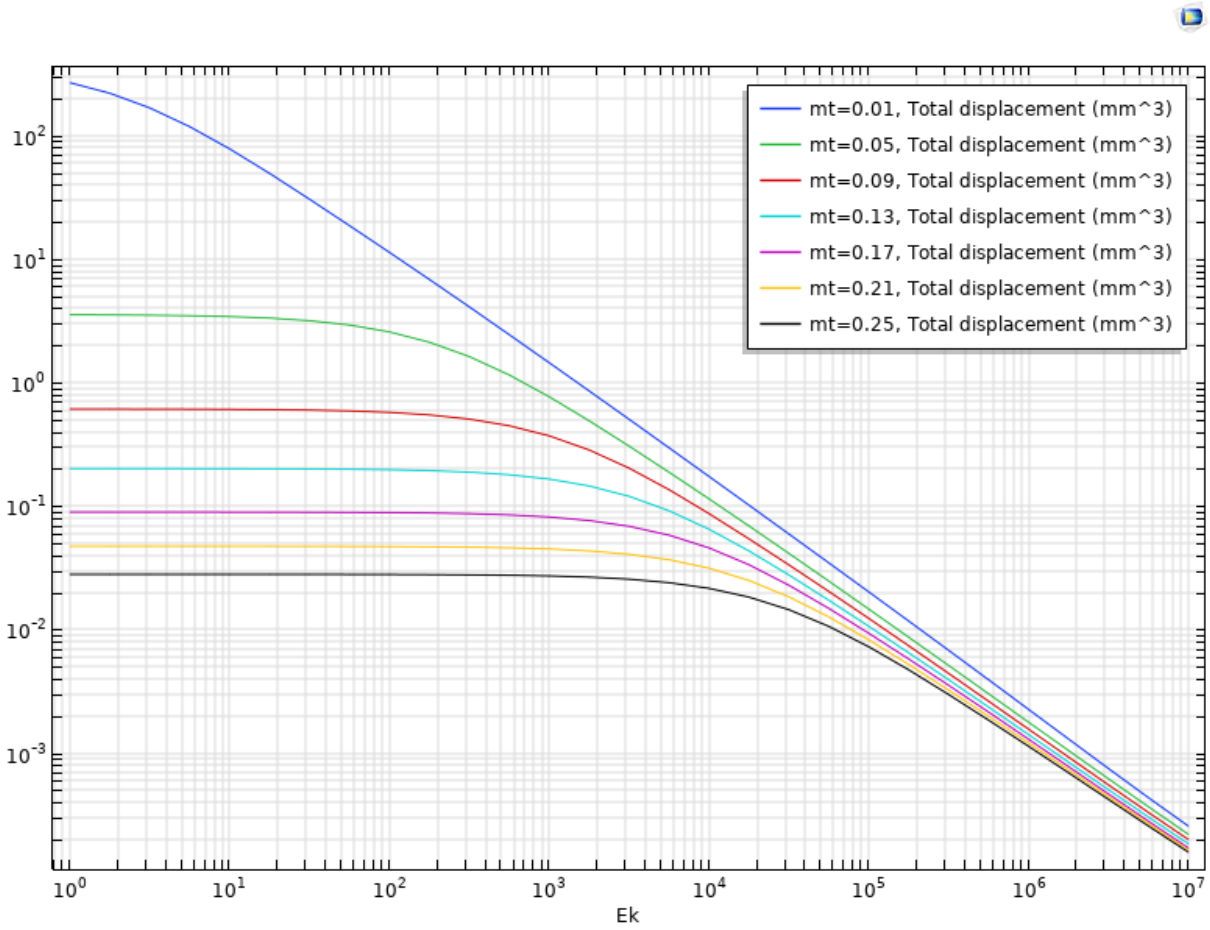

Figure 4.15. Capacitance values produced by varying clot elasticity. Response is shown for multiple membrane thickness settings to produce the various curves.

Each curve has a distinctive flat and sloped region, corresponding respectively to capacitance saturation, and near-direct linear measurement. The results of the first simulation show that thinner capacitor membranes are desirable for the measurement of a clot sample, as it increases the low-end range of elastic moduli that still induce capacitance changes. Thicker membranes saturate in their capacitance at higher elastic moduli, reducing the sensitivity of the fluidic circuit to measure the early stages of clotting, when the elastic modulus of the clot is low. There are practical mechanical limitations on the thinness of the capacitor membrane, as 2 mils with the thinnest the mylar membrane that could be made without wrinkling, creasing, and other defects occurring during device fabrication. This membrane happens to come close to the 100 Pa low end of the desired elasticity measuring range. The 100 Pa elastic modulus is not in the linear

region of sensitivity, but just outside of it. Clot thickness is adjusted later in this section to bring the 100 Pa level closer to linearity with the rest of the system's measurement range.

The results also support the hypothesis that the blood clot behaves as a series capacitance to the membrane capacitor. First of all, we know from chapter 3 that the membrane capacitor is linear. When looking at the composite capacitor (membrane & clot), we still see linearity where clot capacitance dominates. Therefore, the capacitive behavior of the clot must be linear as well. If we call the membrane capacitance the baseline capacitance C_b and the series clot capacitance C_s, then the net capacitance is given by:

$$C_{net} = \frac{1}{\frac{1}{C_b} + \frac{1}{C_s}} \tag{4.20}$$

Two capacitors in series behave like to resistors in parallel. If the capacitance value of one becomes significantly smaller than the other, it dominates by reducing the net capacitance down to a level that is close to its own capacitance. In each curve, a corner is visible. If the series capacitor theory is correct, then the corners are the points at which the dominant capacitor is swapped. In this case, at higher elastic moduli than the corner, C_s dominates, and and lower elastic moduli, C_b does. To confirm this perspective, a simulation was done using MATLAB to plot the effect that varying series capacitances has on a net capacitance on a log scale. If the curves are configured to match the plotting methods of the simulation (thickness vs. capacitance, elastic modulus vs. capacitance), then the series capacitance numerical analysis should match the physics simulation. In order to produce C_s values, an analytical clot capacitance model from prior work on fluidic circuits was used [27].

$$C = \frac{2\pi r^2 t \nu}{E} \tag{4.21}$$

This model agrees with the inverse-proportionality between clot elastic modulus and capacitance that was empirically observed in the simulation. However, it is known to be inaccurate at finding

the exact capacitance values due to errors in the way the expression treats radius, thickness, and Poisson's ratio. This will be shown in the final section of this chapter. For the analytical series capacitance model, all physical parameters of the clot are kept the same except elastic modulus, meaning that the other physical parameters simply form an inaccurate constant above a first-order variable in the denominator. Therefore, this inaccuracy will manifest as a horizontal shift in the corners of each curve by similar amounts.

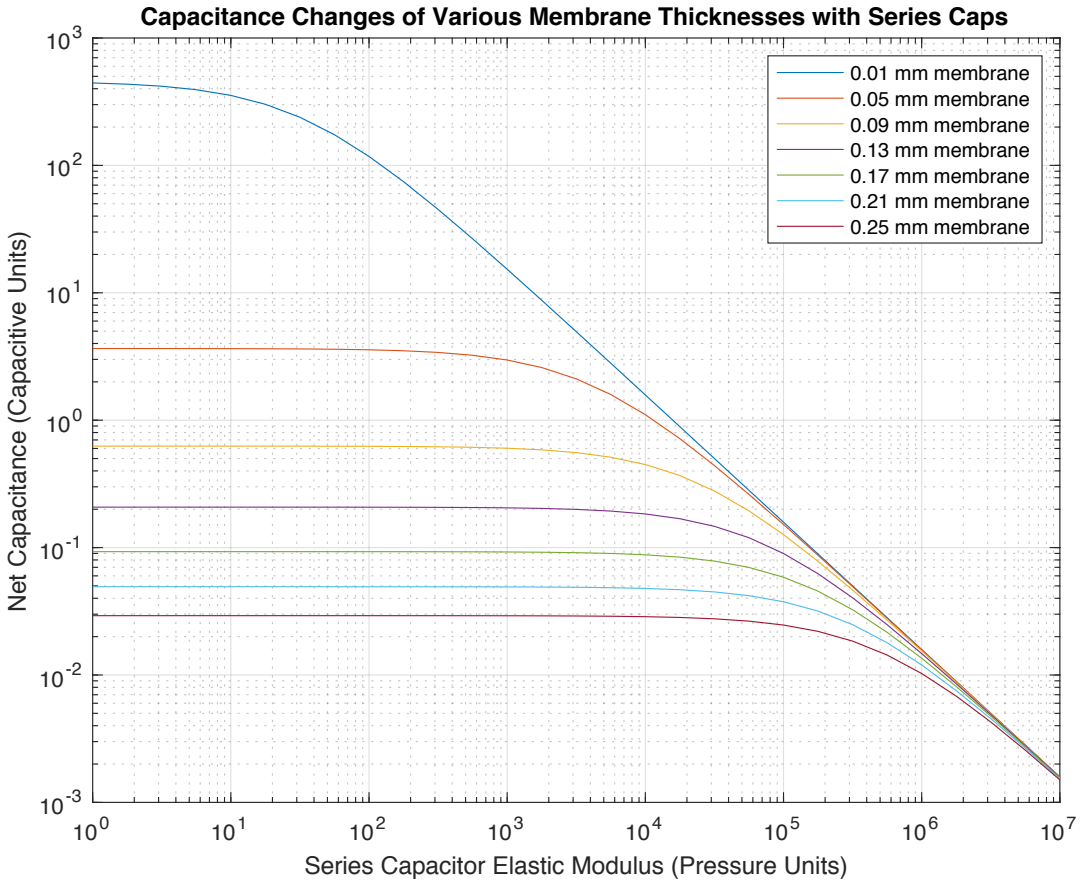

Figure 4.16. Results of analytical modeling of capacitance simulations. The corners are shifted to the right due to clot capacitance inaccuracy.

The above plot shows the net capacitance of the series C_b and C_s capacitors, with capacitances values for C_b analytically derived from the membrane capacitance expression, and C_s continuously varying according the the clot capacitance model. The baseline capacitor membrane

thicknesses are identical to the COMSOL simulation in order to produce the same set of curves. What is first apparent is the accuracy of the flat C_b-dominated regions compared to the simulation, further demonstrating the accuracy of the membrane capacitance expression. However, the corners for each curve occur at elastic modulus values approximately one order of magnitude higher than the simulation. For the sake of an easier comparison, the constant produced by the clot capacitance expression from the static parameters can be divided by an order of magnitude (an arbitrary value, thereby conceding error in the clot capacitance model) to better align the analytical and simulated curves.

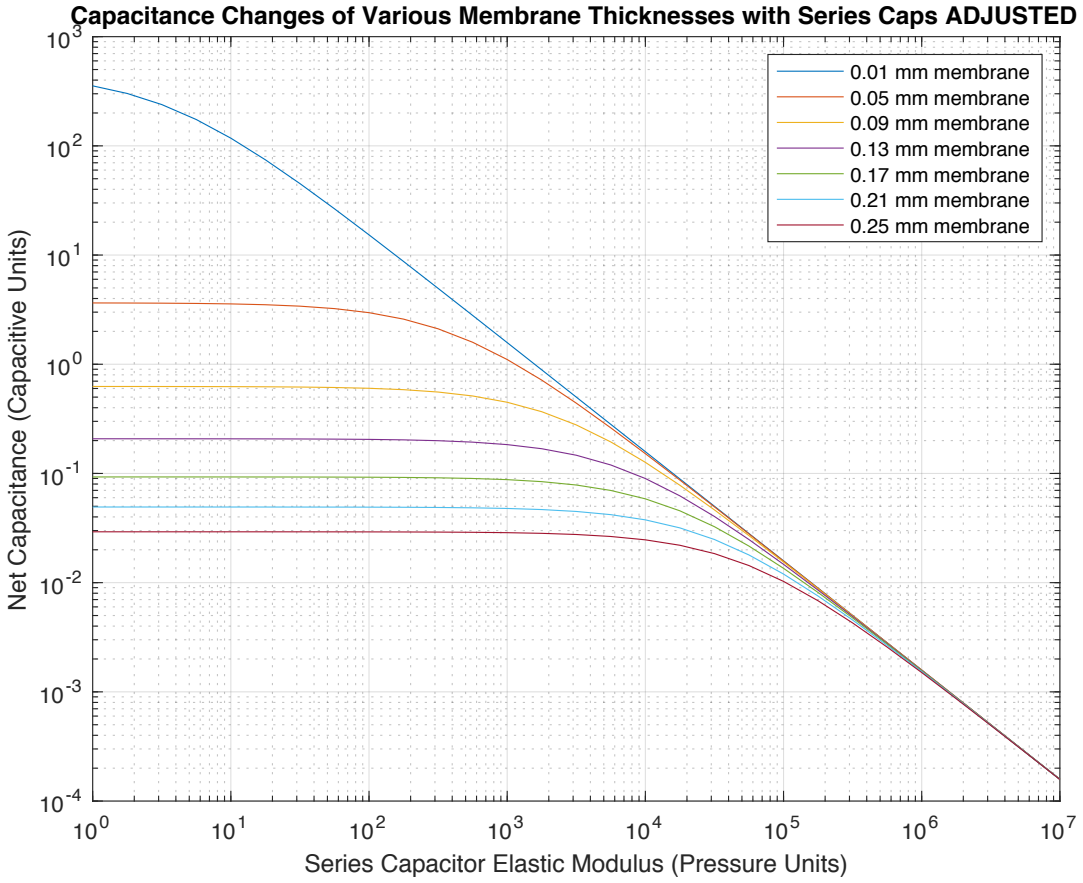

Figure 4.17. Analytical capacitance model with clot capacitance reduced by a factor of ten for the sake of easier comparison to the simulation. The curve shapes and values closely resemble the simulation.

Through inspection, the adjusted curves above look nearly identical in shape to the simulation results for both C_b plateau levels and corner elasticies. Although the curves have been manipulated by a heuristic factor to "correct" the inaccurate clot capacitance model, the congruence of the capacitance simulation and the series capacitance modeling is compelling. An accurate analytical model for describing the capacitance of a clot would produce the same curves. Regardless of the error in the clot capacitance calculation, the key, convincing takeaways are the similar shapes of the curves, the exactness of the C_b values, and the accurate relative locations of the corners.

Another simulation was run with clot thickness as the compared variable, instead of membrane thickness. Otherwise, this simulation setup was identical to the earlier one. Clot thickness also has a bearing on the system sensitivity, although not as pronounced as membrane thickness. Through inspection of the curves, the changes appear to also manifest as C_s capacitance changes. Thus, the clot thickness was made as small as possible in order to squeeze out extra low-end elastic moduli sensitivity. The thickness is 10 mils, and is made possible by using a thin PMMA sheet as the wall of the capacitor cavity.

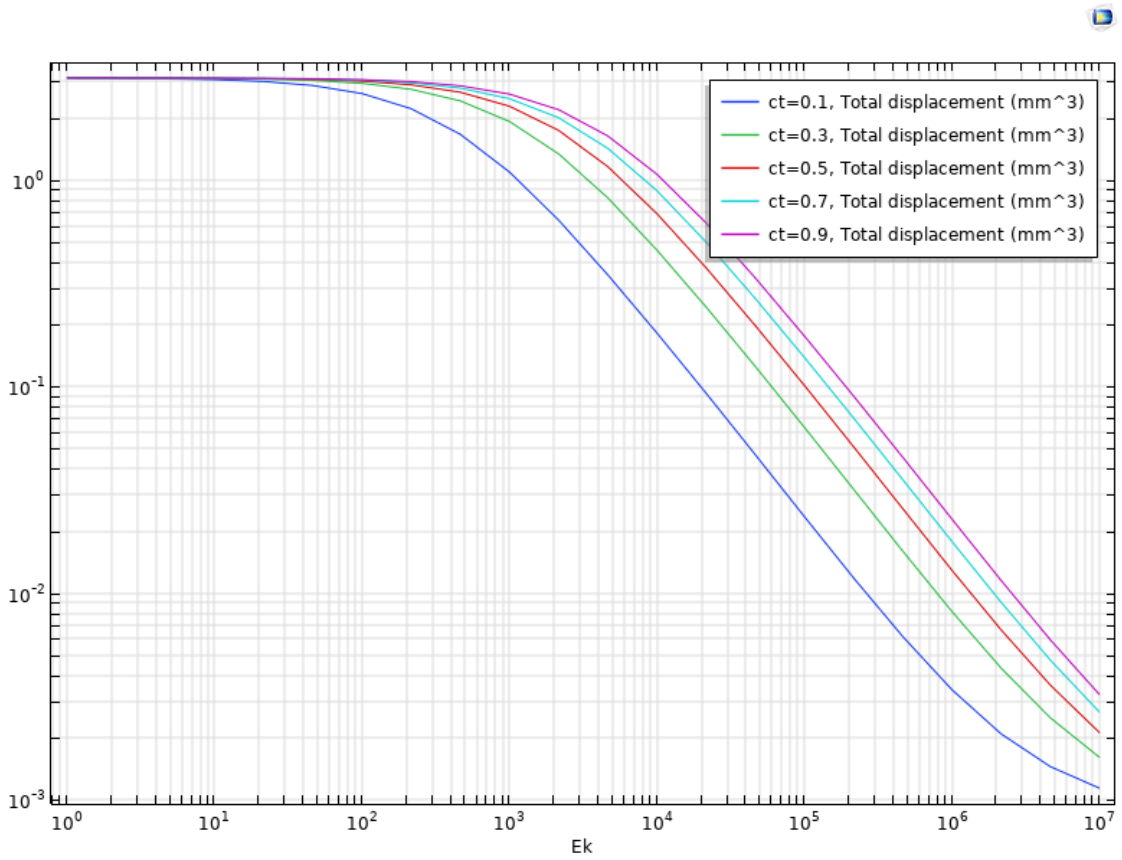

Figure 4.18. Capacitance response to clots of different thicknesses. Larger thicknesses appear to produce smaller capacitances that shift the corner left, increasing the range of elasticity measurement to lower modulus values.

The inlets where blood can be injected were designed to be very large, reducing parasitic resistance and inductance that may occur while the blood sample is still in its liquid phase.

Since the membrane and clot radii are necessarily equivalent, a larger capacitor radius of 4.5 mm was chosen in order to increase the sample size with its thin 2 mil thickness, lower the resonant frequency in order to increase overall resonant signal amplitude, and practically allow for easier sample injection.

4.6 Linearizing and Normalizing the System

There are two ways to improve the linearity and normality of the fluidic circuit. First, the amplitude of the step response over frequency, and second, the frequency of the circuit with respect to its baseline.

As we can see in section 4.4, increasing the resonant frequency through a decrease in capacitance also decreases the step response amplitude in a transconductance system. Recalling the resonant frequency and step response equations:

$$y(t) = \sqrt{\frac{C}{L}} e^{\frac{-R}{2L}t} \sin\left(\frac{1}{\sqrt{LC}}t\right) \tag{4.22}$$

$$\omega_0 = \sqrt{\frac{1}{LC}} \tag{4.23}$$

If resonant frequency is inversely proportional to the square root of capacitance, yet amplitude is directly proportional to the square root of capacitance, then it proves a first-order -20 dB per decade roll-off in amplitude over frequency (amplitude is inversely proportional to frequency). This frequency response characteristic can be written as: $H(j\omega) = \frac{A}{j\omega}$, where A is a complex proportionality constant. In order to remove the $\frac{1}{\omega}$ frequency dependence of the amplitude of the response, the frequency response effectively needs to be multiplied by ω. In the time domain, this corresponds to differentiation of the signal. The implementation of the differentiator is explained in the later instrumentation sections of this work.

Second, we come to linearizing the frequency shifting behavior of the system. Through inspection of the simulations, the change in capacitance that occurs due to the gel elasticity is linear throughout a certain range. In this range, the capacitance and elastic modulus of the sample are inversely proportional to each other. While this physical linearity is immensely useful, the only nonlinearity that occurs is the translation of capacitive changes to resonant

frequency changes. Since resonant frequency is inversely proportional to the square root of capacitance, the resonant frequency is proportional to the square root of the sample elasticity; elasticity is proportional to the square of the resonant frequency. Therefore, we can linearize the elasticity change measurements by squaring the shifts in resonant frequency that occur. However, it would be ill-advised to do this in comparison to another device whose signal processing algorithms are unknown, such as the ROTEM Delta used in experiments in chapter 7.

4.7 Obtaining an Elasticity Value

As discussed in chapter 2, obtaining an accurate, quantitative value for the elastic modulus of a clot sample is not necessary, nor possible, in current VE testers. The output amplitude of VE testers contain contributions from both viscous and elastic components, and the devices are unable to separate the relative contribution of the two. AC fluidics, with the goal of creating a point-of-care VE test, also does not need to perform this viscous/elastic separation, so long as the output amplitude can scale with the elastic modulus of the clot sample.

Nonetheless, if the contribution of viscous effects to the system are ignored, then values for the elastic modulus of the clot can still be theoretical derived. If the resonant frequency and inductance of a fluidic circuit are known, then the capacitance can be calculated. Once the capacitance in known, it can be related to an elastic modulus value by inspecting the simulation curves. In order to prove this concept, silicone rubber disks were used a test samples in experimental fluidic circuits. Since silicone has no theoretical viscous activity, the ability of the system to measure elasticity can be precisely evaluated through these experiments. A single size of silicone disk was measured across devices with different capacitor diameters in order to establish the efficacy of the general measurement principle. Different inductance values were set for each circuit to further investigate this general principle. Based on the theory and simulations that demonstrate that fluidic systems behave like linear circuits, we can expect the derived elasticity of the silicone disk (and by extension, a clot sample) to be the same for each fluidic system, regardless of its baseline capacitance. Note that this expectation is only valid for experimental samples that fall within the measurable elasticity range for each device, which is

why the device used in real, biomedical experiments has a high-capacitance capacitor, unlike the upcoming silicone experiments. Since the elastic modulus of the silicone rubber is expected to be at least 1 MPa, we can use 0.254 mm thick capacitor membranes with radii of 3 mm and up.

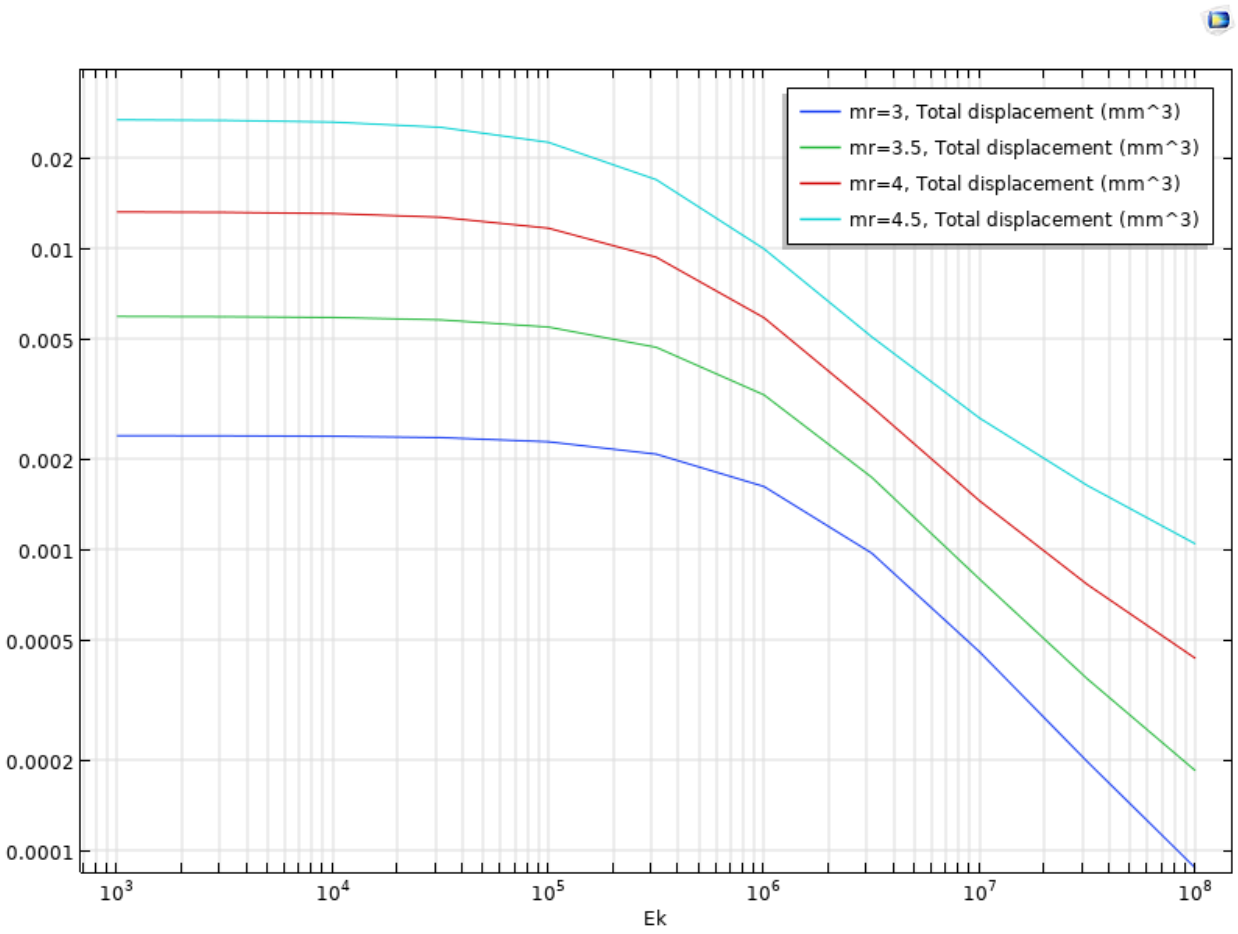

Figure 4.19. Capacitance values versus elastic modulus for a clot object with the same dimensions as the silicone disks used in this experiment. Different membrane radii were plotted in order to allow direct capacitance-to-elasticity lookup for each experimental device.

Capacitor Radius (mm)	Inductance (kg/mm^4)	Resonant Frequency (Hz)	Measured Cap (kPa/mm^3)	Simulated Cap (kPa/mm^3)	Derived Ek (MPa)	Clot Cap Model (MPa)
3	4.1E-05	712.7	0.00121	0.00137	1.58	12.92891
3.5	2.3E-05	676.8	0.00244	0.00261	1.58	6.39804
4	1.6E-05	609.8	0.00439	0.00455	1.58	3.54656

Capacitor Radius (mm)	Inductance (kg/mm^4)	Resonant Frequency (Hz)	Measured Cap (kPa/ mm^3)	Simulated Cap (kPa/ mm^3)	Derived Ek (MPa)	Clot Cap Model (MPa)
4.5	1.1E-05	530.0	0.00791	0.00763	1.58	1.97041

Table 4. Experimental results of elastic modulus measuring experiments using silicone disks. Despite the rounding towards a discrete elastic modulus value due to simulation time, the results are very promising. The error of the analytical clot capacitance model is also apparent.

The above results convincingly illustrate the ability of fluidic circuits to be used in a limited manner as an elastometer. The derived elastic modulus values were found by taking the experimentally-sourced capacitance values for each fluidic circuit and finding the closest simulated capacitance value, corresponding to an elastic modulus (the independent variable of the simulation). Since simulations like this a computationally expensive, only a limited number of elastic moduli can be evaluated. The range was chosen to be three orders of magnitude: from 10^5 to 10^8 Pascals. Five logarithmic values of elastic modulus were chosen for each order of magnitude, producing fifteen total elastic moduli values per circuit radius. In this experiment, the derived elastic modulus of the silicone disk in each circuit ended up being the same value of 1.58 MPa, with the two closest other values being 1 MPa and 2.51 MPa. Although this discretization of the elastic moduli adds some error to this experiment, the efficacy of fluidic circuits at measuring elasticity is still supported by the fact that each fluidic circuit landed on the same MPa measurement, and the low error between the experimental and simulated capacitances. The elastic modulus results of the analytical clot capacitance model from prior work ([27]) are shown on the far-right side of the table for comparison to the simulation-gathered results. Large variations in the elastic modulus values produced by the model between fluidic circuits discredit its accuracy.

Despite the promising notion that fluidic circuits can precisely measure the elastic moduli of a small material object, one must be reminded that this is not strictly possible with viscoelastic materials, because the viscosity contributes the the overall mechanical impedance of the sample,

as previously stated. However, the clear effect that elasticity has on this system is sufficient to explore its application as a blood VE tester.

Chapter 5: Instrumentation Engineering- Part 1: Analog

5.1 Preface

The next two chapters will document in technical detail the design of the electrical instrumentation used with AC fluidic cartridges. The instrumentation must be portable and efficient in order to demonstrate the potential viability of AC fluidics as a point-of-care testing technology. In chapter 3.7, prior instrumentation methods were shown that were sufficient enough to enable laboratory evaluation in prior work, but are still far from being portable, efficient, and inexpensive enough to meet point-of-care requirements [26, 27]. Finally, as brought up in the chapter 4, it was shown that AC fluidic circuits could be designed to produce a large, ringing step response that could be electrically measured through the reversible transduction of the same piezoelectric unimorph element that is also used as a pressure source. This principle forms the foundation of the instrumentation approach in this work.

Throughout the years of work that have been dedicated to this project, multiple iterations of instrumentation systems were produced. Instead of verbosely documenting each iteration and its changes, only the latest iteration will be documented, with the lessons learned being only briefly or implicitly described. To provide a brief summary of the generational changes, the main differences come down to the efficiency and performance of the analog front end, and the optimization of the digital signal processing. This entails reduced analog stage count, more efficient power management, improving the piezo driving stage to reduce noise by accepting high voltage rails from boost converters, reducing the complexity of the track-and-hold stages, using better suited op-amps for their respective applications, reducing variability in filter response, employing more powerful MCUs, use of multirate signal processing, and even more changes unlisted. The description of the design rationale of the latest iteration is influenced by many of these changes.

5.2 System Requirements

Functional Requirements

The system will consist of fluid-containing cartridges that connect to an electrical unit. The purpose of the electrical unit is to:

- Supply power for digital, analog, and piezo components.
- Power the fluidic circuits by driving the piezoelectric element therein.
  - The piezoelectric element needs to be repeatedly charged and discharged in order to produce pressure changes in the fluidic cartridge. These changes are to be steps in pressure that come about from sudden instances of charging and discharging of a piezo buzzer. Greater charge transfer levels to the piezo are preferred in order to increase the associated fluidic pressure changes, thereby increasing the amplitude of the resonating ringing to be recorded. Faster piezo charging transition times are preferred in order to allow the resonant signal to be recorded sooner, when the amplitude of the damped resonant pressure oscillation in the fluidic cartridge is theoretically larger.
- Transduce pressure oscillations in the fluidic circuit to electrical signals and perform signal conditioning.
  - The system must be able to produce a clean depiction of the resonant ringing signals. There may be signal gating, amplification and filtering. The gating will discard any signals that are not associated with the resonance of the fluidic circuit, the amplification will ensure that the signal is high enough in amplitude for analog-to-digital conversion, and filtering will bandlimit the signal within the ranges of expected resonance values of the fluidic systems.
- Conduct frequency analysis to determine the resonant frequency of the fluidic circuit.
  - Digital frequency analysis must determine the resonant frequency composing the damped oscillation signal.
- Output a real-time stream of resonant frequency information to be displayed on a serial plotter.
  - The final objective of the digital electronics is to output a serial stream of values corresponding to the measured resonant frequency of the fluidic system. This data is meant to be used with a means of display that is outside of the scope of this prototype.

Power Requirements

The system must be able to run off of a single +5 V rail from a USB line. From this noisy USB rail, a clean, low-noise, low-voltage bipolar set of rails must be product for use in the analog front end. This can be implemented using linear LDO regulators. The final subsystem that requires a unique power setup is the piezoelectric driver. A voltage boost to the range of 20-40 V is desired, corresponding to a level about one order of magnitude higher than any other voltage in the system.

The electronics must be low-power in order to facilitate the portability of the device, but not at the expense of SNR. Due to the high expected current draw of the MCU, high quiescent current draw of amplifiers and other integrated circuits may be acceptable in some cases.

Communication and Interface Requirements

The device will provide USB serial communication, using a MCU development board to provide basic USB output sent to an external PC. The serial data can be viewed in real-time or recorded using a multitude of available software.

Control Requirements

The control of the cartridge measurement system is entirely open-loop, as the MCU will generate digital signals to trigger the cartridge measurement at a preprogrammed pace. The analog front consists of stages of signal conditioning without any global feedback. All specifications on the analog front end will remain fixed from fabrication, including frequency response and gain. The digital filtering done will not rely on any adaptive techniques that require feedback.

Computation Requirements

The system will include a powerful MCU that is tasked with producing the digital control signals, collecting data, and doing DSP. The computations consist of storing multiple digital recordings of analog signals, waveform averaging, linear filtering, performing an FFT, and conducting frequency peak analysis. The MCU used to operate this system must boast high

memory and high clock speed in order to achieve the computations. Any MCU with an ARM Cortex-M4 is likely a good contender, with 32-bitness, at least 100 MHz core clock, and 50 KB of RAM. No connection to online resources is necessary yet, as wireless communications is outside of the scope of this prototype. A DSP MCU would likely constitute a proper choice for a final product, but rapid prototyping ability dominates the needs of this project.

Software and Firmware Requirements

Programs for device control, signal digitization, resonant frequency computation, and serial communication will be preloaded to the MCU used in the device. Therefore, no software environment must be developed to interface with the device. However, since the MCU operates as a serial output, an OS is generally required to receive and store the serial data. No internet connection should be required for proper functioning.

Data Storage, Format, and Security Requirements

The A-D converter must produce 16-bit integers that correspond to the signal levels of the recorded analog signal. Although these signals are quantized as fixed-point numbers, subsequent calculations and operations on the data will be done using 64-bit floating-point numbers in the ARM environment. All working data will be stored locally on the SRAM of the MCU. The final output of the digital system, the clot firmness as determined by the resonant frequency, is a single floating-point value. The data collected will be not be considered private medical information, and will not be subject to security and encryption protocols due to HIPAA.

Precision and Accuracy Requirements

The accuracy and precision of the A-D sampling timing must be high in order to have high confidence and low variability in the calculated frequency information of the signal. High timing accuracy is necessary to ensure that a calculated resonant frequency closely corresponds to the actual resonant frequency of the connected fluidic system. The 30 ppm typical accuracy of a quartz crystal oscillator will suffice. High timing precision is important to reduce jitter that

would add noise to the frequency domain of the collected signals, rendering frequency peak analysis more difficult.

User Interface Requirements

Due to the lack of consumer-friendliness of the instrumentation at this point, a custom, easy-to-use UX is not strictly necessary for this system. All interfacing with the device will be done through MCU programming, mechanical switches, and USB serial reception. Cartridges will be electrically connected to the device through alligator clips.

Materials Requirements

The electronic components will be sourced with RoHS components to the best selection available. Additionally, RoHS exemption 7c-I excludes PZT piezoelectric transducers from the requirements, allowing this system to be labeled as RoHS. However, since PZT contains lead, this system cannot be labelled as lead-free.

Mechanical Requirements

There will be no housing made for any electronic reader unit. Jumper cables will be used to create electrical conduction between the measurement electronics and the electrically passive cartridge. The electronics will be implemented on through-hole breadboards for ease of prototyping.

5.3 System Architecture

The first step to producing instrumentation that meets the requirement of this project was to conceive of required stages and the way they are organized. This begins with the closest stage to the AC fluidic circuits: the piezo driver. Subsequent signal conditioning stages include windowing, amplifying, and filtering sections. After the analog stages, the signal is digitized, stored, and processed into a digital stream of the measured resonant frequency of the fluidic circuit under test. The following signal flow diagram depicts this high-level approach to the instrumentation.

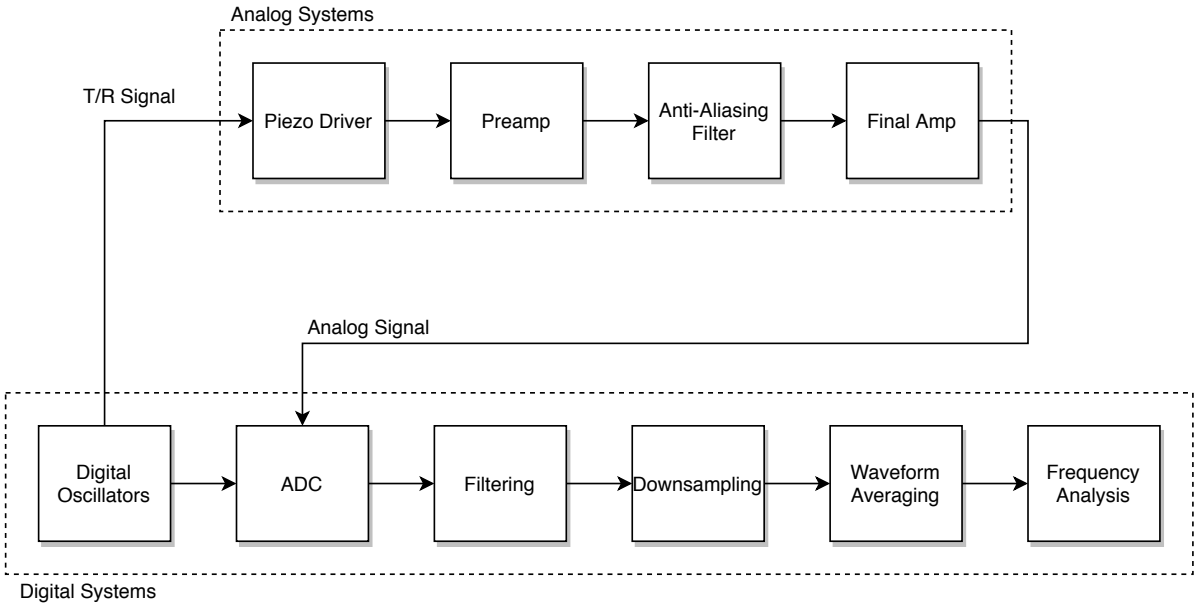

Figure 5.1. Signal flow block diagram for fluidic circuit instrumentation.

The next step was to convert the signal flow diagram into an electrically feasible design. At the center of this design is a microcontroller unit (MCU), which enables programatic control of analog instruments, analog-to-digital conversion, digital signal processing, data output streaming, and other useful features. Naturally, MCUs are present in nearly all portable instrumentation devices. The following electronic block diagram better resembles an actual electronic implementation for the instrumentation.

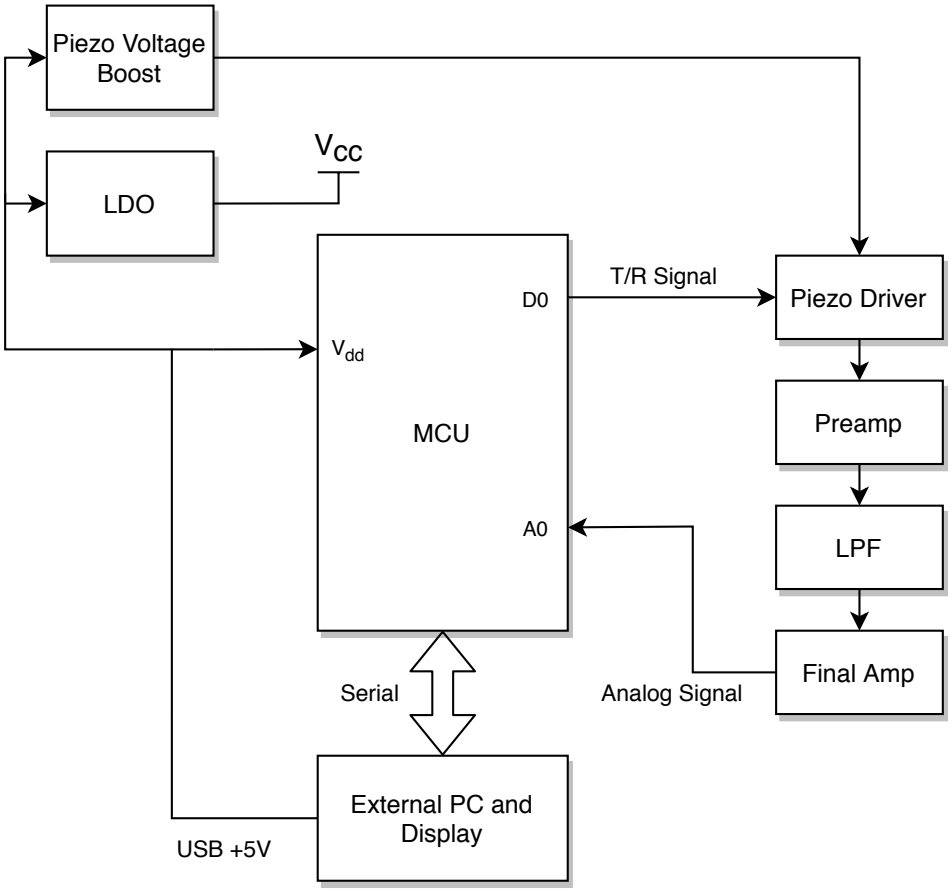

Figure 5.2. Analog electronics block diagram implementing signal flow.

The elaborated analog stages include power management and connections to the MCU, while the MCU is tasked with executing all digital systems to further process the received analog signal. The design of all analog stages will be described in the remaining sections of this chapter, with complete schematics and a bill of materials available in the appendices.

5.4 Power Supply

The requirements specify that the entire system must be able to run off of a single USB +5V input. For the vast majority of microcontrollers that could be used with this project, 5 volts is plenty enough to run the MCU. However, it would be a poor decision to run the analog subsystems on USB voltage, as it is notoriously noisy and imprecise. In order to produce high-

quality analog results, the analog subsystems must run on low-noise, low-artifact bipolar power rails. To this end, linear low dropout (LDO) regulators were utilized to create a bipolar supply. Although the LDO feature may not strictly be necessary if producing the bipolar analog supply from the USB +5V rail, the LDO feature can allow a +3.3V rail to also be used, with is commonly done on the development boards of MCUs. The would allow the line and load regulation of the LDOs we use to be combined with addition regulation from a +3.3V MCU regulator.

Designing the bipolar analog supply was rather straightforward, as it mainly came down to choice of LDO regulators. As it is beneficial to have a larger bipolar voltage range, allowing for a reasonable selection of op-amps and greater output range, the range was chosen to by 3 volts (±1.5V bipolar). The low dropout voltage of the LDO regulators allows the 3V bipolar rails to be created from the +3.3V MCU rail. The regulators were chosen to be the BAxxBC0 series due to their output voltage accuracy, integrated protective measures, and high line and load regulation specifications. For simplicity, fixed output versions were chosen at +3V and +1.5V.

Prior iterations of the circuit were designed to run off of a single-use alkaline 9V battery. Although the Teensy can run solely on USB power, the 9V battery was still required to power the piezoelectric driver of the old system.

5.5 Piezo Driving and Transduction

In general, higher voltages put across a piezo element will produce higher quality signals to be transduced. In order to increase the SNR of this critical driving stage, it was desired to drive the piezo elements with a special, higher-voltage rail produced from a piezo-specific boost converter, instead of the low-voltage bipolar rails used by the other analog stages. The MC34063A DC-DC converter was selected for its adjustable output voltage (allowing heuristic evaluation of different boost levels) and short-circuit current limiting (a prudent safety measure when working with higher voltages, especially when connecting to external modules like fluidic circuits).

However, as with any boost converter, the output voltage will contain considerable noise and artifacts, despite a clean input. These artifacts are highly undesired in the signal from the piezoelectric buzzers, as their amplitude can easy obscure the fluidic circuit ringing signal. To circumvent this problem, the topology of the piezo charger was designed to ensure that piezo buzzers discharged in a step-down fashion into ground, rather than a step-up to the boost potential. Incidentally, an earlier iteration of piezo transduction actually utilized a step-up method, because the voltage rail to which the buzzer was being stepped was low-noise. Naturally, that is not the case with a boost converter, so a change in topology was warranted. The AC component of the +28V rail can theoretically slightly alter the amplitude of the resonant frequency ringing signal, depending on the time at which the +28V rail is disconnected from the piezo buzzer. However, the AC component of the +28V rail is about 400 mV peak-to-peak, which is less then 36 dB below the +28V DC component, so any amplitude changes in the ringing signal are very small, and unlikely to cause any issues with repeated frequency analysis of a fluidic circuit.

In terms of circuit layout, the piezo buzzer must be on the low-side of a high-side switch to the boost potential. The downside to this circuit layout is the extra complexity in making a high-side switch. Low-side switches can often be implemented using N-channel MOSFETs that need only the logic-level (3.3V or 5V) actuation signal of an MCU to be switch on and off (linear and cutoff operation modes). High-side switches require a P-channel MOSFET, which typically require a gate actuation signal of much greater voltage range than MCU logic. For the P-channel MOSFET to turn off, the gate must be held at the source voltage, and for it to turn on and conduct ohmically, the gate voltage must be reduced from the source voltage by an amount specified as the gate-source threshold voltage ($V_{GS(th)}$). In practice, the change in gate voltage is often made larger in order to guarantee ohmic conduction for higher drain-source potential difference. In order to produce this high voltage signal, an NPN BJT in common emitter topology is used to convert the MCU logic signal into the P-channel gate driving signal.

When the BJT is on (in saturation mode), the gate voltage is taken down to a voltage division of the source voltage and the collector-emitter saturation voltage of the BJT (typically about several hundred millivolts, so approximation as ground is reasonable), producing a sufficient gate-source potential difference in the MOSFET to activate ohmic conduction without exceeding the maximum gate-source voltage. The values of the resistors that make up the voltage divider are chosen according to the desired voltage reduction (-10V) and the desired Thevenin resistance. If the Thevenin resistance is too low, then energy will be wasted when the BJT is on through the high current flowing through the low-resistance voltage divider. However, if the Thevenin resistance is too high, it could form a nontrivial delay in MOSFET switching due to the large RC time constant formed with the gate capacitance of the FET. By choosing a P-channel MOSFET with low input capacitance, this problem is obviated, and resistors in the 10-100 kΩ range can be used. When the BJT is off (cut-off mode), the gate is taken to the source potential via a pull-up resistor. The SUP53P06-20-E3 P-channel MOSFET was selected for its low drain-source resistance of 19.5 mΩ when it is on, reasonable input capacitance of about 3500 pF, and its robust current and temperature ratings. The 2N3904 NPN BJT was selected for its famous overall versatility. A series resistor was placed on the BJT base to avoid overcurrenting the MCU actuation signal.

After the piezoelectric buzzer had been given a robust driving mechanism, the transduction methods still needed to be implemented. There were two methods of piezoelectric transduction considered: resistor-capacitor windowing (RCW) and transimpedance amplifying (TIA). Both of these methods take advantage of the fact that piezoelectric buzzers behave electrically most like a capacitive component, as is shown in the Van Dyke model of an unloaded piezoelectric element.

The RCW method consists of discharging the piezo buzzer, behaving as a capacitor, across a resistor. The potential difference across the resistor will include the step response signal. As long as the switching mechanisms discussed earlier are assumed to be nearly ideal, then the major design decisions for this transduction method are the resistance value and piezo charging

amount. This corresponds to the discharge resistor value, and the voltage of the piezo before discharge. Since the boost converter in this system has an adjustable output level, heuristic evaluation was straightforward, and +28 V was chosen as a compromise between SNR and current consumption. Choosing the resistance value requires a deeper understanding of the drawbacks of the RCW transduction method. With the introduction of the resistance in the RC windowing method, piezo discharge actually must follow the step response of a first order LTI system, which is an exponential rise or fall. This can cause three issues:

1. The pole created can fall into the range of expected ACF resonant frequencies (0.1 - 1 kHz).
2. Resonant ringing picked up by the piezo buzzer cannot be observed before several RC time constants worth of delay.
3. The gain of the transduction stage, controlled by the resistance, exacerbates the above.

The delay caused by the RC time constant is the purpose for the “windowing” portion of RCW. The very large exponential transient from the signal must be removed from the signal in order to avoid issues with input voltages damaging op-amps, and filter transient responses being dominated by the exponential, further obscuring the desired ringing signal. The exponential can be suppressed through amplitude windowing or time windowing. Prior iterations of the instrumentation used a track-and-hold amplifier to perform time windowing, but this was abandoned due to difficulty in managing the high-dynamic range of the signal with the limited selection of analog switch and S/H amplifier options available. The current amplitude windowing system which uses a diode-based passive voltage clipper to reduce the exponential transient amplitude to a level no more than one diode drop (~0.6-0.7 V) above the ground potential of the bipolar analog supply, ensuring that the signal falls within the common-mode input range of the first amplifier stage without clipping the ringing itself.

RCW, although proven to work, has listed flaws, motivating the pursuit of an alternative transduction method. In order to obtain a sharp step response with low rise/fall time, the charge accumulated on the capacitor must discharge as fast as possible. Since the above issues boil down to the nonzero resistance coupled with the capacitive piezo buzzer, the most promising

idea was to use a transimpedance amplifier to read the piezo buzzer, as an ideal TIA has no input resistance. Although the design of the TIA is more complex than the RC windowing technique, namely due the possibility for shorting between the piezo boost rail and the zero-input-resistance TIA, it theoretically removes the need for windowing, so the overall component could is comparable to the RCW technique. Both transduction methods were implemented on a single board in order to allow direct comparison between the two.

Unfortunately, the TIA transduction method failed to produce high-quality results. The piezo buzzer, if discharged with no electrical impedance, actually allows the mechanical resonance of the buzzer itself to dominate, as opposed to the "RLC" resonance of the fluidic circuit to which it is connected. Therefore, the RCW method was chosen as the final transduction method, with 27 kΩ allowing for a compromise between fast settling time and low mechanical resonance interference.

5.6 Filtering and Amplification

With the fluidic ringing signal having been transduced effectively from the piezo buzzer, the remaining objectives of the analog front-end is to prepare the signal for digitization. This comes down to filtering and amplification. Although these two processes are very common, there are countless ways of implementing them. Achieving the best results is based on recognizing tradeoffs and making the right decision for this application. Across the board, the first tradeoff to consider is noise versus power consumption. Higher resistance values and low quiescent current op-amps would save energy, as is important for a portable, point-of-care system. This comes at the cost of increased noise, which can make it difficult or impossible to resolve the resonant frequency of the fluidic circuit being measured. To make a judgement on this matter, the current consumption of other circuit components was taken into account. MCUs and their evaluation boards can easily consume current in the 10s of milliamps, if not 100s for the computational requirements of this system. Furthermore, the power supply and piezo driver of the system draws current in the 10s of mA for the linear regulators and boost converter. The total current draw of the system so far is relatively large compared to the quiescent current of low-noise op-amps,

which is usually on the order of single milliamps per channel. Therefore, priority was given to low-noise implementation strategies.

The first low-noise implementation strategy is performing some amplification of the ringing signal before filtering occurs. Filtering larger, amplified signals wastes more energy, but it introduces less opportunity for noise (Johnson resistor noise, amplifier voltage noise, an amplifier current noise) to become a significant within the signal bandwidth. The amplifier consists of a filter preamp and a post-filter final amplifier. The most important parameters for the preamp are high PSRR, low noise, high input impedance, low input bias current, and low input offset voltage. The TLV2461 is used for its adherence to these parameters. The classic non-inverting topology is preferred in order to maximize the benefits of negative feedback, such as high input impedance and low distortion.

The design of the filter stage includes filter type, implementation details. The Butterworth filter type was selected due to a lack of other factors that would motivate the use of another filter type. For instance, since the signal is undergoing frequency analysis on the magnitude spectrum, linear phase filtering is not important, removing the Bessel filter type from consideration. The multiple feedback topology was selected due to its reduced sensitivity to component tolerances than Sallen-Key and other active filter topologies. The cutoff frequency is set to 1 kHz, which is the upper bandwidth limit for AC fluidics frequencies. RC pairs were chosen such that no resistor is greater than 100 kΩ. Finally, the order of the filter must be chosen. The pole count of the filter is five, with justification found in the first DSP section, since it is based on eliminating aliasing. Nevertheless, the parity of the pole count at this point was still chosen to be odd (3rd order, 5th, 7th, etc.). This allows a buffered, passive RC circuit to comprise the last pole of the filter, helping to reduce the lack of high-frequency attenuation that commonly occurs in second-order op-amp filter stages due to diminishing loop gain combined with positive feedback. The OP484 was chosen for the filter stage due to its very low noise and wide bandwidth, which help to reduce the above drawbacks of second-order filter stages at higher frequencies by providing

additional loop gain for the MHz-level frequencies present in the digital systems that may parasitically couple their way into the analog signal.

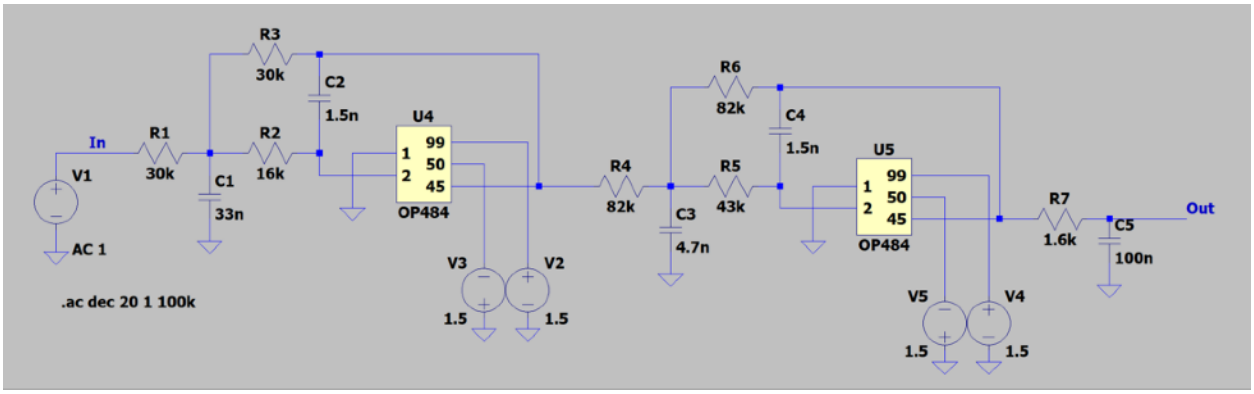

Figure 5.3. Lowpass filter model in LTspice XVII. Pre and post buffers were not included.

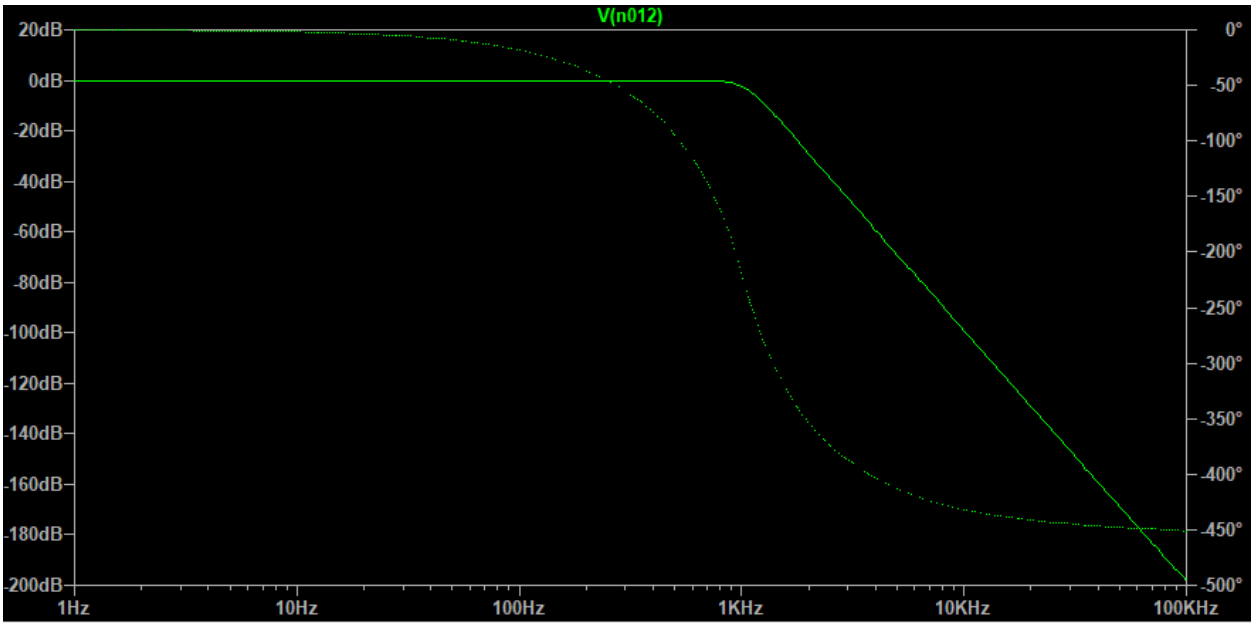

Figure 5.4. Frequency response of LTspice model showing flat passband, -100 dB/dec attenuation, and 1 kHz cutoff, validating the filter design.

Finally, there is a final amplifier than provides additional gain to the signal and serves as an ADC driver. The component used here is also a TLV246, same like the preamp. The high PSRR allows

the amplifier to send a clean signal over to the ADC without noise on the bipolar analog rails bypassing the low-pass filter. Otherwise, that noise would likely introduce aliasing.

5.7 Lack of Analog Differentiation

As uncovered in chapter 4, section 4, the step response for a transconductance system will decrease in amplitude as frequency increases. In order to normalize the frequency response of the signal, differentiation can be used to remove the frequency-dependence of ringing amplitude. This can be implemented as an analog or digital system. Ultimately, it was chosen to implement the differentiator digitally, because there are many practical drawbacks to analog differentiators. These drawbacks include high sensitivity to noise, and low stability at high frequencies, including the potential to oscillate.

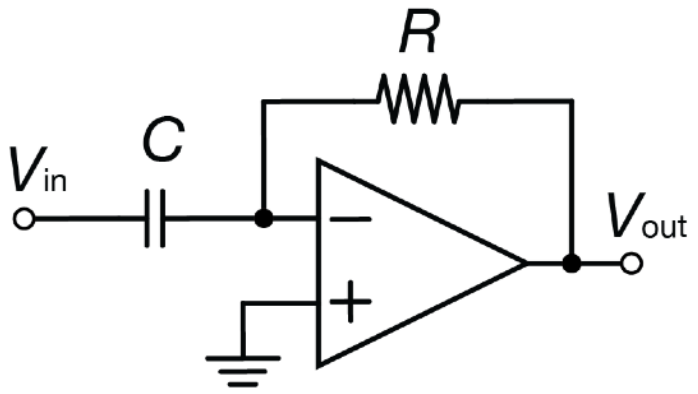

Figure 5.5. Theoretically ideal analog differentiator, with noise and stability problems.

These can be reduced through the use of an input resistor and feedback capacitor, but the circuit will still amplify undesirable high frequencies, and attempts to reduce this high-frequency amplification result in overdamping in the differentiation region.

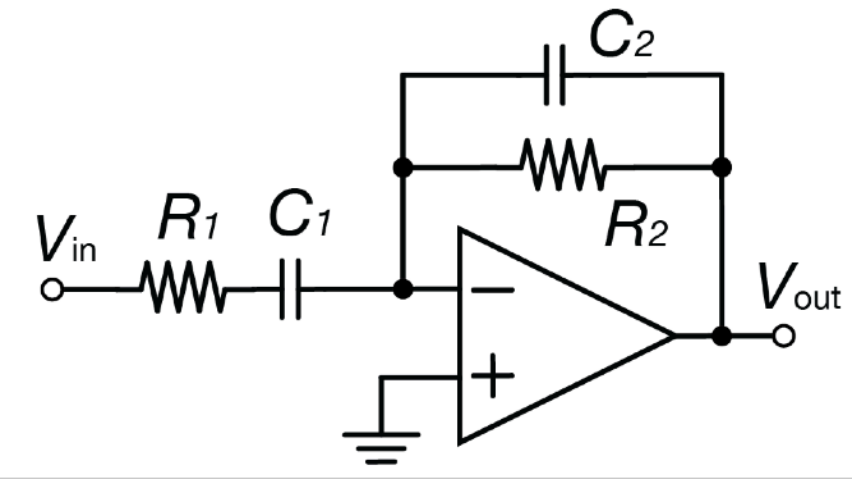

Figure 5.6. Practical analog differentiator, with high-damping side-effects.

On the other hand, DSP differentiation is closer to ideal, has no stability concerns, and after bandlimiting and downsampling, it does not increase the magnitude of high frequencies that we desire to filter out. Therefore, no analog differentiation is performed, and at this point, the signal is considered ready for A-D conversion and DSP.

Chapter 6: Instrumentation Engineering- Part 2: Digital

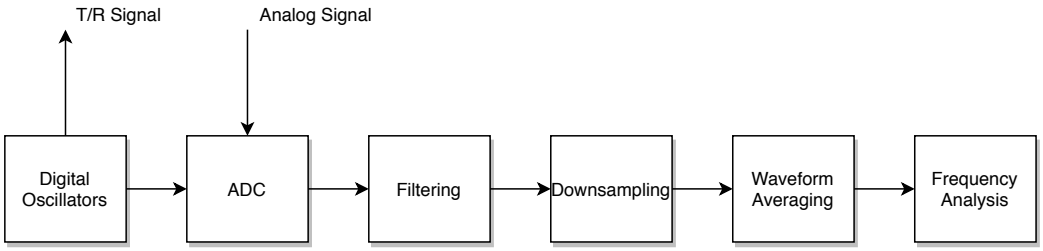

Figure 6.1. DSP block diagram adapted from last chapter.

6.1 Choice of MCU

After the analog front end produces a healthy voltage signal that displays the ringing of the system, the frequency of the ringing must be uncovered in order to determine the resonant frequency of the fluidic circuit. Naturally, this is a point where digital signal processing (DSP) comes into play, enabling sophisticated and precise analysis of the ringing signal. The first key decision to make was the DSP prototyping environment to be used. There are several options for DSP prototyping they could be chosen, such as MCU development boards, or software-based DSP setups using Python, MATLAB, or LabVIEW. For this project, MCUs were selected as the preferred development platform, as they are more representative of what a commercialized fluidic circuit reader might look like using portable embedded systems.

The Teensy 3.6 development board was selected for its hardware superiority over many other development boards, such as the popular Arduino series, and its ease of programming. In terms of hardware, the Teensy board features an NXP MK66FX1M0 MCU chip. With an ARM Cortex-M4 processor running at a 180 MHz clock speed, it is a very fast MCU on the market today. While this high computational ability of this MCU may be significantly greater than what is required for this system, it reduces the likelihood that computational issues interfere with prototyping. Furthermore, the MK66FX1M0 includes a highly capable 16-bit analog-to-digital converter (ADC) capable of sampling at moderately high frequencies due to its fast successive-

approximation-register design. As a development board, the Teensy 3.6 includes all low-level hardware that must be connected to the microcontroller (oscillators, voltage regulators, etc.). On the programming side, the Teensy 3.6 is bundled with an integrated development environment that readily allows the MCU to be programmed over USB. There are also many excellent third-party libraries that facilitate the programming of the DSP objectives. Finally, the board can be configured to be USB serial device whose data can be read on any PC through a simple serial port monitoring program.

6.2 Analog-to-Digital Conversion

With the analog front end having been designed for low-noise, it is paramount that the analog-to-digital conversion process preserve this through proper design technique. The two pertinent decisions here are the ADC bit depth and sampling rate. Bit depth is chosen to increase the accuracy of the quantization process at the tradeoff of more memory needed for each sample. The more bits there are in an ADC, the greater the dynamic range of the signal can be

$$SQNR = 20\log\left(2^{Q}\right) \approx 6 \text{ dB}$$

The 16-bit ADC included in the Teensy 3.6 permits 96 dB of dynamic range above quantization noise ($SQNR(Q = 16 \text{ bits}) \approx 96$ dB). The signals to be measured by the ADC only need a fraction of that dynamic range, resulting in a high SNR (due to low quantization noise). Next, the sampling rate of the ADC must be chosen. The key consideration that informs the choice of sampling rate is the deleterious discrete-time phenomenon known as aliasing, which refers to potential ambiguity in determining the frequency of a discrete-time signal due to multiple valid interpolations. In order to prevent aliasing, the sampling rate of a ADC must be at least twice the highest frequency in a bandwidth-limited analog signal, a principle commonly known as the Nyquist-Shannon sampling theorem. Since the highest nominal frequency of AC fluidics signals is 1 kHz, a simple application of Nyquist-Shannon would be to sample at exactly double this highest frequency: 2 kHz. However, this would be ill-informed for this system, as it would require very strong analog filtering in order to attenuate all frequencies above 1 kHz to a level at which no significant aliasing occurs. With a 16-bit ADC, the nominal anti-aliasing filter requirement is -96 dB attenuation at the Nyquist frequency to place all stopband frequencies

under one LSB, effectively eliminating those frequencies as long as they are not greater in magnitude than the passband frequencies. Such a strong analog filter would like have a pole count that is greater than ten, resulting in a system with high component count and low stability, as the higher the order of an IIR filter (which can be analog or digital), the more sensitive it becomes to inevitable variations in the locations of its poles. Although low-tolerance components could be utilized to build such a filter, the cost is unappealing when there are more efficient solutions at hand.

A more efficient method utilized in this system is to sample the AC fluidics signal at a rate that is much higher than the minimum theoretical rate of 2 kHz. By sampling at a higher rate, a lower order analog anti-aliasing filter can be used, because the Nyquist frequency (sampling rate divided by two) increases. For a specified amount of attenuation at a given frequency in a filter stopband, a higher filter order is required if that frequency is closer to the filter cutoff. Therefore, by extending the frequency difference between the anti-aliasing filter cutoff and the Nyquist frequency, we can digitize a signal with higher fidelity and no appreciable aliasing despite having a lower-order analog band limiting filter. The sampling rate was chosen to be twenty times the nominal bandwidth of important AC signals: 20 kHz, resulting in the Nyquist frequency being 10 kHz, or ten times greater than the 1 kHz AC fluidics spectrum. To achieve -96 dB attenuation at 10 kHz from a 1 kHz cutoff of -3 dB, the analog Butterworth filter must be fifth order. A filter of this type can readily be implemented using 1% E24 series resistors and 5% E6 series capacitors with no more than ±1 dB of magnitude error (typically occurring near the corner frequency).

6.3 Downsampling

While the above design choices result in a high-fidelity analog to digital conversion process, they result in a certain drawbacks to the captured signal. First of all, the signal, having been sampled at a high sampling rate, has many more samples than are strictly necessary for frequency analysis up to 1 kHz. In fact, the signal has exactly ten times more points than are necessary for this purpose, resulting in large memory use and potentially high computational expenses for further

signal processing and analysis. Second of all, the signal is still not actually bandwidth limited to the 1 kHz nominal AC fluidics spectrum, resulting in much unwanted frequency information being contained in the signal.

Luckily, both of these issues can be resolved by downsampling the signal. Downsampling is process of digitally lowering the sampling rate of a digital signal while still preserving non-aliased frequency content. This produces a smaller, more compressed signal that can greatly increase subsequent processing efficiency; the common motivation for multirate signal processing. Moreover, the classic fast Fourier transform (FFT) algorithm has a computationally performance trend of $\mathcal{O}\left(n \log_2 n\right)$, meaning that reducing the input signal points by a factor of ten results in an approximate FFT performance increase of a factor of thirty-three: well justifying the incorporation of the signal downsampling, considering that the FFT is usually the most taxing signal processing algorithm in a frequency-analysis system.

To downsample a signal by an integer factor M, it is fairly intuitive to remove samples from the signal and only keep every M^{th} sample (known as decimation by a factor of M). However, low-pass filtering must be done before decimation, or else the risk of aliasing occurs. To explain, after a signal is decimated by a factor of M, the frequency domain is stretched by a factor of M, and since the frequency domain of a discrete-time signal is periodic, aliasing will occur if any overlapping occurs between the periodic, stretched spectra of the signal. Low-pass filtering with a normalized cutoff frequency of $\frac{\pi}{M}$ solves this problem very effectively. The digital filter design has much to consider here. First of all, unlike continuous-time filters, the performance of a discrete-time filter of a given order will decrease the lower the cutoff frequency. With the M factor being equal to ten in our system, obtaining a nice digital filter would require very higher order. Since filtering a finite-duration sequence is $\mathcal{O}\left(n^2\right)$, this could lead to a significant performance decrease that contradicts our motivation for downsampling in the first place.

To optimize the downsampling, the multistage filtering method was used. Multistage filtering consists of splitting up a filtering and downsampling task into multiple steps, each of which

occurring significantly faster than if the entire bandwidth reduction were implemented as one high-coefficient filter. For this system, the stages were setup as three series of $\omega = \frac{\pi}{2}$ filters, which results in a net $\omega = \frac{\pi}{8}$ cutoff, rendering the final signal bandwidth 1.25 kHz, which is close enough to the 1 kHz for our purposes. Filtering was done using an 10th-order Butterworth digital IIR filter with a cutoff of $\omega = \frac{2\pi}{5}$, in order to increase attenuation at $\omega = \frac{\pi}{2}$. This is possible due to the very computationally efficient nature of IIR filters.

6.4 Signal Averaging

Signal averaging is a signal processing technique where a set of replicate time-domain measurements are averaged at each corresponding sample between the replicate epochs. If there is a common signal in each epoch that is properly aligned in time, then constructive interference occurs, and the common signal passes through. Noise and interference are uncorrelated, so they are averaged out over time. The primary advantage of using this filtering technique is its effectiveness at filtering noise that is not significantly outside the spectra of AC fluidics signals (10 Hz to 10 kHz). The quintessential one that shows up is mains interference, usually occurring at 60 Hz and to a lesser extent at its harmonics. Instead of using linear filters to notch or high-pass the suspect frequencies, waveform averaging solves the issue while not reducing the bandwidth of AC fluidic signals, and it does so in a generalized manner that is immune to changes in the frequency of common interference sources.

In order to ensure the proper use of signal averaging, the following conditions must be met:

1. The signal waveform must be repetitive (but not necessarily periodic or occurring at regular intervals)

2. The noise must be random and uncorrelated with the signal (i.e. not periodic with the signal)

3. The temporal position of each waveform must be known

The first and third conditions are straightforward to assert for this instrumentation system, as multiple measurements of AC fluidic systems are taken in regular succession (repetitive waveform satisfying first condition) and the time at which it happens is controlled digitally (known temporal position satisfying third condition. The second condition may seem untenable due to the fact that 50 Hz or 60 Hz mains interference could theoretically occur at the resonant frequency of an AC fluidic system or a harmonic thereof. However, this is a misunderstanding of the problem. The pertinent factor is not whether the noise/interference is harmonically related to the AC fluidics signal, but rather, whether it is related to the rate of signal repetition. Imagine that both the resonant AC fluidic frequency and mains frequency are 60 Hz. Although these two distinct signals may have the same fundamental frequency, they are not necessarily phase-locked, because mains interference will continue regardless of the state of the AC fluidics instrumentation. In contrast, the phase of the AC fluidics signal is reset every time the piezo buzzer is driven, and the rate of this resetting is determined digitally. Therefore, mains interference can only bypass the signal averaging if the refresh rate of the signal collection is harmonically related to the mains frequency. While this is extremely unlikely in practice, the refresh rate of the instrumentation is nonetheless specifically chosen to not be a divisor of either 50 or 60 Hz (11 Hz).

Having justified the use of signal averaging, two design decisions remain: whether to perform linear filtering before or after signal averaging, and what order the signal averaging process should be. Since signal averaging is not an LTI operator, it may not be commutative with LTI filtering. An important recognition for this optimization problem is that the decision to use multirate signal processing in this system mandates that downsampling be done after filtering in order to prevent aliasing from occurring. Therefore, the question truly becomes whether signal averaging should be done before or after downsampling, as filtering is necessary to proper downsampling. The first solution to this problem is a refutation of the earlier premise that signal averaging and LTI filtering are not commutative. Although signal averaging is not an LTI operator because it has a nonlinear, time-varying frequency response, the averaging operation that is done on aligned samples between time epochs is linear. Thus, when this linear averaging

is combined with linear filtering, commutability applies, so order has no bearing on the final signal produced.

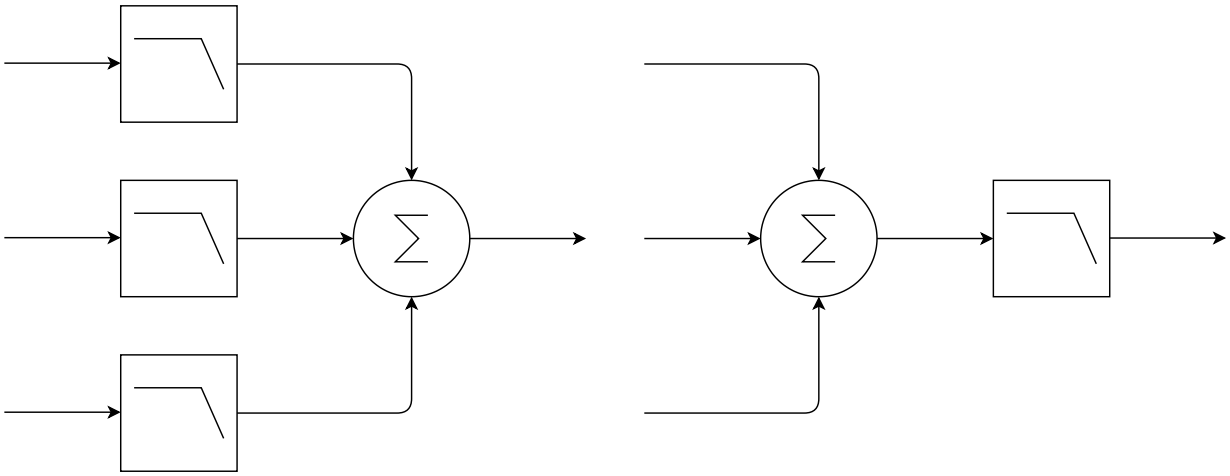

Figure 6.2. Signal flow diagrams of filtering before averaging (left) and vice versa (right).

Therefore, the ordering problem only concerns efficiency. As shown in the block diagrams above, there is a memory tradeoff associated with this decision. More filtering stages are required if downsampling is done before averaging, and in the opposite case, the averaging operation must store and process more points since the inputs are not downsampled. While this may seem like a stalemate between the two options, the filtering before averaging option is actually more memory efficient, because the separate filtering stages do not need to all run at every iteration of the signal processing loop. Each iteration produces only one novel input signal, while all other inputs to the averaging function remain the same until they are eventually discarded. Therefore, as long as we store the previous inputs to the averaging function, then the only the novel input signal needs to be filtered. With this optimization, both topologies require only one filter stage to execute during a loop iteration, in which case, placing the downsampler before the averaging operation reduces the computational expenses needed by the latter. If this system had dynamically changing inputs to the averaging stage for every loop iteration, then this optimization would not be possible, and the correct ordering of the downsampler and averager

would depend on the relative memory sizes of the two, which are subject to change from variations in filter order and sampling time.

6.5 Digital Differentiation

Technically, there is no such thing as digital differentiation, as calculus does not exist in discrete-time. The proper terminology for the discrete-time operation analogous to continuous-time differentiation is simply differencing. There is no rational transfer function that can exactly match the desired differentiator frequency response of $H\left(e^{j\omega}\right) = j\omega$, but close approximations are available, while also being computational efficient. The first-difference differentiator has the following time domain LCCDE:

$$y_{fd}[n] = x[n] - x[n-1] \tag{6.1}$$

The downside to the first-difference differentiator is its propensity to amplify high-frequency noise. The central difference differentiator improves on this, but a more recent contender in the digital differentiator race appears to be even better at maintaining linearity while reducing noise levels [34]:

$$y_{pro}[n] = \frac{-3x[n]}{16} + \frac{31x[n-1]}{32} - \frac{31x[n-3]}{32} + \frac{3x[n-4]}{16} \tag{6.2}$$

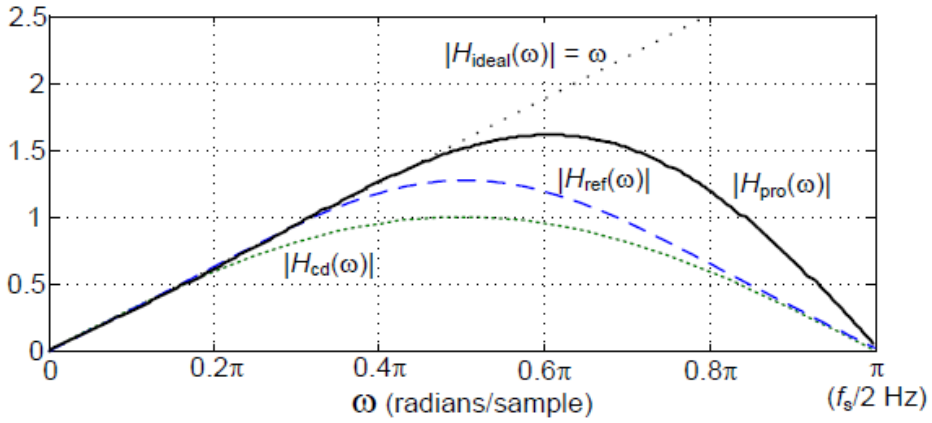

Figure 6.3. Normalized frequency response of various digital differentiators. Taken from [34].

Since most of the bandwidth of the downsampled signal can contain important resonance signals, there is no appeal to using a central-difference differentiator, or anything else with a low-pass rolloff.

6.6 Frequency Analysis

The final step of the signal processing is to conduct frequency analysis to determine the resonant frequency of the AC fluidic system under measurement. Naturally, the algorithm used to conduct this analysis is the FFT. Before the FFT is done to the average, downsampled signal, it is zero padded in order to increase the point count of the FFT, increasing the accuracy of subsequent peak calculations. With 64 final signal samples padded with 128 zeros for a total sample count of 172 and a sampling rate of 2.5 kHz, the frequency resolution of the discrete frequency domain is about 15 Hz. Although this may seem like a wide range for a design choice that effectively determines the frequency resolution of the signal processing, interpolation is used to approximate major peaks between the FFT points. Several interpolation methods exist, but the one utilized for this system is based on the parabolic curvature of adjacent frequency samples [35].

$$f_{\text{peak}} = (k + \delta)\frac{f_s}{N} \tag{6.3}$$

$$\delta = -\,\Re\left[\frac{x_{k+1} - x_{k-1}}{2x_k - x_{k-1} - x_{k+1}}\right] \tag{6.4}$$

A von Hann window is applied to the signal in order to reduce the effect of low-frequency spectral leakage from obscuring the resonance peak. The accuracy of the peak detection is quite good, as the noise margin of the system is as low as 0.1 Hz for low-frequency signals. This can allow subtle changes in the elastic state of a clot to be measured. Finally, a moving average FIR filter is applied to the stream of resonant frequency values to smooth the curve. Since this curve, corresponding to clot firmness over time, has no frequency-encoded information, the moving average filter is optimal for reducing random noise and preserving the time-domain shape and transient characteristics of the curve. The order of this filter is 32, which is high enough to

remove noise without producing slow transient responses or high group delay. In order to reduce the output data size, the resonant frequency is transmitted over USB serial only every other DSP cycle, resulting in an effective refresh rate of 5.5 Hz.

The number of FFT points is made to be a power of two in order to enhance the speed of the operation. The transient response of the filtering stages are removed in order to preserve point count throughout the filtering process, at the expense of some ripple in the frequency domain due to the rectangular windowing effect.

Chapter 7: Medical Experiments

7.1 Objectives

Having designed the fluidic circuit for optimal clot measurement, and the instrumentation to readily perform those measurements, clotting experiments were ready to be undertaken. The primary goal of these experiments is to confirm or reject our models in chapter 4 that support the ability of fluidic circuits to perform elasticity measurements. Furthermore, these experiments provide an opportunity for any practical issues associated with fluidic circuit to present themselves, such as thermal faults, fluid leakage, the formation of bubbles, instrumentation shortcomings, and difficulties with injecting a sample. Data was collected from the serial output of the MCU development board through a USB serial monitor application, and saved to CSV files on a PC.

7.2 Thermal Control of Device

The baseline resonant frequency of an AC fluidic circuit will vary depending on the temperature of the fluid medium, as viscosity is strongly temperature-dependent. Liquid viscosity usually decreases as temperature increases, resulting in an increase in resonant frequency through a loss of fluid inductance. If such a temperature change occurs during an experimental run using the device, it can produce signal increases that may be falsely interpreted as a change in blood elasticity.

In order to better understand the significance of this issue, let us examine an AC fluidic device without temperature regulation on the driving fluid. With body temperature (37 °C) as the highest temperature on this range and room temperature (20 °C) as the lowest, the dynamic viscosity of water changes by about 30%. This results in a change of resonant frequency by a factor of $\sqrt{30}\,\% \approx 5.5\,\%$. This change is not large relative to the shifts induced by the clots in the device (next section), but can still be observed after placing a room temperature fluidic circuit on a 37 °C hot plate.

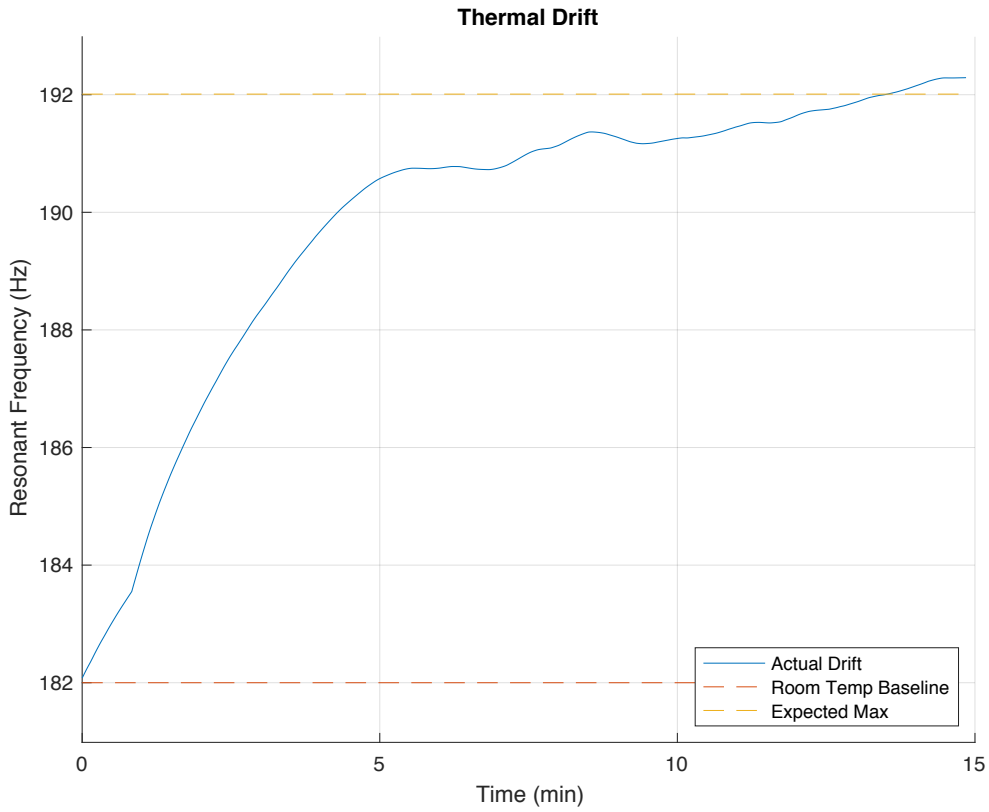

Figure 7.1. Thermal drift of fluidic circuit on hot plate, approaching maximum expected increase level corresponding to the difference between room and body temperature.

Furthermore, as the temperature increase settles to approximately 37 °C, so does the corresponding increase in resonant frequency. Hence, warming AC fluidic cartridges on 37 °C hotplates was chosen as an adequate method of thermal control for the sake of experimentation.

7.3 Fibrinogen-Thrombin Gel Experiment Setup

Clinically-relevant evaluations of the fluidic circuit's ability to measure clot elasticity were made using gels formed with fibrinogen and thrombin. By adding thrombin to fibrinogen solutions, fibrinogen is converted to fibrin, forming a clot. Varying the concentration of the fibrinogen solutions allows us to control the relative clotting strength and kinetics between different solutions. This forms the basis for this set of experiments. AC fluidic results are compared to identical gel samples being measured by a ROTEM Delta device.

Fibrinogen solutions were made in a 1x PBS buffer of pH 7.4. The fibrinogen concentrations for these experiments were set to 200, 400, and 800 mg/dL. This concentration range captures the normal concentration range of fibrinogen in human plasma (200-400 mg/dL), plus an additional high level to emulate stronger clotting (800 mg/dL) [36]. The use of fibrin gels for biomedical experiments is justified by the significance of fibrin levels to coagulopathy. Many coagulopathies, such as dilutional coagulopathy and thrombocytopenia, are clinically detected through the measurement of fibrin clots derived from patient whole blood [37]. Gold-standard existing clot VE testers include methods to do this measurement on whole blood; for instance, the FIBTEM assay of ROTEM eliminates the contribution of platelets to the clot, allowing fibrin polymerization to be specifically evaluated. Furthermore, using fibrin gels allows us to more precisely control the clotting characteristics of each sample. Blood clotting is a notoriously inconsistent physical process, and simplifying the biosample to just fibrinogen and thrombin helps to reduce variation. This allows for more consistent experimental evaluation of the fluidic circuit. Furthermore, the 200-800 mg/dL fibrinogen concentration range will produce a range of ROTEM values that extend down close to the minimum output signal (1 mm) [38]. This is representative of the low-end elasticity dynamic range of modern VE testers. The maximum expected ROTEM output (for the 800 mg/dL fibrinogen concentration) is expected to be at around, or higher than, the typical FIBTEM result of approximately 15 mm [39].

Solutions were gently stirred to solubilize the fibrinogen; no shaking or vortexing was done in order to reduce foaming. The fibrinogen stock added also contained FXIII in equimolar amounts to fibrinogen. Before adding thrombin, 10 mM $CaCl_2$ was added to the fibrinogen solution in order to calcify the solution. After calcification, nonspecific binding and spontaneous weak polymerization will occur, making it important to add thrombin and inject the sample into the testing devices quickly. Otherwise, the viscosity of the solution can become too high for proper injection. After adding 0.5 IU/mL thrombin, fibrinogen is cleaved into fibrin and FXIII is activated to FXIIIa, which cross links fibrin monomers and forms the elastic clot. For the negative control, no thrombin is added to a 800 mg/dL calcified fibrinogen solution. The temperature was strictly kept at 37 °C by placing the device on an aluminum hot plate with

closed-loop temperature control in order to standardize the kinetics of the fibrinogen cleavage and fibrin cross-linking across experimental trials. The fibrinogen solution samples were also preheated to 37 °C to normalize cleavage and polymerization kinetics. In addition, this keeps the internal fluid of the fluidic circuit at a standard temperature, which is important for managing the baseline resonance of the device, as described earlier in this chapter. Because the ROTEM Delta is used as a control in these experiments, the ROTEM's hot plate was used, ensuring minimal systematic temperature differences between fibrin gel samples in the ROTEM and fluidic circuits. Samples were allowed to polymerize for at least 30 minutes in either device. For each concentration of fibrinogen, the results of three trials are averaged for inclusion in the primary analysis. Due to some procedural difficulties in injecting samples without the formation of bubbles, as well as the catastrophic formation of bubbles during clotting, such data is not used in the analysis, and given commentary in the later sections of this chapter with regards to deleterious phenomena that may occur in this system.

7.4 Fibrinogen-Thrombin Gel Experiment Results

The first dataset of interest is a direct comparison of the AC fluidics results for different fibrinogen concentrations. This data, although not yet referenced to ROTEM, can demonstrate sensitivity solely through differences found in the relative shapes of the curves. The following plots show data from the three trials of the device for each fibrinogen concentration. No filtering is applied to the curve in order to gain maximum insight as to the functionality of the device, apart from that inherent to the DSP of the system. The results (next page) show correlation between the curves of each trial for each fibrinogen concentration level. There are obvious artifacts in the signal that deviate from the classic smoothness of a thromboelastogram, such as swift peaks and valleys. In some cases, there are prolonged surges and/or dips in the signal that appear to “correct” themselves later on. These causes and implications of these signal artifacts are discussed in the later sections of this chapter. Nonetheless, the overall correlation of the signals to one another for each fibrinogen concentration is highly promising. In all cases, the system appears to maintain the operational capacity to measure the clot over the 40 minute trial period.

Figure 7.2. Resonant frequency increases for three trials of 200 mg/dL fibrinogen clots.

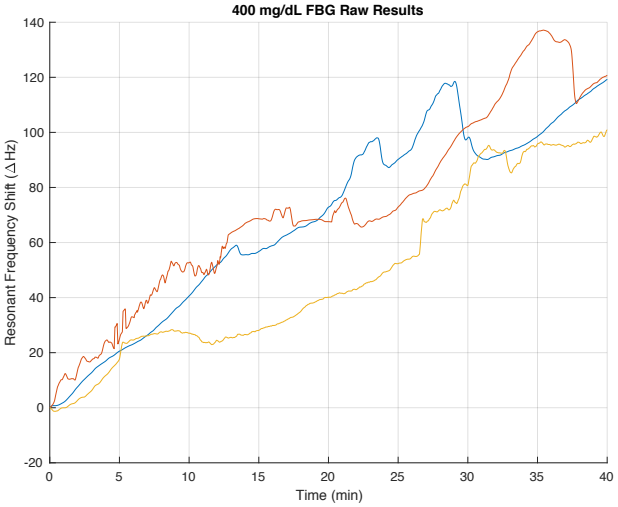

Figure 7.3. Resonant frequency increases for three trials of 400 mg/dL fibrinogen clots.

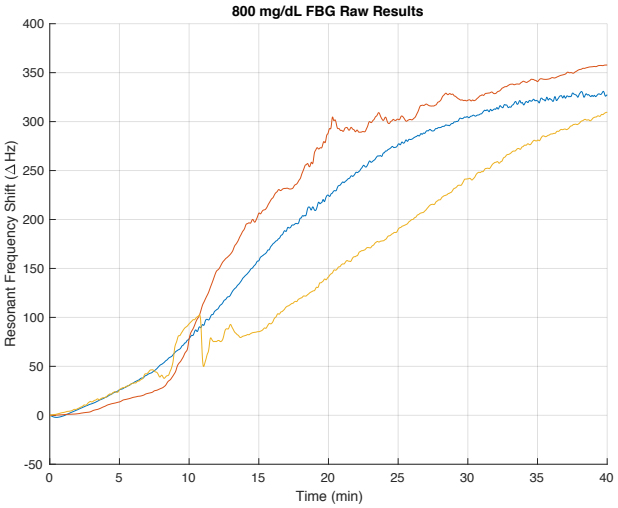

Figure 7.4. Resonant frequency increases for three trials of 800 mg/dL fibrinogen clots.

Now the averages of the trials are taken for each fibrinogen concentration and plotted together for relative comparison against the control with no thrombin added.

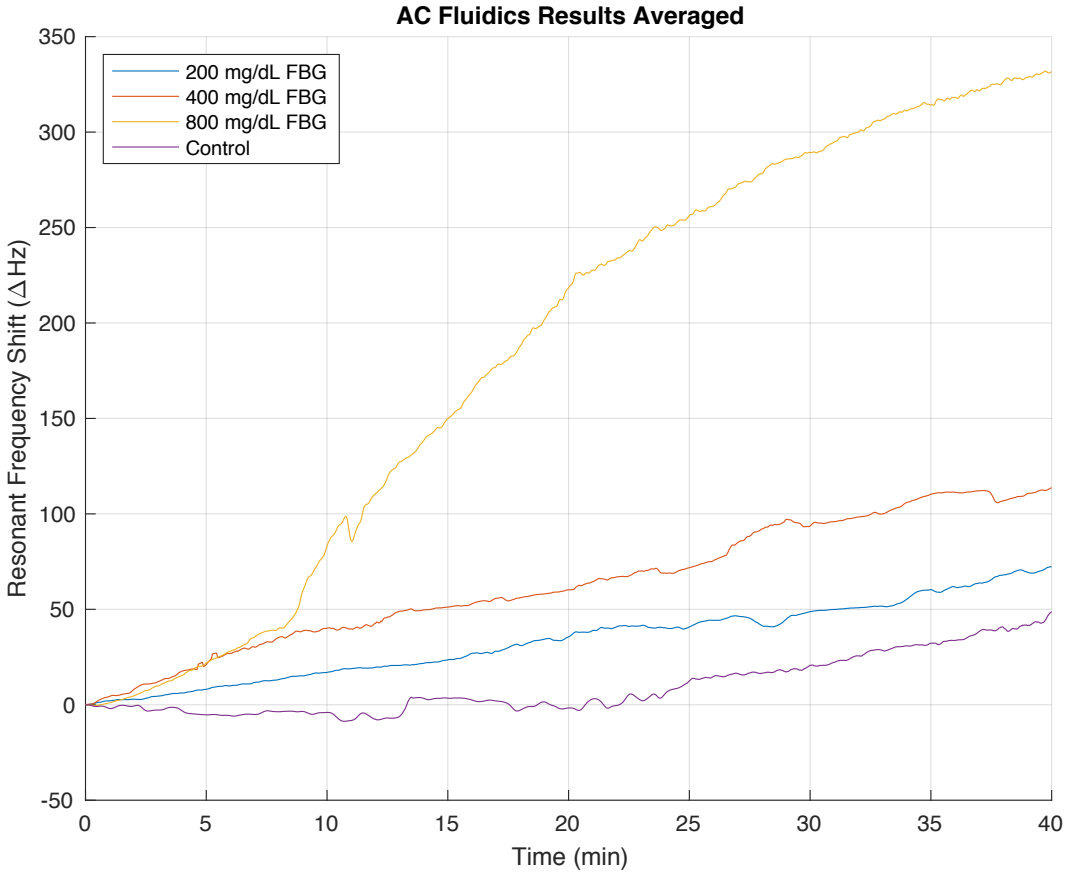

Figure 7.5. Averaged results for each fibrinogen concentration referenced to control without thrombin.

The major differences in the shapes of these curves are readily apparent. The 800 (mg/dL units omitted) FBG curve is very stark, and happens to resemble the classic thromboelastogram, and the 400 and 200 FBG curves are smaller, but still represent significant detection of the lower fibrinogen concentrations. Even the 200 FBG curve is significantly greater than the thrombin-less control. These data suggests that this system can differentiate the elasticity of clots in a sensitive manner, as accounted for in the design process of chapter 4. Now, the data of the fluidic

circuit is compared to a clinically accepted VE testing device: the ROTEM Delta. The raw data from the ROTEM trials are as follows:

Test ID	Thrombin (IU/ml)	A5	A10	A15	A20	A25	MCF
Neg Control FBG800	0	1	2	2	1	1	7
FBG200 Run1	0.5	2	3	3	3	3	3
FBG400 Run1	0.5	8	9	9	10	10	10
FBG800 Run1	0.5	6	11	11	12	12	11
FBG200 Run2	0.5	3	5	6	5	5	6
FBG400 Run2	0.5	6	10	11	11	11	11
FBG800 Run2	0.5	6	10	11	11	12	12
FBG200 Run3	0.5	4	3	3	3	3	4
FBG400 Run3	0.5	7	9	10	10	10	10
FBG800 Run3	0.5	7	11	11	11	12	12
200 Avg	0.5	3.0	3.7	4.0	3.7	3.7	4.3
400 Avg	0.5	7.0	9.3	10.0	10.3	10.3	10.3
800 Avg	0.5	6.3	10.7	11.0	11.3	12.0	11.7

Table 5. Raw data from the ROTEM Delta for the experimental trials. Some entries were originally absent due to a lack of convergence of the ROTEM processing algorithm on its own data. In these places, marked in orange, the last value is repeated. All values from the ROTEM (A5-A25 + MCF) are given in "mm" units.

The ROTEM data falls within the expected range of approximately 0-15 mm for our fibrinogen concentrations [38]. In order to compare datasets between ROTEM and AC fluidics, some educated guesses are required. The signal processing and algorithms that ROTEM utilizes are private, and without that information, we cannot compare the two datasets exactly. Nonetheless, the two datasets are plotted side-by-side. The fluidic circuit results are zero-phase filtered using a

1000-point moving average window in order to allow better comparison between to the ROTEM data, which is likely to be filtered as well.

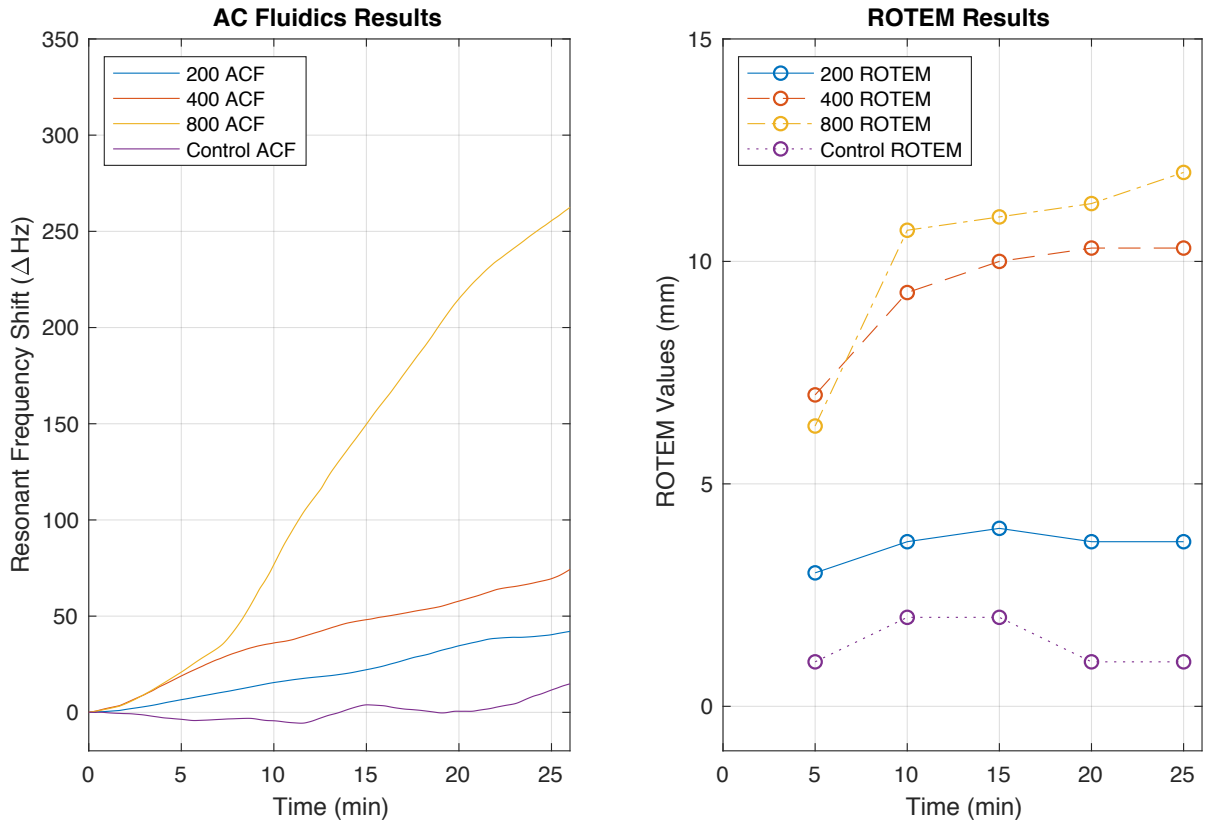

Figure 7.6. Smoothed data curves from AC fluidic system compared to ROTEM. Since the ROTEM data contains few points, linear interpolation is used to produce ROTEM curves.

The ROTEM results, although very undersampled compared to the AC fluidics data, show positive signs for this system. ROTEM was also able to distinguish between the three samples, albeit with a different relative separation of the curves. Furthermore, it appears that the ROTEM results tend to plateau after approximately 10 minutes, while the amplitude data of the fluidic circuits continues to rise significantly even 25 minutes after the initiation of the experiment. Whether this is a signal processing difference or instrumentation difference between the two devices is hard to gauge. One possibility is that the mechanically oscillatory nature of the ROTEM device results in weaker clotting action, contrary to speculation that low-frequency

mechanical emulation of venous cardiac pulsations improve clotting [40, 41]. At the very least, the continued amplitude gain over time in AC fluidics is probably not a deleterious trait of the instrument, as during the critical first 10 minutes of the measurement, the resonant frequency of the device is increasing alongside ROTEM. In fact, the amplitudes and slopes of the different FBG concentration curves are arguably easier to distinguish than the ROTEM data. This may be the most important finding of this experiment- that AC fluidics can provide a more rapid insight into sample elasticity than ROTEM. If the ROTEM data were sampled at a higher rate, then it may be easier to get rapid elasticity information on the device, but the very slow sampling makes it difficult- a limitation of the cup-and-pin instrumentation method. This is another reason to value the high-speed instrumentation of AC fluidic circuits. The high throughput rate of the AC fluidics instrumentation allows for nearly continuous curves to produced with no interpolation and no estimation; just instant information.

We can attempt to form a direct comparison by normalizing the ROTEM results to the AC fluidic results. The 5-minute ROTEM value for the 800 mg/dL fibrinogen solution was aligned to the 5-minute resonant frequency value of the fluidic circuit for the same fibrinogen concentration. The highest fibrinogen concentration was selected as the normalization basis, due to the higher expected signal-to-noise ratios in both systems. After the 5-minute ROTEM sample, the remaining ROTEM samples are linearly scaled with respect to the 5-minute sample. For other fibrinogen concentrations, the 5-minute amplitude is linearly scaled according to their ratio with the 800 mg/dL FBG 5-minute standard. The same is repeated in a subsequent plot, but with the 25-minute mark used as the normalization point. Both plot illustrate the lack of linearity between the datasets of the two devices, due primarily to the continued rising amplitude of the AC fluidic data versus the plateauing of the ROTEM data. This results in the dynamic range of the AC fluidic signal being much larger than the ROTEM data.

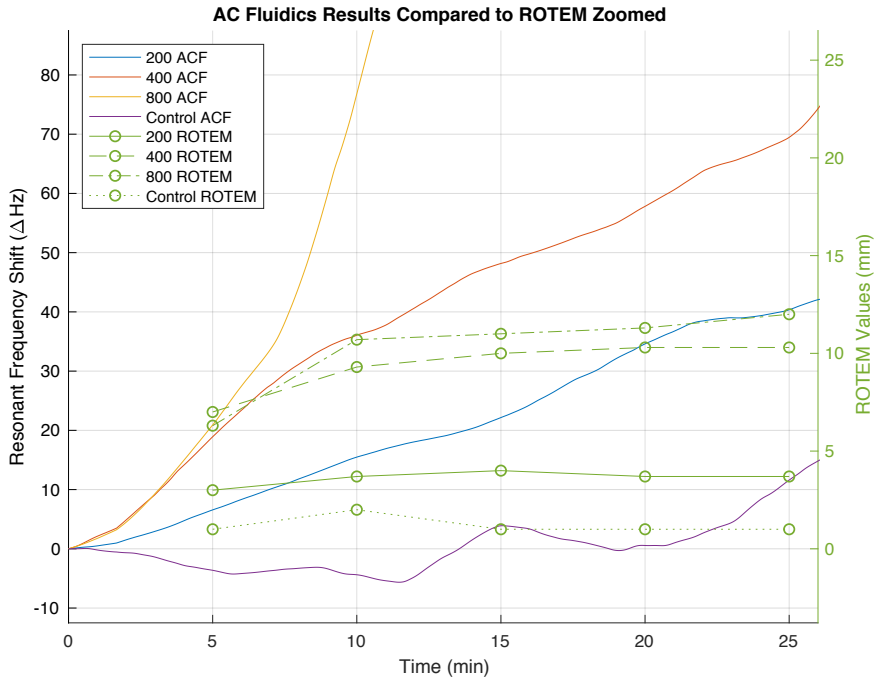

Figure 7.7. Direct comparison of AC fluidic system curves versus ROTEM with alignment taking place at the 5 minute mark.

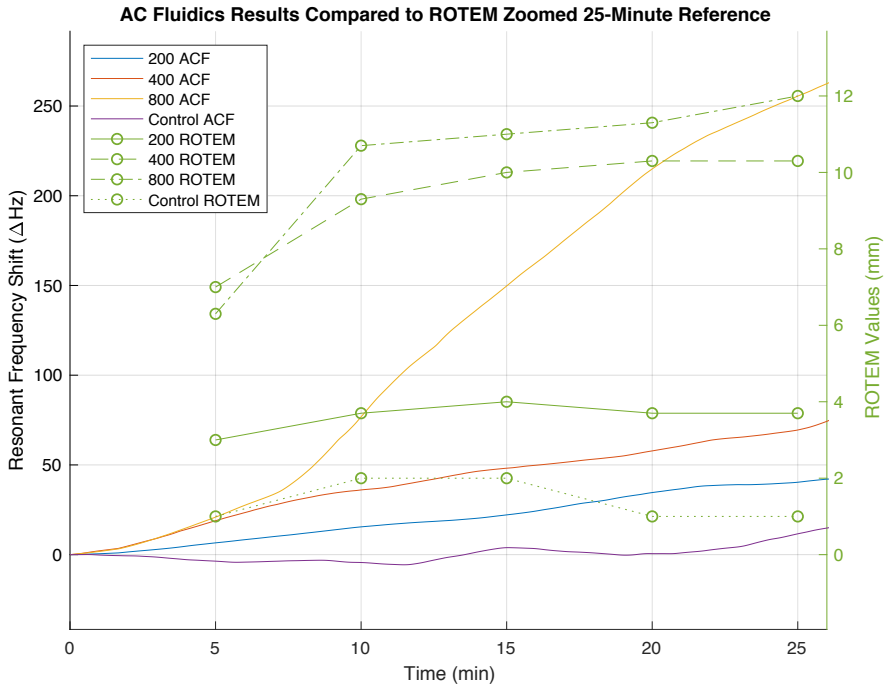

Figure 7.8. Similar comparison but with the ROTEM values referenced to the 25-minute mark.

7.5 Trial Repeatability & Bubble Problems

The ability of this fluidic circuit system to produce consistent, repeatable results was observed. The rate of elasticity change, and the absolute elasticity values at time checkpoints were consistent. However, during various experimental trials not represented in the data above, practical limitations of the technology were encountered. In some instances, the resonant frequency of the device under test surged rapidly, and then returned to the linear baseline.

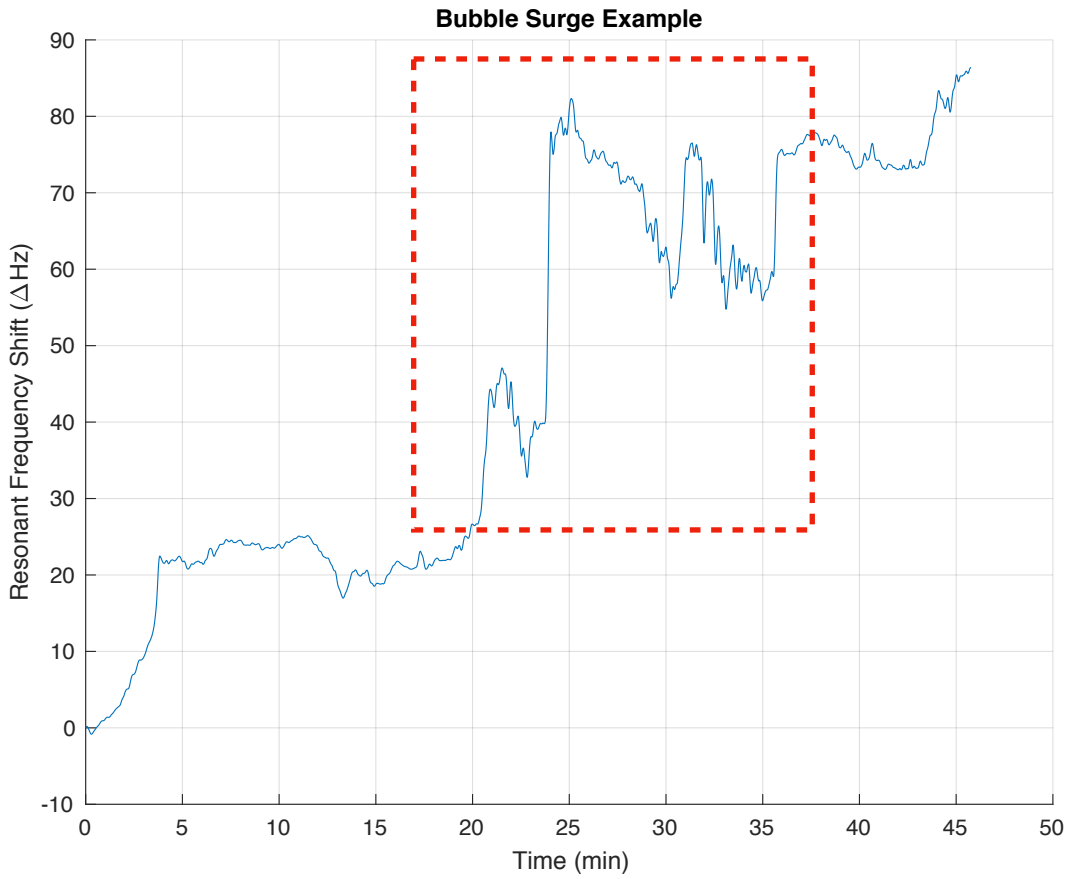

Figure 7.9 Example of bubble surges occurring during trial with 400 mg/dL fibrinogen.

Filtering could be used to smooth these curves out to minimize the impact of such surges on the output. Nonetheless, it is still critical to understand the physical basis behind these surges, which can lead to future optimizations. Incorporating the electric-hydraulic analogy used thus far to

understand AC fluidic systems, an increase in resonate frequency can occur from a decrease in either capacitance or inductance. Since the hydraulic and mechanical analogy for inductance is mass, that would seem unlikely to be the candidate for a sudden drop through the experiment, as mass is entirely conserved in this system. Although fluid dynamic viscosity also affects inductance through direct proportionality, it would be unlikely to increase the resonant frequency, as we expect the viscosity of a fibrin gel to increase over time, which can only lower the resonant frequency, as discussed in chapter 4. Therefore, the most likely basis for this surge is a sudden drop in system capacitance that would be occurring in series with the rest of the fluidic circuit. The most suspect cause of this would a bubble.

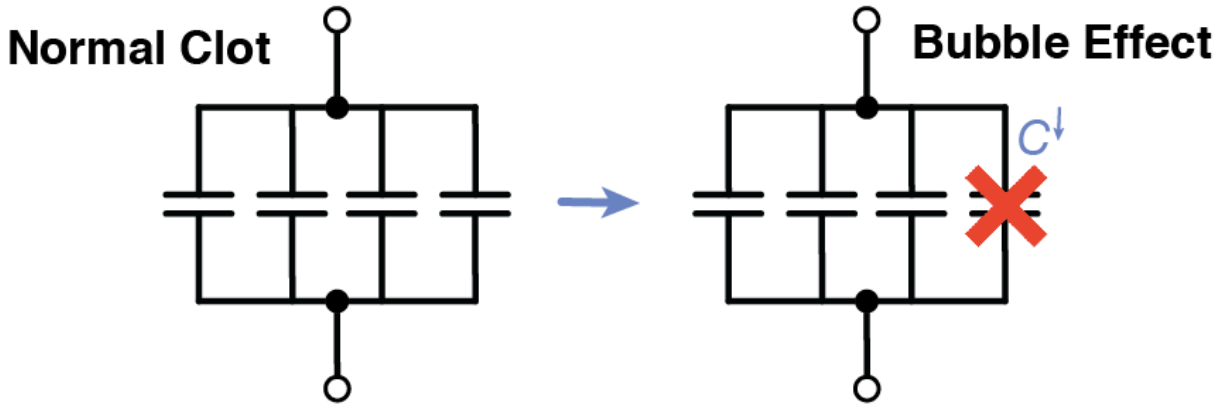

Figure 7.10. Hypothetical bubble mechanism for loss of elasticity near inlet ports.

The bubble surge hypothesis posits that the resonance surge is caused by a sudden loss of capacitance in areas where bubbles are formed, as that area becomes an inelastic, viscous hot-spot. This is most likely to occur near the sample loading inlets inside the well. As the area near the bubble is hardened, the effect of the bubble is mitigated.

Surges in resonant frequency were not the only effects observed, as some trials experienced major dips in resonant frequency. Opposite to the resonance surge effect, this is likely due to a sudden increase in capacitance. Bubbles can actually be valid explanations for this as well, because if a bubble is lodged in a highly-elastic portion of the clot, then the bubble behaves as a more compressible substitution for the clot in that region, increasing the local capacitance.

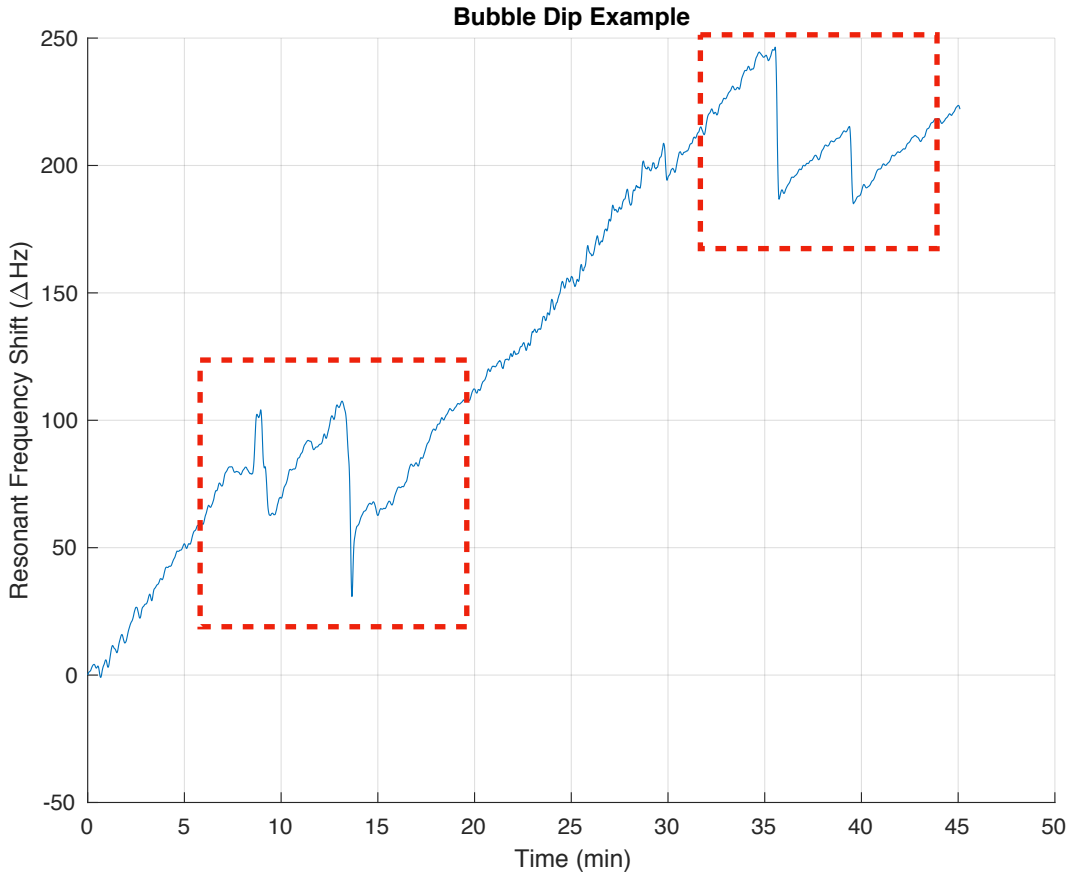

Figure 7.11. Examples of bubble dips during a 800 mg/dL FBG experiment.

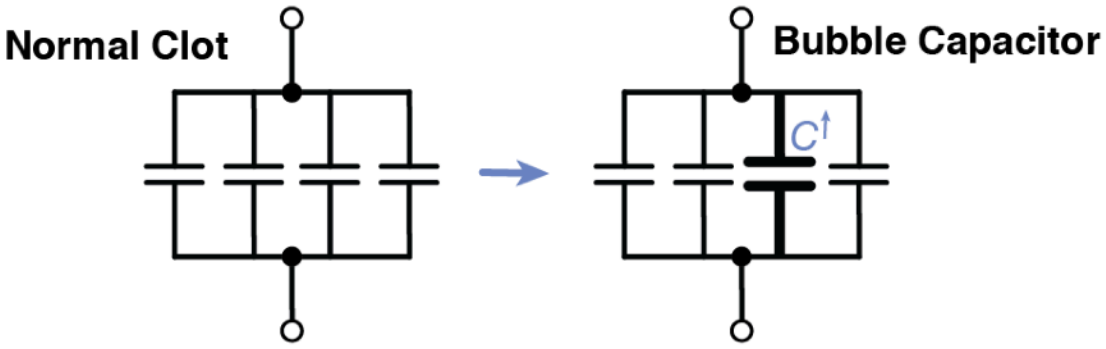

Figure 7.12. Hypothetical explanation for sudden resonance drops.

7.6 Viscous Dips

It was observed that sample viscosity may contribute to the system output. Some samples were observed to decrease the resonant frequency of the fluidic circuits for several minutes before the elasticity-driven frequency increase occurred. The hypothetical cause for this is an increase in inductance that occurs as the sample viscosity increases. This inductance is primarily present in parallel to the elastic capacitance of the clot, because the sample loading inlets provide a pathway to atmospheric ground pressure for viscous, fluidic components in the sample chamber. After enough clotting has occurring, the resistance of these parallel, fluidic channels increases to a point where the inductance no longer has a significant effect on the system. In this way, more optimal circuit designs in the future may seek to maximize resistance in these segments in order to suppress their inductance. However, doing so also increases the inductance, producing an optimization problem.

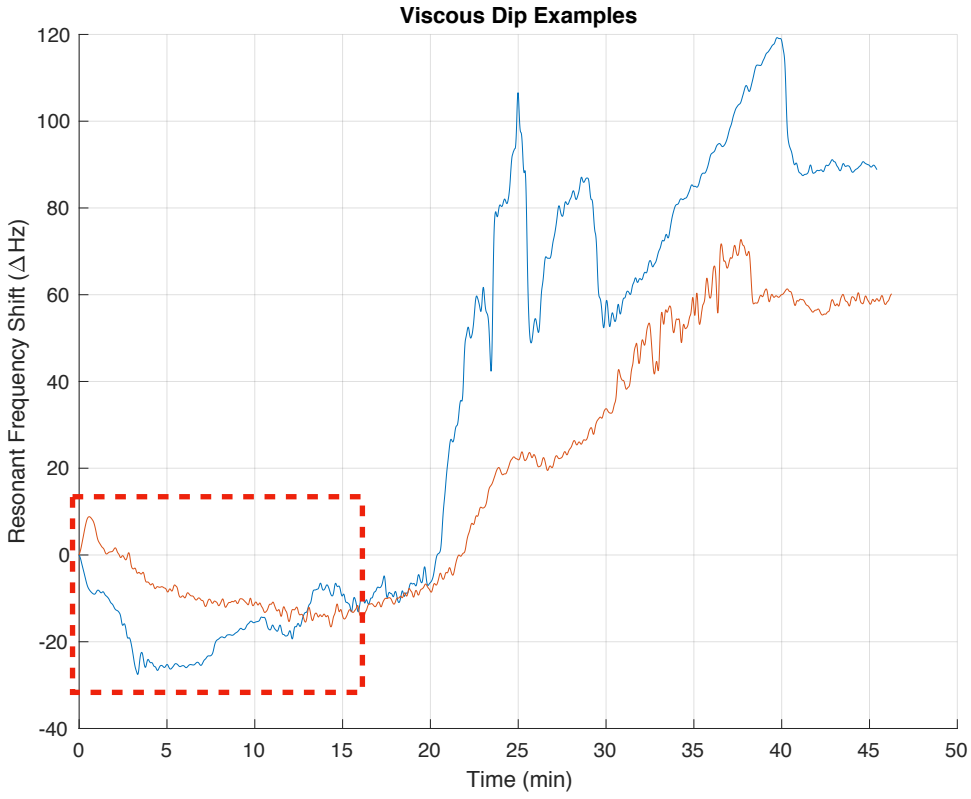

Figure 7.13. Two examples of viscous dips occurring for two FBG trials.

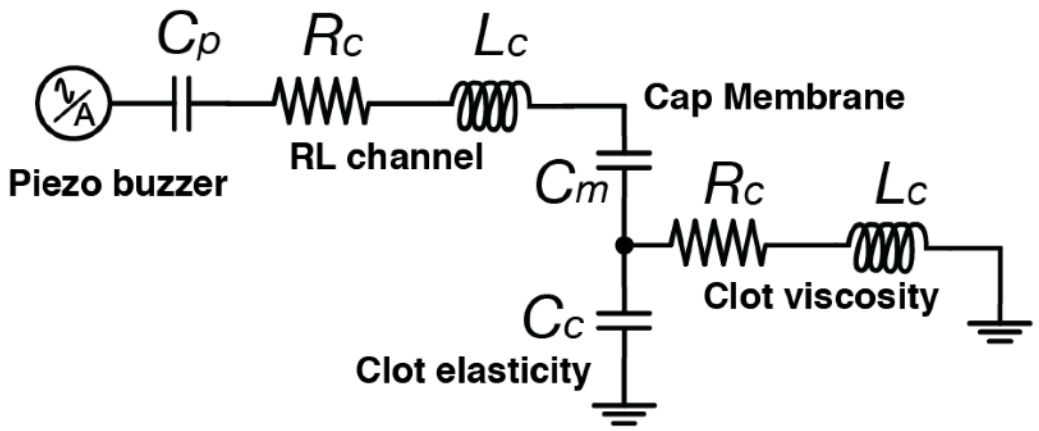

Figure 7.14. Hypothetical explanation for early resonance dips due to viscosity.

Prior to the elasticity of the sample becoming dominant enough to form the "series capacitance" with the membrane capacitor of the fluidic circuit, it can behave primarily as a viscous element. When highly viscous, it forms a serial resistance and inductance with the rest of the system (not parallel due to high impedance of clot capacitor at this time). As the viscosity of the fluid increases, so does its resistance. It was observed that sometimes, this resistance was so large, that the damping of the fluidic circuit was sufficiently high to suppress the ringing almost completely. While the electrical instrumentation of the circuit can still measure the resonant frequency, the lower number of periods in the oscillation increases the error of the resonant frequency estimation, resulting in more noise along the thromboelastogram curve. Nonetheless, the occurrence of such high-damping scenarios was rare, and even during such situations, the output is still accurate with simple noise-reduction filtering.

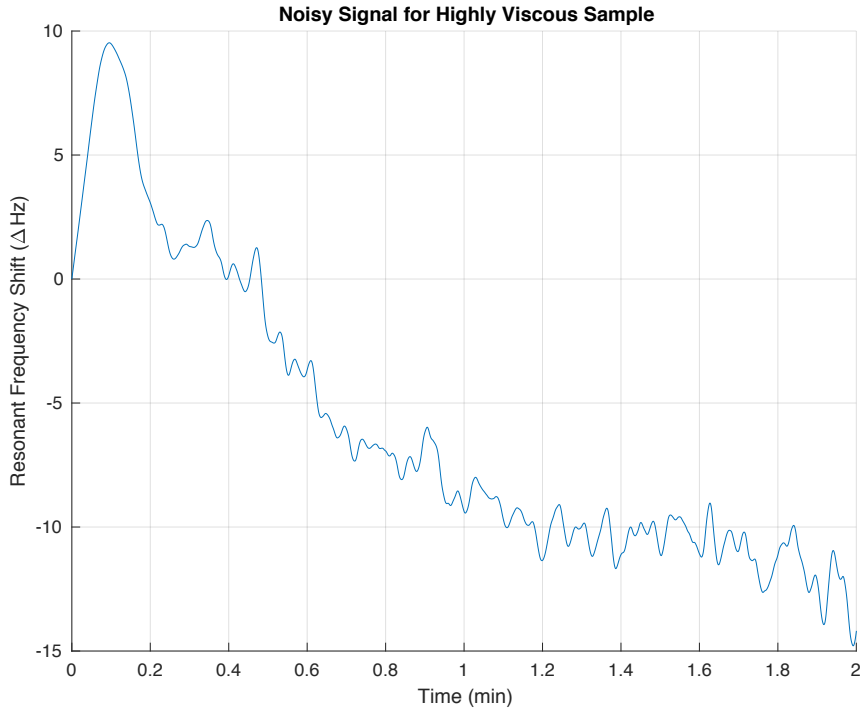

Figure 7.15. Close up of increasing noise during a viscous dip due to damping.

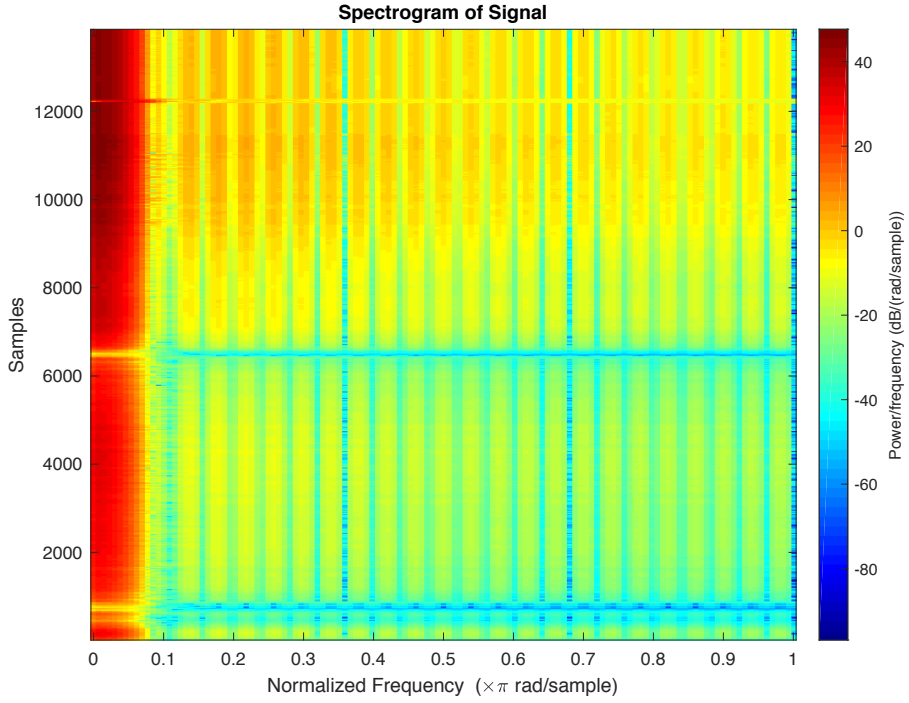

Figure 7.16. Spectrogram shows increasing high-frequency content in above signal over time.

Chapter 8: Conclusions and Discussion

8.1 Conclusions

AC fluidics is a unique and capable instrumentation technology that, when combined with carefully intentioned design, could serve as an inexpensive yet effective blood VE testing device. The successful fluidic circuit design work and implementation of portable instrumentation have conveyed promise to the clinical potential of this technology.

The design work that went into producing a fluidic circuit dedicated to measuring clot elasticity is important for several reasons. First of all, it has produced a system which is capable of limited VE measurements that are arguably as good as a ROTEM device. For the clinical application of point-of-care blood VE testing, this is obviously important. However, this design work has also expanded our scientific understanding of fluidic circuits, and improved our design techniques. The discovery of a valid analytical membrane capacitance expression allows for more ambitious declarations to be made with regard to how fluidic circuits work when loaded with an elastic sample. For instance, without the capacitance expression, we could not use simulation results to confidently affirm the series capacitance hypothesis of how a clot affects the fluidic circuit. The use of simulations also allowed for new, productive fluidic circuit design techniques to be pioneered, namely the use of elasticity response curves to immediate recognize of the design choices necessary to produce a system capable of measuring the minimum elasticity desired. As a general technology, AC fluidics could have other promising commercial applications whose requirements differ considerably from that of blood VE testing. The design techniques used in this work can very well be used to create other fluidic circuit designs tailored to their applications.

With the instrumentation of AC fluidics in a robust and well-documented form, the use of this device for larger-throughput testing with cartridges and viscoelastic samples is more feasible. The upgraded system runs on USB power without any need for an additional battery, and no delicate, expensive optical instrumentation setups are used. The improvements to the

instrumentation front-end electronics increase SNR, which furthers the reliability of resonant frequency detection, especially in cartridges with higher resonant frequencies. These are all technical improvements to the system, but the higher-level consequence of these achievements is the validation that a commercializable product using AC fluidic technology can be made portable.

8.2 Areas for Future Work

During the experiments run with this system, it was placed on a hot plate as a means of temperature regulation. One important objective of future should be the mechanical implementation of a heater into the device. Since water has a high specific heat capacitance, and PMMA is thermally insulative, heating the driving fluidic of a fluidic circuit would not only regulate the baseline resonance of the device, but it would also serve as an excellent mechanism for heating the clot sample. The greatest anticipated difficulty with heating the water would be finding a leak-proof method of heating that bypasses the thermally insulative PMMA. The brass diaphragm of the piezoelectric unimorph transducers may be useful in this way, as they provide a clear thermal access to the underlying fluid. Mechanical implementation of a heater that can warm the brass without disrupting its transduction behavior could be challenging. More inefficient heating methods are also available, like installing a hotplate or oven into the fluidic cartridge reader.

The signal processing of this technology could be further improved to provide results that better resemble that of other VE testers. In a sense, this aspect of potential future work is not so much about the signal processing (sampling, filtering, frequency analysis, etc.) as it is about the algorithmic treatment of the data. All other clinical VE testers use proprietary, secret algorithms to convert the sensor information into the classic thromboelastogram curves. While AC fluidics has demonstrated remarkable ability to specifically measure clot firmness, perhaps on a faster and more sensitive level than ROTEM, the raw data from AC fluidics does not precisely match the shape of the ROTEM curve, mainly due to the continued rise in amplitude after the ROTEM curve begins to plateau. The reasons why this occurs between the two devices could be narrowed

down to a algorithmic intervention by ROTEM, a physics difference in the two sensor types that results in different behavior or measurement of the clot over time, or something else entirely. No matter what the reason for the difference is, clinicians would prefer that the output of AC fluidics closely resemble the characteristic thromboelastogram curves that have been used for decades. Hence, pursuing that resemblance is a worthwhile area of future work for the commercialization of this technology.

The capacitor of this system should be redesigned to preserve the measurement advantages seen in this work while making it easier for a sample to be properly loaded. While injecting fibrinogen solutions, water, and other solutions into the capacitor of this system, it was not uncommon for bubbles to form as the result of high surface tension in the liquid adhering to minor roughnesses on the surface of the capacitor walls. Aside from better fabrication or manufacturing techniques to form a smoother capacitor well, clever designs that take advantage of capillary action, gravity, siphoning, and/or other techniques can make it significantly easier and more consistent to load a sample into a fluidic circuit. This is not only important for the ease of the further research and development, but it is perhaps most important for the clinical personnel who may one day use this technology out in the field, where sample loading problems are unacceptable.

Appendix A: COMSOL Modeling Details

The details of the COMSOL modeling done in this work is documented below. All experiments utilized a similar general setup, comprising a membrane, a clot, and a backing. The exception to this is the capacitance value experiment, because in that case, the clot and backing layer were removed to isolate the capacitor itself.

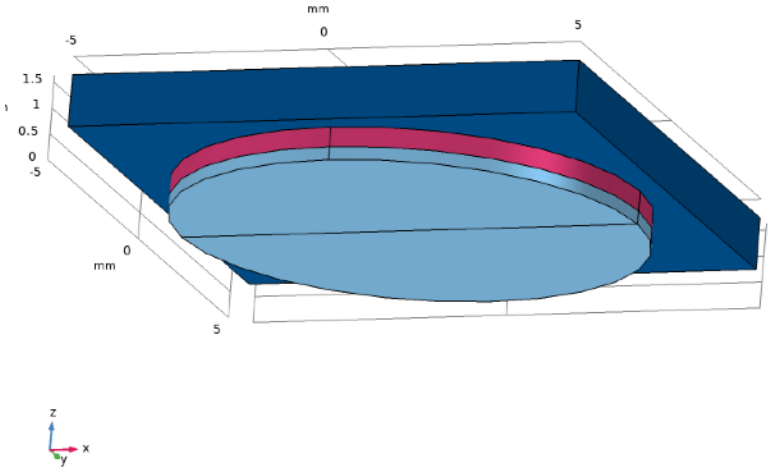

The clot and backing layer geometries were set to be free.

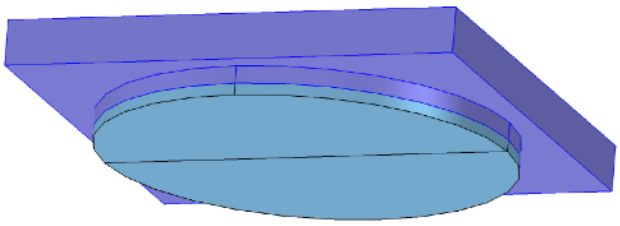

The membrane is not set this way because its perimeter needs to be fixed in order to simulate the bulge of a fluidic capacitor.

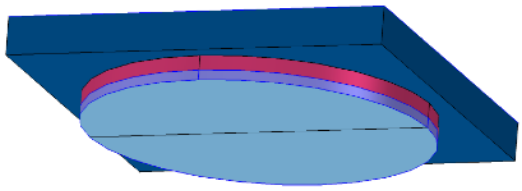

The face of the membrane is receiving the pressure load.

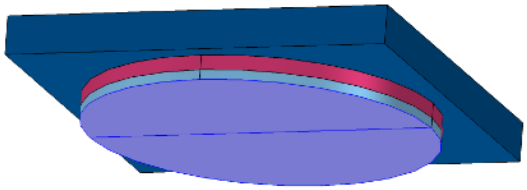

For materials, fixed PMMA parameters are assigned to the membrane and backing layer.

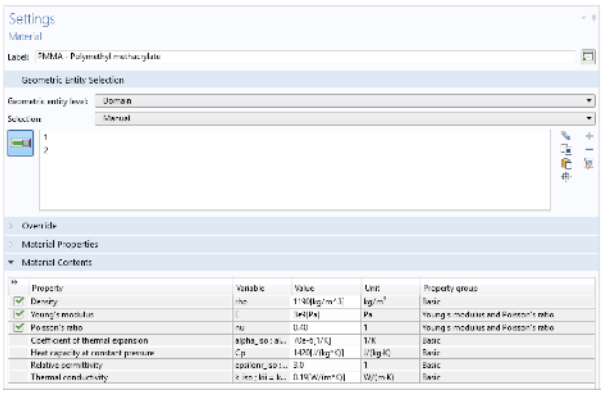

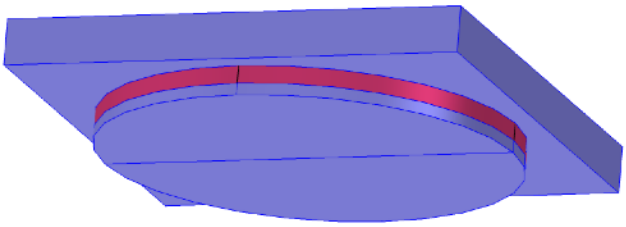

The clot is assigned a material with a mass density close to water to resemble a biological material (although in these steady-state simulations, mass is unimportant) and the elastic modulus is set to be a variable that is changed during experiments.

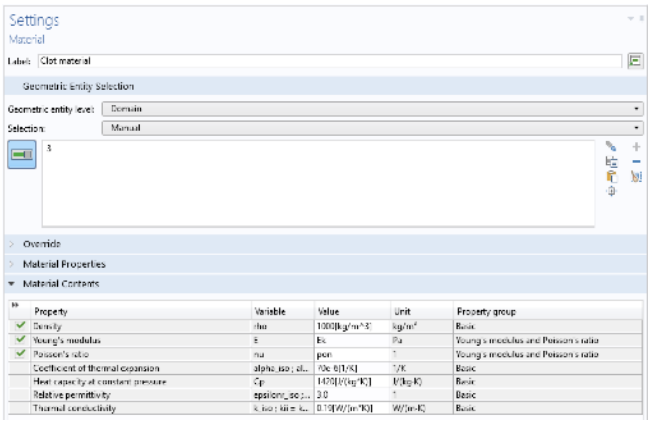

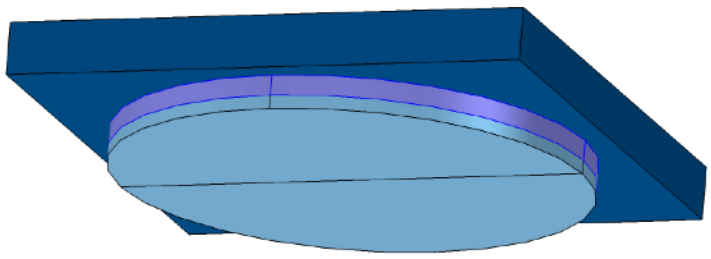

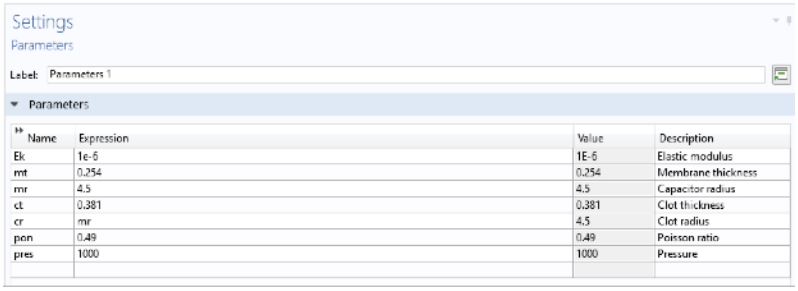

Sweep parameters for each experiment in this work:

Settings

Parametric Sweep

Compute Update Solution

Label: Silicone Disk Response

Study Settings

Sweep type: All combinations

Parameter name	Parameter value list	Parameter unit
Ek (Elastic modulus)	10^{range(5,1/5,8)}	
mr (Capacitor radius)	range(3, 0.5, 4.5)	
cr (Clot radius)	2.25	
ct (Clot thickness)	1	

Settings

Parametric Sweep

Compute Update Solution

Label: Elastic Response

Study Settings

Sweep type: All combinations

Parameter name	Parameter value list	Parameter unit
Ek (Elastic modulus)	10^{range(0,1/4,7)}	
mt (Membrane thickness)	range(0.01,0.04,0.27)	

Settings

Parametric Sweep

Compute Update Solution

Label: Capacitance Values

Study Settings

Sweep type: All combinations

Parameter name	Parameter value list	Parameter unit
mr (Capacitor radius)	range(3,0.5,4.5)	
mt (Membrane thickness)	0.0508, 0.254	
pres (Pressure)	1000	

Settings

Parametric Sweep

Compute Update Solution

Label: Capacitor Linearity

Study Settings

Sweep type: All combinations

Parameter name	Parameter value list	Parameter unit
pres (Pressure)	range(0,0.1,1)	
mr (Capacitor radius)	range(3,0.5,4.5)	

Representative deformation and forces in the simulation

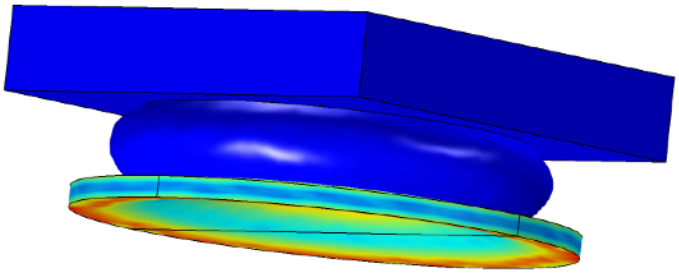

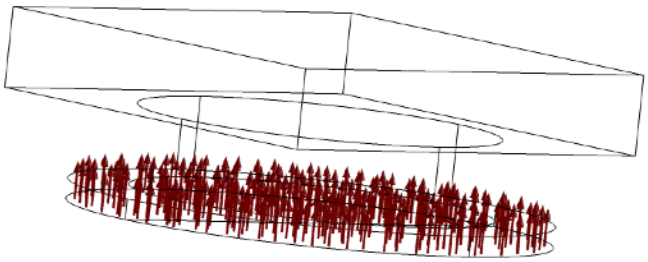

Appendix B: Complete Electrical Schematics

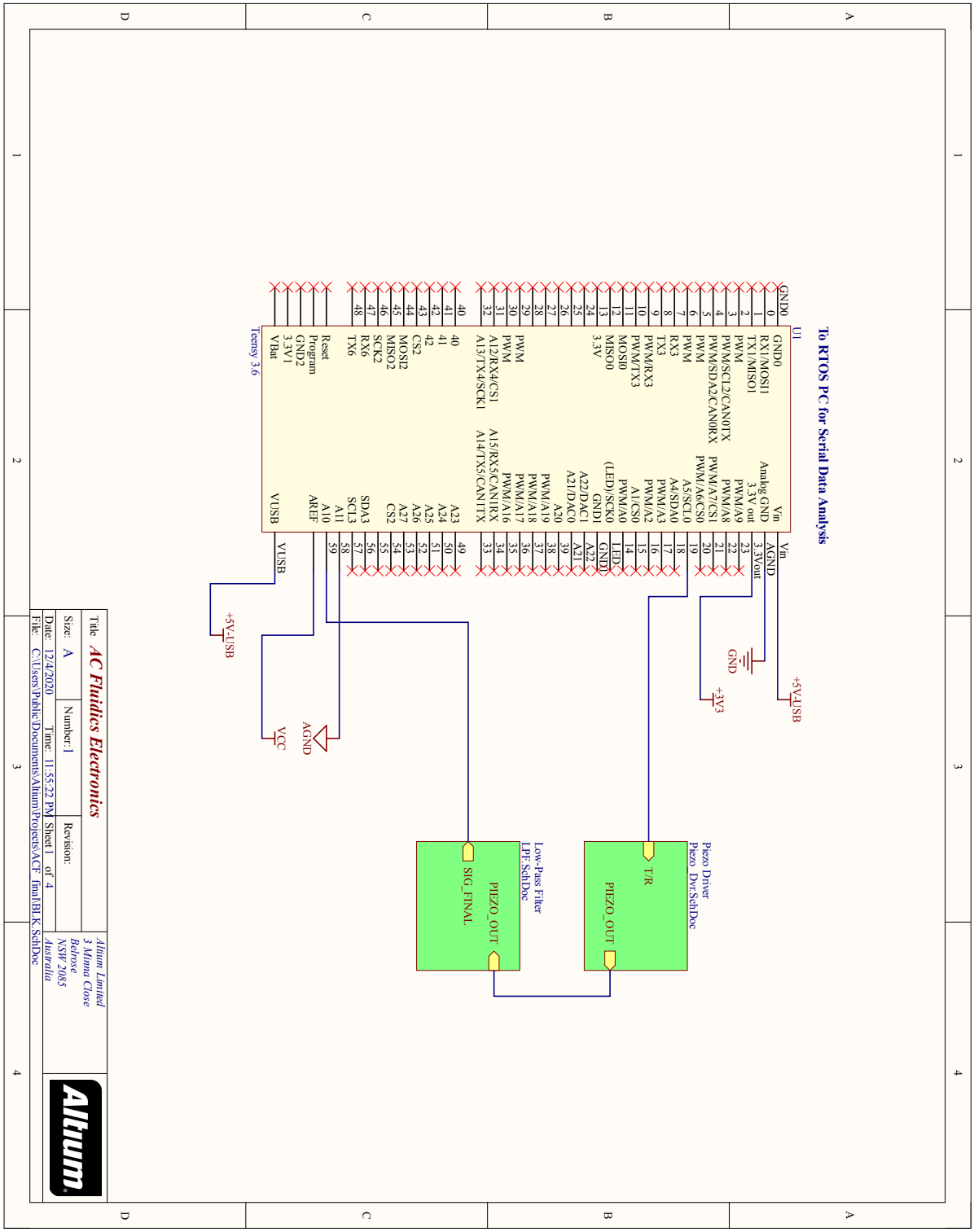

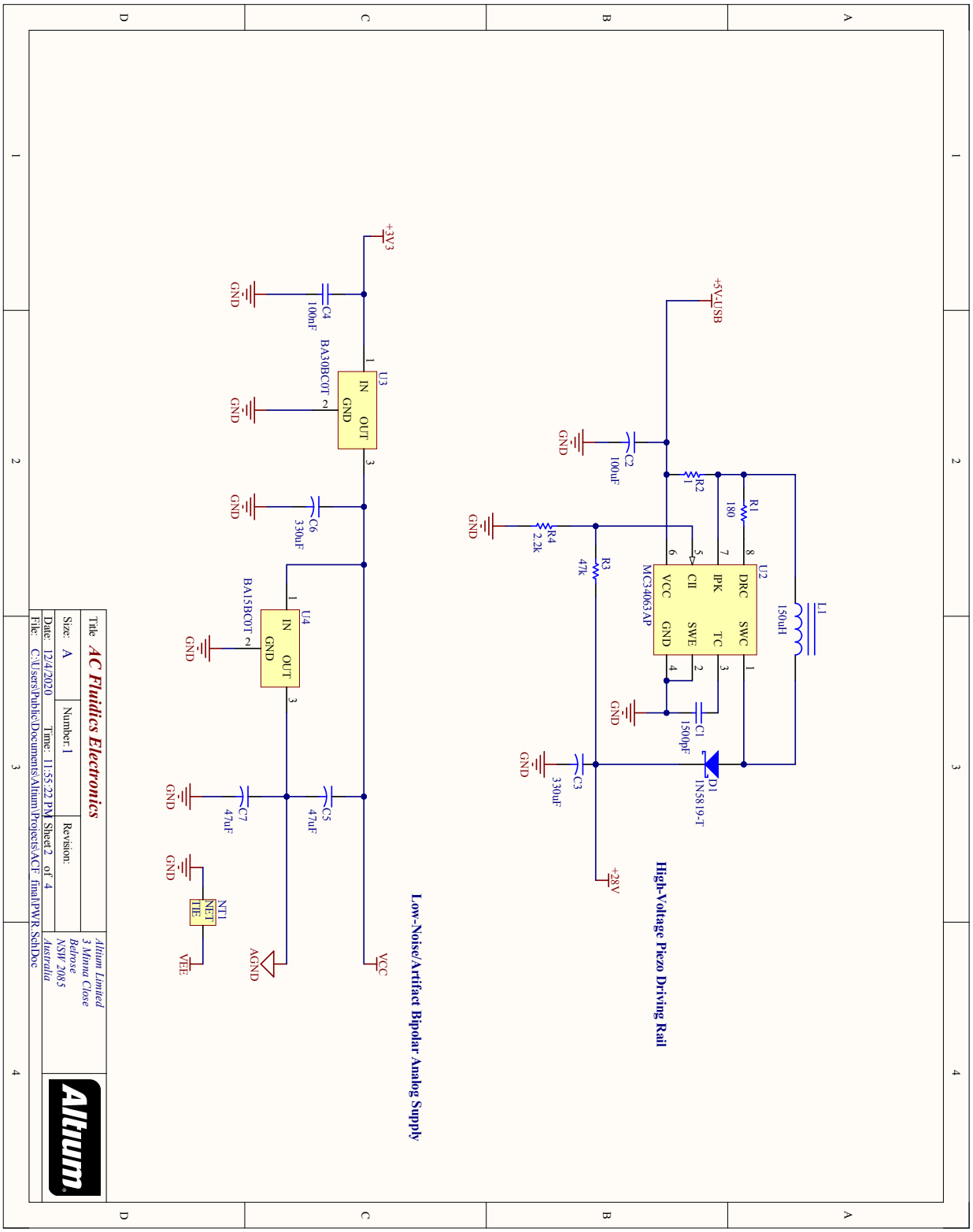
High-Voltage Piezo Driving Rail
Low-Noise/Artifact Bipolar Analog Supply
+5V-USB
L1
150uH
U2
MC34063AP
DRC
IPK
CII
VCC
SWC
TC
SWE
GND
R1
180
R2
1
R3
47k
R4
2.2k
C1
1500pF
C2
100uF
C3
330uF
D1
1N5819-T
+28V
+3V3
U3
BA30BC0T
U4
BA15BC0T
IN
OUT
C4
100nF
C5
47uF
C6
330uF
C7
47uF
NT1
NET TIE
VEE
VCC
AGND
Title
AC Fluidics Electronics
Size: A
Number 1
Revision:
Date: 12/4/2020
Time: 11:55:22 PM
Sheet 2 of 4
File: C:\Users\Public\Documents\Altium\Projects\ACF_final\PWR.SchDoc
Altium Limited
3 Minna Close
Belrose
NSW 2085
Australia

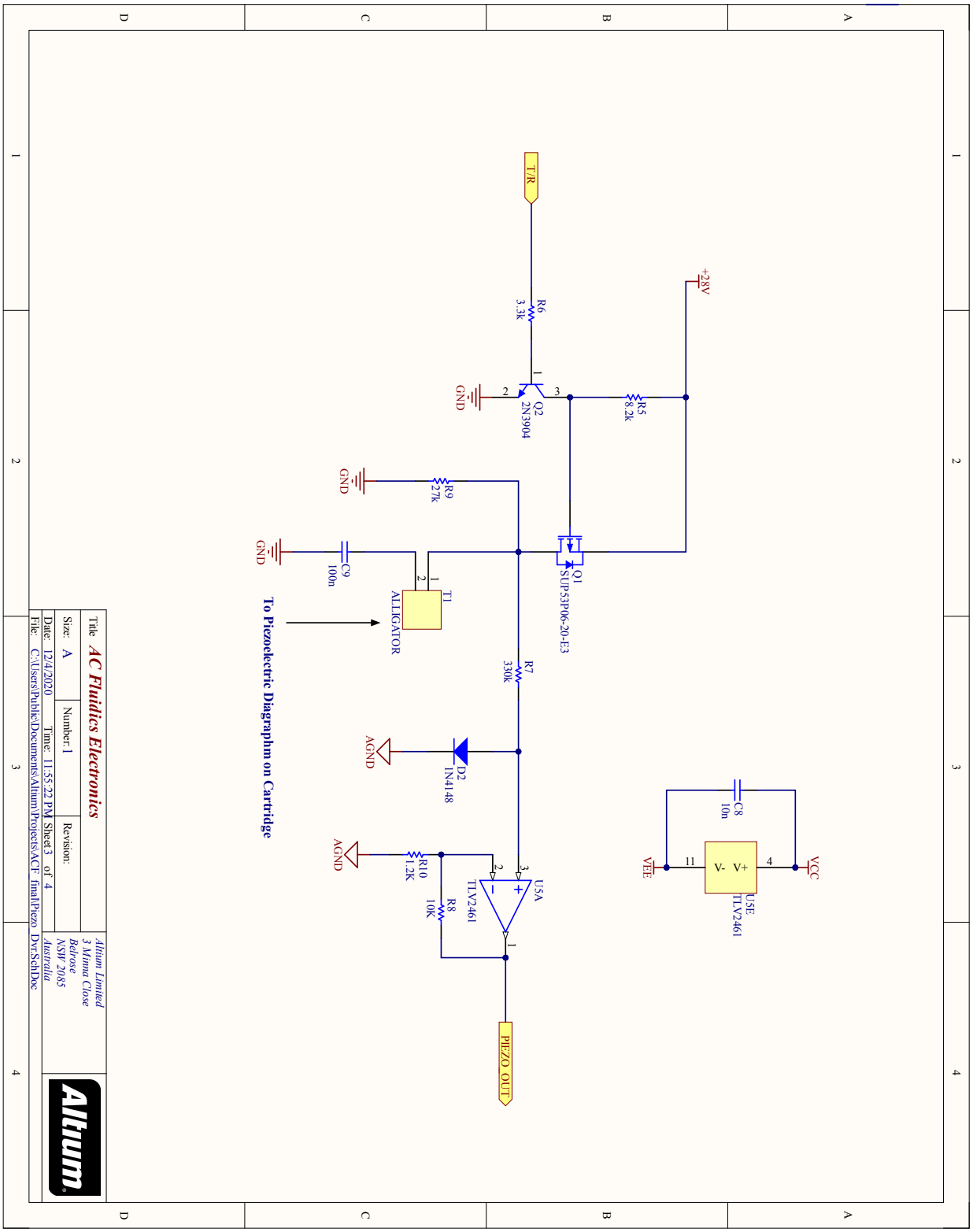
T/R
R6
3.3k
GND
Q2
2N3904
+28V
R5
8.2k
GND
R9
27k
GND
C9
100n
T1
ALLIGATOR
Q1
SUP53P06-20-E3
To Piezoelectric Diagraphim on Cartridge
R7
330k
AGND
D2
IN4148
AGND
R10
1.2K
R8
10K
U5A
TLV2461
PIEZO OUT
C8
10n
VEE
V-
V+
VCC
U5E
TLV2461
Title AC Fluidics Electronics
Size: A
Number 1
Revision:
Date: 12/4/2020
Time: 11:55:22 PM
Sheet 3 of 4
File: C:\Users\Public\Documents\Altium\Projects\ACF final\Piezo DrvSch.Doc
Altium Limited
3 Minna Close
Belrose
NSW 2085
Australia
Altium

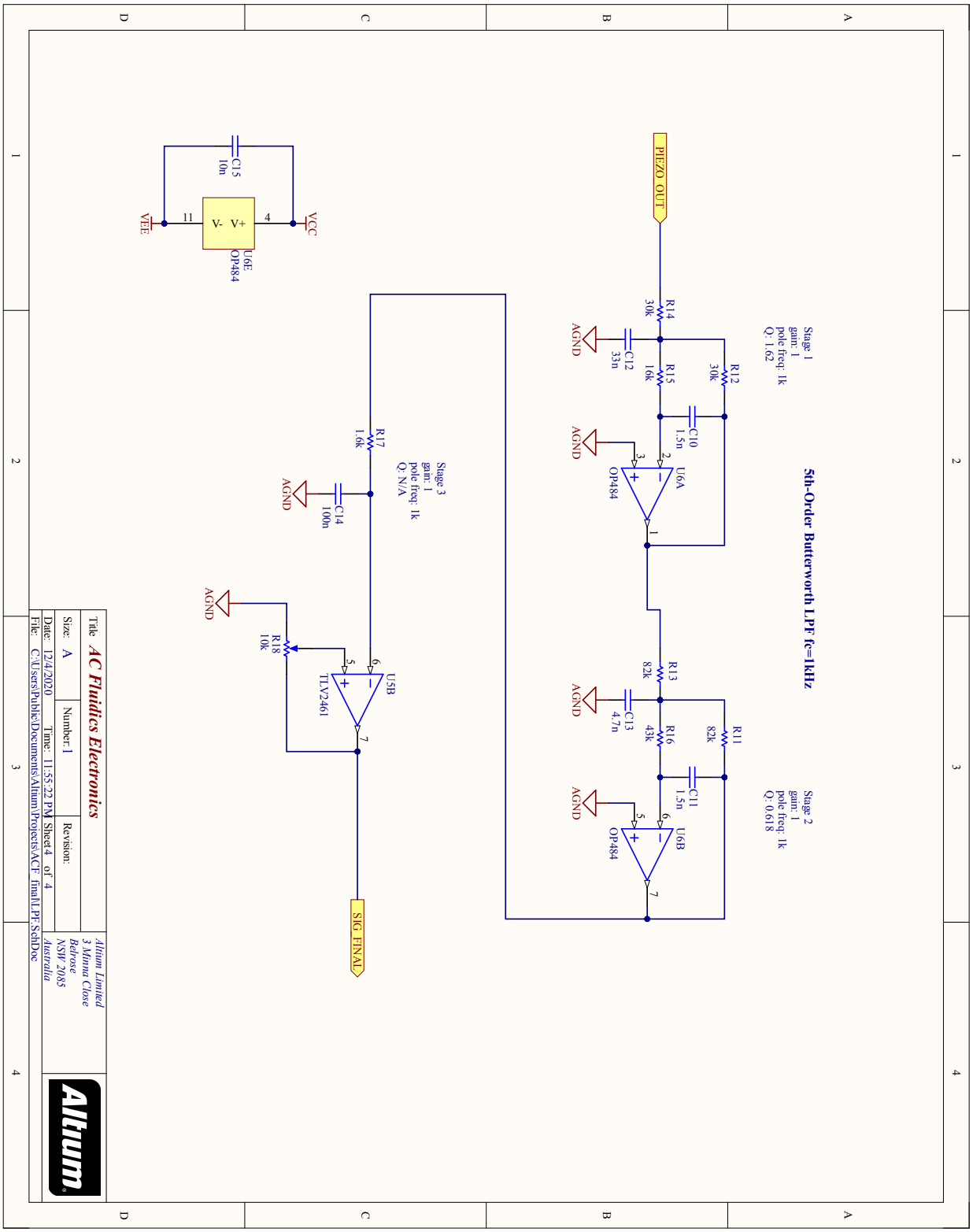
5th-Order Butterworth LPF fc=1kHz
Stage 1
gain: 1
pole freq: 1k
Q: 1.62
Stage 2
gain: 1
pole freq: 1k
Q: 0.618
Stage 3
gain: 1
pole freq: 1k
Q: N/A
PIEZO OUT
SIG_FINAL
AGND
VCC
VEE
R14 30k
R12 30k
R15 16k
C10 1.5n
C12 33n
U6A OP484
R13 82k
R11 82k
R16 43k
C11 1.5n
C13 4.7n
U6B OP484
R17 1.6k
C14 100n
R18 10k
U5B TLV2461
C15 10n
U6E OP484
Altium Limited
3 Minna Close
Belrose
NSW 2085
Australia
Title AC Fluidics Electronics
Size: A
Number 1
Revision:
Date: 12/4/2020
Time: 11:55:22 PM
Sheet 4 of 4
File: C:\Users\Public\Documents\Altium\Projects\ACF_final\LPF.SchDoc

Appendix C: Electrical Bill of Materials

Bill of Materials — **Colin Eckhoff** — **UW Bioengineering Fall 2020**

Line #	Designator	Qty	Value	Tolerance	Description	Category	Manufacturer	Manufacturer Part Nur	Vendor	Vendor Part #
1	C3, C6	2	300 uF	±20%	CAP ALUM 330UF 20% 63V RADIAL	Capacitor	Panasonic Electronic Components	ECA-1JHG331	Digikey	P5584-ND
2	L1	1	150 uH	±10%	FIXED IND 150UH 1A 340 MOHM TH	Inductor	Abracon LLC	AIAP-02-151K	Digikey	AIAP-02-151K-ND
3	U3	1	x	x	IC REG LINEAR 3V 1A TO220FP	Linear Regulator	Rohm Semiconductor	BA30BC0T	Digikey	BA30BC0T-ND
4	U4	1	x	x	IC REG LINEAR 1.5V 1A TO220FP	Linear Regulator	Rohm Semiconductor	BA15BC0T	Digikey	846-BA15BC0T-ND
5	Q1	1	x	x	MOSFET P-CH 60V 9.2A TO220AB	MOSFET	Vishay Siliconix	SUP53P06-20-E3	Digikey	SUP53P06-20-E3-ND
6	D1	1	x	x	DIODE SCHOTTKY 40V 1A DO41	Diode	Diodes Incorporated	1N5819-T	Digikey	1N5819DITR-ND
7	U1	1	x	x	TEENSY 3.6 W/ HDRS K66 EVAL BRD	MCU Eval Board	SparkFun Electronics	DEV-14058	Digikey	1568-1465-ND
8	U6	1	x	x	IC OPAMP GP 4 CIRCUIT 14DIP	Op Amp	Analog Devices Inc.	OP484FPZ	Digikey	OP484FPZ-ND
9	U5	1	x	x	IC OPAMP GP 2 CIRCUIT 8DIP	Op Amp	Texas Instruments	TLV2462IP	Digikey	296-1893-5-ND
10	U2	1	x	x	IC REG BUCK BST ADJ 1.5A 8DIP	DCDC Regulator	Texas Instruments	MC34063AP	Digikey	296-17766-5-ND

Appendix D: MCU Source Code

```
#include <IIRFilter.h>
#include <ADC.h>
#include "arduinoFFT.h"

#define TX 19

#define SAMPLES 512            // Must be a power of 2 for FFT
#define SAMPLING_FREQUENCY 20000 // Hz
#define REFRESH_RATE 10
#define AVG_EPOCHS 16
#define ZERO_PAD 4 // Multiplicative padding factor; must be power of 2
#define BOXCAR_ORDER 32
#define PRINT_RATE 2 // Divisive factor with refresh rate

ADC *adc = new ADC();

arduinoFFT fft = arduinoFFT();

unsigned long turn_count = 0;
unsigned int sampling_period_us;
unsigned int refresh_period_us;
unsigned long microseconds;
double vReal[SAMPLES * ZERO_PAD];
double vImag[SAMPLES * ZERO_PAD];
int acquisition_num = 1;

double waveform_0[SAMPLES];
double waveform_f1[SAMPLES];
double waveform_f2[SAMPLES / 2];
double waveform_f3[SAMPLES / 4];
double waveform_avg_input[AVG_EPOCHS][SAMPLES / 8];
double waveform_avg[SAMPLES / 8];

double freq[BOXCAR_ORDER];
int freq_num = 1;

const double B_lp[] =
{ 0.000499454078233100 , 0.00499454078233100, 0.0224754335204895,  0.0599344893879720  ,
0.104885356428951, 0.125862427714741, 0.104885356428951, 0.0599344893879720,  0.0224754335204895,
0.00499454078233100, 0.000499454078233100};
const double A_lp[] =
{1, -1.99240148160141, 3.01948286335539,  -2.81852242649452, 2.03872063706253,
-1.05454462109568, 0.414446268750400, -0.115718625236829,  0.0224985092722184,
-0.00266891235357610,  0.000148764452177762};
IIRFilter lp(B_lp, A_lp);

void setup() {
  Serial.begin(9600);
  analogReadRes(16);
  analogReadAveraging(8); // any higher than 8 messes with 50 us sampling period
  analogReference(EXTERNAL);
  pinMode(TX, OUTPUT);
  digitalWrite(TX, LOW);
  sampling_period_us = round(1000000 * (1.0 / SAMPLING_FREQUENCY));
  refresh_period_us = round(1000000 * (1.0 / REFRESH_RATE));
}
```

```
void loop() {
  long loopStart = micros();
  recordWaveform();
  downsample();
  average();
  differentiate();
  freq();
  plot('p'); // 't'-TD  'f'-FD  'p'-freq
  turn_count++;
  while (micros() - loopStart < refresh_period_us) {}
}

void recordWaveform() {
  digitalWrite(TX, HIGH);
  delay(5); // piezo charging up
  digitalWrite(TX, LOW);
  delay(4); // digital delay enough to prevent early signal chopping
  for (int i = 0; i < SAMPLES; i++) {
    microseconds = micros();
    waveform_0[i] = adc->analogReadDifferential(A10, A11);
    while (micros() < (microseconds + sampling_period_us)) {}
  }
}

void downsample() {
  for (int i = 0; i < SAMPLES; i++) {
    waveform_f1[i] = lp.filter(waveform_0[i]);
  }
  for (int i = 0; i < SAMPLES / 2; i++) {
    waveform_f2[i] = lp.filter(waveform_f1[i * 2]);
  }
  for (int i = 0; i < SAMPLES / 4; i++) {
    waveform_f3[i] = lp.filter(waveform_f2[i * 2]);
  }
  for (int i = 0; i < SAMPLES / 8; i++) {
    waveform_avg_input[acquisition_num - 1][i] = waveform_f3[i * 2];
  }
  acquisition_num++;
  if (acquisition_num > AVG_EPOCHS) {
    acquisition_num = 1;
  }
}

void average() {
  for (int i = 0; i < SAMPLES / 8; i++) {
    waveform_avg[i] = 0;
    for (int j = 0; j < AVG_EPOCHS; j++) {
      waveform_avg[i] += waveform_avg_input[j][i];
    }
    waveform_avg[i] /= AVG_EPOCHS;
  }
}

void differentiate() {
  for (int i = 0; i < SAMPLES / 8 - 5; i++) {
    waveform_avg[i] = (3 * waveform_avg[i] / -16) + (31 * waveform_avg[i + 1] / 32) + (31 *
waveform_avg[i + 3] / -32) + (3 * waveform_avg[i + 4] / 16);
  }
  for (int i = SAMPLES / 8 - 5; i < SAMPLES / 8; i++) {
```

```
    waveform_avg[i] = waveform_avg[i - 1];
  }
}

void freq() {
  double mean = 0;
  for (int i = 0; i < SAMPLES / 8; i++) {
    vReal[i] = waveform_avg[i];
    vImag[i] = 0;
    mean += vReal[i];
  }
  for (int i = SAMPLES / 8; i < SAMPLES / 8  * ZERO_PAD; i++) { // zero padding
    vReal[i] = 0;
    vImag[i] = 0;
  }
  fft.Windowing(vReal, SAMPLES / 8, FFT_WIN_TYP_HANN, FFT_FORWARD);
  fft.Compute(vReal, vImag, SAMPLES / 8 * ZERO_PAD, FFT_FORWARD);
  fft.ComplexToMagnitude(vReal, vImag, SAMPLES / 8 * ZERO_PAD);
  freq[freq_num - 1] = fft.MajorPeak(vReal, SAMPLES / 8 * ZERO_PAD, SAMPLING_FREQUENCY / 8);
  freq_num++;
  if (freq_num > BOXCAR_ORDER) {
    freq_num = 1;
  }
}

void plot(char arg) {
  switch (arg) {
    case 'f':
      for (int i = 0; i < (SAMPLES * ZERO_PAD / 8); i++) {
        Serial.println(vReal[i], 1);
      }
      break;
    case 't':
      for (int i = 0; i < SAMPLES / 1; i++) {
        Serial.println(waveform_f1[i]);
      }
      break;
    case 'p':
      double freq_value = 0;
      for (int i = 0; i < BOXCAR_ORDER; i++) {
        freq_value += freq[i];
      }
      freq_value /= BOXCAR_ORDER;
      if (turn_count % PRINT_RATE == 0) {
        Serial.println(freq_value);
      }
      break;
  }
}
```

References

1) *Injuries and Violence: the Facts 2014*. Department for the Management of Noncommunicable Diseases, Disability, Violence and Injury Prevention, World Health Organization, 2014.
2) S. Mondello, A. Cantrell, D. Italiano, V. Fodale, P. Mondello, and D. Ang, "Complications of Trauma Patients Admitted to the ICU in Level I Academic Trauma Centers in the United States," Biomed Res Int, vol. 2014, 2014, doi: 10.1155/2014/473419.
3) P. Rhee *et al*., "Increasing trauma deaths in the United States," *Ann. Surg*., vol. 260, no. 1, pp. 13–21, Jul. 2014, doi: 10.1097/SLA.0000000000000600.
4) R. Lozano et al., "Global and regional mortality from 235 causes of death for 20 age groups in 1990 and 2010: a systematic analysis for the Global Burden of Disease Study 2010," Lancet, vol. 380, no. 9859, pp. 2095–2128, Dec. 2012, doi: 10.1016/S0140-6736(12)61728-0.
5) B. T. Oyeniyi, E. E. Fox, M. Scerbo, J. S. Tomasek, C. E. Wade, and J. B. Holcomb, "Trends in 1029 Trauma Deaths at a Level 1 Trauma Center," *Injury*, vol. 48, no. 1, pp. 5–12, Jan. 2017, doi: 10.1016/j.injury.2016.10.037.
6) "WISQARS (Web-based Injury Statistics Query and Reporting System)|Injury Center|CDC," Jul. 01, 2020. https://www.cdc.gov/injury/wisqars/index.html (accessed Jul. 21, 2020).
7) Committee on Military Trauma Care's Learning Health System and Its Translation to the Civilian Sector, Board on Health Sciences Policy, Board on the Health of Select Populations, Health and Medicine Division, and National Academies of Sciences, Engineering, and Medicine, *A National Trauma Care System: Integrating Military and Civilian Trauma Systems to Achieve Zero Preventable Deaths After Injury*. Washington (DC): National Academies Press (US), 2016.
8) D. S. Kauvar, R. Lefering, and C. E. Wade, "Impact of hemorrhage on trauma outcome: an overview of epidemiology, clinical presentations, and therapeutic considerations," *J Trauma*, vol. 60, no. 6 Suppl, pp. S3-11, Jun. 2006, doi: 10.1097/01.ta.0000199961.02677.19.
9) P. C. Spinella, "Zero preventable deaths after traumatic injury: An achievable goal," *J Trauma Acute Care Surg*, vol. 82, no. 6S Suppl 1, pp. S2–S8, 2017, doi: 10.1097/TA.0000000000001425.
10) M. Giannoudi and P. Harwood, "Damage control resuscitation: lessons learned," *Eur J Trauma Emerg Surg*, vol. 42, pp. 273–282, 2016, doi: 10.1007/s00068-015-0628-3.
11) C. G. Ball, "Damage control resuscitation: history, theory and technique," *Can J Surg*, vol. 57, no. 1, pp. 55–60, Feb. 2014, doi: 10.1503/cjs.020312.
12) A. Ja et al., "Operative management and outcomes in 103 AAST-OIS grades IV and V complex hepatic injuries: trauma surgeons still need to operate, but angioembolization helps," The Journal of trauma, Apr. 2003. https://pubmed.ncbi.nlm.nih.gov/12707525/ (accessed Dec. 01, 2020).
13) N. Curry and P. W. Davis, "What's new in resuscitation strategies for the patient with multiple trauma?," *Injury*, vol. 43, no. 7, pp. 1021–1028, Jul. 2012, doi: 10.1016/j.injury.2012.03.014.
14) J. Mikhail, "The trauma triad of death: hypothermia, acidosis, and coagulopathy," *AACN Clin Issues*, vol. 10, no. 1, pp. 85–94, Feb. 1999.

15) M. González Balverde, E. J. Ramírez Lizardo, E. G. Cardona Muñoz, S. E. Totsuka Sutto, and L. García Benavides, "Prognostic value of the lethal triad among patients with multiple trauma," *Revista médica de Chile*, vol. 141, no. 11, pp. 1420–1426, Nov. 2013, doi: 10.4067/S0034-98872013001100008.
16) B. Mitra, F. Tullio, P. A. Cameron, and M. Fitzgerald, "Trauma patients with the 'triad of death,'" *Emerg Med J*, vol. 29, no. 8, pp. 622–625, Aug. 2012, doi: 10.1136/emj.2011.113167.
17) N. Credland, "Managing the trauma patient presenting with the lethal triad," International Journal of Orthopaedic and Trauma Nursing, vol. 20, pp. 45–53, Feb. 2016, doi: 10.1016/j.ijotn.2015.09.003.
18) J. S. Hagemo, "Prehospital detection of traumatic coagulopathy," *Transfusion*, vol. 53 Suppl 1, pp. 48S-51S, Jan. 2013, doi: 10.1111/trf.12035.
19) J. B. Holcomb *et al*., "Admission rapid thrombelastography can replace conventional coagulation tests in the emergency department: experience with 1974 consecutive trauma patients," *Ann. Surg*., vol. 256, no. 3, pp. 476–486, Sep. 2012, doi: 10.1097/SLA.0b013e3182658180.
20) M. E. Shaydakov, D. F. Sigmon, and J. Blebea, "Thromboelastography (TEG)," in *StatPearls*, Treasure Island (FL): StatPearls Publishing, 2020.
21) S. Palta, R. Saroa, and A. Palta, "Overview of the coagulation system," Indian Journal of Anaesthesia, vol. 58, no. 5, p. 515, Oct. 2014, doi: 10.4103/0019-5049.144643.
22) P. C. Spinella and A. P. Cap, "Prehospital hemostatic resuscitation to achieve zero preventable deaths after traumatic injury," *Curr. Opin. Hematol*., vol. 24, no. 6, pp. 529–535, Nov. 2017, doi: 10.1097/MOH.0000000000000386.
23) G. Hochleitner, K. Sutor, C. Levett, H. Leyser, C. J. Schlimp, and C. Solomon, "Revisiting Hartert's 1962 Calculation of the Physical Constants of Thrombelastography," Clin Appl Thromb Hemost, vol. 23, no. 3, pp. 201–210, Apr. 2017, doi: 10.1177/1076029615606531.
24) G. W. Blair and R. H. Matchett, "The kinetics of the polymerization of fibrin in some normal and pathological bloods as studied with the thrombelastograph," Biorheology, vol. 7, no. 3, pp. 171–176, Jan. 1971, doi: 10.3233/bir-1971-7302.
25) E. Mfoumou, J. Tripette, M. Blostein, and G. Cloutier, "Time-dependent hardening of blood clots quantitatively measured in vivo with shear-wave ultrasound imaging in a rabbit model of venous thrombosis," Thromb Res, vol. 133, no. 2, pp. 265–271, Feb. 2014, doi: 10.1016/j.thromres.2013.11.001.
26) R. Jain, R. B. Darling, and B. Lutz, "Frequency characterization of flow magnitude and phase in resonant microfluidic circuits," Analytical Methods, vol. 9, no. 37, pp. 5425–5432, 2017.
27) R. Jain, "Smartphones for control and detection of rapid diagnostic tests," Thesis, 2018.
28) T. B. Greenslade, "The Hydraulic Analogy for Electric Current," The Physics Teacher, vol. 41, no. 8, pp. 464–466, Oct. 2003, doi: 10.1119/1.1625205.
29) C. Morris and F. Forster, "The correct treatment of harmonic pressure-flow behavior in microchannels," Jan. 2000.
30) M. R. Begley, M. Utz, D. C. Leslie, H. Haj-Hariri, J. Landers, and H. Bart-Smith, "Periodic response of fluidic networks with passive deformable features," Appl. Phys. Lett., vol. 95, no. 20, p. 203501, Nov. 2009.

31) J. P. Landers, Handbook of Capillary and Microchip Electrophoresis and Associated Microtechniques. CRC Press, 2007.
32) A. E. X. Brown, R. I. Litvinov, D. E. Discher, P. K. Purohit, and J. W. Weisel, "Multiscale Mechanics of Fibrin Polymer: Gel Stretching with Protein Unfolding and Loss of Water," Science, vol. 325, no. 5941, pp. 741–744, Aug. 2009, doi: 10.1126/science.1172484.
33) G. Wu, C. R. Krebs, F. C. Lin, A. S. Wolberg, and A. L. Oldenburg, "High sensitivity micro-elastometry: applications in blood coagulopathy.," Ann Biomed Eng, vol. 41, no. 10, pp. 2120–2129, Oct. 2013, doi: 10.1007/s10439-013-0817-3.
34) "A New Contender in the Digital Differentiator Race - Rick Lyons." https://www.dsprelated.com/showarticle/814.php (accessed Dec. 04, 2020).
35) E. Jacobsen and P. Kootsookos, "Fast, Accurate Frequency Estimators [DSP Tips Tricks]," IEEE Signal Processing Magazine, vol. 24, no. 3, pp. 123–125, May 2007, doi: 10.1109/MSP.2007.361611.
36) K. M. Weigandt et al., "Fibrin Clot Structure and Mechanics Associated with Specific Oxidation of Methionine Residues in Fibrinogen," Biophys J, vol. 103, no. 11, pp. 2399–2407, Dec. 2012, doi: 10.1016/j.bpj.2012.10.036.
37) O. H. Larsen, C. Fenger-Eriksen, K. Christiansen, J. Ingerslev, and B. Sørensen, "Diagnostic Performance and Therapeutic Consequence of Thromboelastometry Activated by Kaolin versus a Panel of Specific Reagents," Anesthesiology, vol. 115, no. 2, pp. 294–302, Aug. 2011, doi: 10.1097/ALN.0b013e318220755c.
38) H. Schöchl et al., "FIBTEM provides early prediction of massive transfusion in trauma," Crit Care, vol. 15, no. 6, p. R265, 2011, doi: 10.1186/cc10539.
39) C. Solomon, H. Schöchl, M. Ranucci, U. Schött, and C. J. Schlimp, "Comparison of fibrin-based clot elasticity parameters measured by free oscillation rheometry (ReoRox®) versus thromboelastometry (ROTEM®)," Scand J Clin Lab Invest, vol. 75, no. 3, pp. 239–246, May 2015, doi: 10.3109/00365513.2014.993698.
40) W. R. Burghardt, T. K. Goldstick, J. Leneschmidt, and K. Kempka, "Nonlinear viscoelasticity and the thrombelastograph: 1. Studies on bovine plasma clots," Biorheology, vol. 32, no. 6, pp. 621–630, Dec. 1995, doi: 10.1016/0006-355X(95)00041-7.
41) D. Tabriz, B. Swilley, and B. Toskich, "Thromboelastography: useful and underutilized," Journal of Vascular and Interventional Radiology, vol. 27, no. 3, pp. S228–S229, Mar. 2016, doi: 10.1016/j.jvir.2015.12.586.